AIRWAY MECHANICS
AND
PULMONARY FUNCTION TESTS

A thesis presented in partial fulfilment of the requirements for the degree of
Doctor of Philosophy in
Physics

at Massey University
Palmerston North
New Zealand

Ulrich Holzhäuser
1999

ABSTRACT

Methods of engineering mechanics were applied to further the theoretical understanding of the elastic deformation of some specific components of the tracheobronchial tree when subject to a transmural pressure difference.

The contribution of the epithelial basement membrane to airway collapse was analysed. The well-known approach based on the physics of a shell was extended to investigate the influence of a non-homogeneous stiffness of the basement membrane on airway collapse. Results were obtained for the fundamental "two-lobe" collapse. These indicate that the critical pressure at which collapse starts depends on the location of the region of maximal stiffness.

A method was presented for analysing asymmetric stress-strain behaviour when the Young modulus of a material is different in compression than in tension. Results indicated that, if the basement membrane were stiffer in compression than in tension, the resulting collapsed structure would be slightly stiffer than in the case of no stiffness difference and thus the airway would be less narrowed and less compliant.

The deformation of the trachea was analysed by using the same theory as used in the study of the folding of the epithelial membrane. Computations were made to investigate (i) a semi-circular "base-shape" as well as more complex, non-circular shapes, (ii) the effect of shortening of the posterior membrane, (iii) localised weakening of the cartilage ring. Good agreement between model predictions and published MRI microscopy data from rabbit tracheas was obtained.

The concepts of fluid mechanics in elastic tubes were used to analyse the effects of airway remodelling on forced expiratory airflow and resistance to airflow. The tracheobronchial tree was modeled as a system of branching, elastic tubes. Flow behaviour through that system of tubes was analysed which allowed the simulation of pulmonary function tests, in particular forced expiration and response to a muscle agonist. Effects of thickening of the airway wall components (adventita, smooth muscle and the submucosa) on exiratory flow and airways resistance, were investigated. Results showed that thickening of the smooth muscle had the strongest effect on expiratory airflow and airway resistance, followed by thickening of the submucosal area. Model results were within a physiologically feasible range.

ACKNOWLEDGEMENTS

The following people have helped me during the course of this work. It is a pleasure to thank them.

Assoc. Prof. Rod K. Lambert, my first supervisor, for his constant support, enthusiasm, expertise and patience during our discussions.

Dr. Craig Eccles, my second supervisor for his assistance with software-related problems.

Dr. Rodger Pack, from Massey University's Institute of Food, Nutrition and Human Health, my third supervisor, for reading the draft of my thesis and his useful advice.

Assoc. Prof. Bob O'Driscoll for his assistance with computer equipment-related problems.

Barbara Moore from University of British Columbia Pulmonary Research Laboratory, Vancouver, Canada for letting me use some of her data.

The Palmerston North Medical Research Foundation for their research grant.

All members of the Institute of Fundamental Sciences for maintaining a pleasant working environment.

Last but not least my parents, who always supported me, although they hated the idea of me going to New Zealand to pursue PhD studies.

TABLE OF CONTENTS

PART II:

Forced expiratory flow in the presence of muscle tone................ 64

List of Figures

PART I:

PART II:

List of symbols

PART I:

F : force
T : tensile force/unit axial length
S : shear force/unit axial length
M : bending moment/unit axial length
P : pressure
κ : curvature
ν : Poisson ratio
E : Young modulus
t : thickness
D : flexural rigidity
s : arc length
R : tube radius
$f(s)$: function indicating dimensionless variation of stiffness distribution
α : stiffness coefficient
θ : angle that tube wall makes with reference direction
P^* : normalised pressure
P^*_{cr} : normalised critical pressure
P^*_c : normalised wall-touching pressure
λ : normalised arc length
n : number of folds
x,y : coordinates of tube wall
A_0 : initial cross-sectional area
A : cross-sectional area
ε : strain
σ : stress
η : ratio between Young moduli
I_A : second moment of area

$\beta(\eta)$: function describing change of flexural rigidity of a composite area

CF : cost function

L_{max} : length at which maximal isometric force was generated

L : posterior membrane length (trachea)

w : width of cartilage ring

a,b : ellipse half radii of cartilage ring

c_s : stretch coefficient

h : arc height

r : radius (intercartilaginous membrane deformations)

PART II:

Raw : airway resistance

FEV_1 : forced expiratory volume in one second

TLC : total lung capacity

VC : vital capacity

RV : residual volume

FRC : functional residual volume

p : pressure

ρ : density

μ : viscosity

z : generation number

U : local average flow speed

$\dot{V}$: volume flow

A : cross-sectional area

f : dissipative pressure loss/unit length

c : wave speed

Re : Reynolds number

L : length of airway

α : specific airway compliance

V : volume

P_o^* : outer adventital perimeter

P^*_{mo} : outer perimeter of airway smooth muscle

P_{bm} : perimeter of basement membrane

D^*_{bm} : maximal diameter of basement membrane

D^*_{e} : maximal diameter external to smooth muscle

D^*_{o} : maximal outer diameter

WA_o : outer (adventital) wall area

WA_{sm} : smooth muscle wall area

WA_i : wall area internal to smooth muscle (sub mucosa)

T_N : normalised tension

σ : stress

G : parenchymal shear modulus

PMS : percentage smooth muscle shortening

α, β : coefficients for PMS function

dose : (hypothetical) agonist causing smooth muscle shortening

INTRODUCTION

This brief general introduction is to set the scene for the whole thesis. More detailed introductory material will be presented in the introductions to each of part I and part II.

Airway diseases are among the world's most prevalent diseases [77]. The predominant forms of airway diseases are asthma and disorders such as emphysema, peripheral airways disease and chronic bronchitis which are summarised as chronic obstructive pulmonary disease (COPD) [2]. Current (June 1999) statistics show that in New Zealand, for example 15.5 % of adults suffer from asthma, and the rate among 14 years old is as high as 30% [3]. Worldwide, asthma affects up to 10% of the populations in most developed countries. COPD ranks as the fifth highest cause for death COPD for New Zealand men (1996) [4], it is the sixth cause of death in the world [77]. It affects 4-6% of people more than 45 years of age [77]. These diseases constitute a major financial burden to society, with both direct and indirect costs. The treatment of both diseases requires an understanding of the relationships between the structural changes which occur in disease and the consequences on the functionality of the lung.

The major difference between COPD and asthma is a reversibility of airways obstruction in asthma that can be achieved by the administration of bronchodilating agents. COPD is characterised as a long-term disease whereas asthma must be reversible to establish a diagnosis [2]. The cause for both diseases is lung inflammation induced by various initiating factors, most likely environmental allergens, occupational sensitising agents, viral respiratory infections in asthma and cigarette smoking in COPD [77].

Pathological changes in COPD are found in the central as well as in the small airways and in the lung parenchyma [77]. Macroscopically, these changes lead to thicker airway walls and thus to airway obstruction. The situation with asthma is less clear. Currently available knowledge regarding the interrelationship between inflammation and airway function is based on acute inflammatory events, such as airway smooth muscle contraction and (sub)mucosal swelling to name only two factors which might occur in asthma [77].

The clinical syndrome in asthmatics is characterised by an increased responsiveness of the tracheobronchial tree to a variety of stimuli resulting in excessive airway narrowing [77]. Airway narrowing in COPD is caused by changes in the different constituents of the airway wall [77]. The ultimate manifestation of both conditions is airway obstruction and reduced airflow. Even though in the past there have been many studies aimed at increased understanding of the physiology of the lung and how structural changes such as airway remodelling affect the functionality of the lung, the present understanding is far from being complete. An understanding of how the observed changes in airway morphology in pathological situations affect its functionality requires the understanding of the mechanics of the lung, especially its central component, the tracheobronchial tree.

The concepts employed in this thesis to analyse the mechanics of the lung and its functional impairment in disease are based on engineering mechanics. The lung is essentially a mechanical system that can be described as a bellows which is inflated and deflated as air is pumped in and out [28]. Airway narrowing as a response to non-specific stimuli has the mechanical effect of increasing the resistance to flow of the tracheobronchial tree thus increasing the work of breathing for the sufferer. Hence to understand the effects of airway narrowing it is important to understand how changes in airway geometry and mechanics affect flow through the airways.

The approach used is to model the tracheobronchial tree as a system of branching elastic tubes which serve the purpose of conducting air from the trachea to the alveolar ducts or vice versa. Crucial for this approach is a thorough knowledge of the tube law of all airways, that is the change of cross-sectional area as a function of the pressure difference across the tube wall. This necessarily involves knowledge of the elastic properties of the biological tissues that make up the airway walls.

The knowledge of the tube law or the compliance of an elastic tube is also crucial when one wants to analyse flow behaviour through that tube [91]. By applying the concepts of flow in collapsible tubes to the tracheobronchial tree one is, in principle, able to predict expiratory airflow of the lungs and resistance to flow through the tracheobronchial tree. Of considerable interest is the understanding of forced expiratory flow and how structural changes affect forced expiratory flow since the most commonly applied pulmonary function tests for assessing the functionality of the lungs are based on forced expiration. This thesis is concerned with advancing our knowledge of the mechanics underlying these phenomena and our ability to interpret experimental data through the use of appropriate models.

The thesis is subdivided into two parts. Part One is concerned with the theoretical analysis of the mechanics of some specific, individual components of the bronchial tree, that is the bronchioles at the periphery of the tracheobronchial tree and the trachea, the most centrally located airway. In particular, chapter two is concerned with the mechanics of the bronchial basement membrane and its contribution to the mechanical phenomenon of airway collapse. A published theory will first be reviewed and subsequently extended to study effects of a non-homogenous stiffness on airway collapse. In chapter three a theoretical analysis of tracheal mechanics is presented. It includes an analysis of the deformation of the cartilage "horseshoe" with the posterior membrane joining the tips of the horseshoe. The analysis was extended to study a non-homogeneous stiffness of the cartilage ring and to include effects of stretching of the posterior membrane. Additionally, it includes an analysis aimed at investigating the effect of the highly elastic connective tissue between two adjacent horseshoes on the deformation of the horseshoes.

Part Two is concerned with the simulation of airflow and pulmonary function tests based on the geometry and compliance of the components of the tracheobronchial tree. Two well-established models, the computational model to simulate forced expiratory flow and the computational model designed to study airway wall remodelling and how it affects airway resistance are reviewed. The objective of Part II is to merge both models to provide more realistic insights into the interrelationship between forced expiratory flow, airway resistance, smooth muscle tone and airway wall remodelling. The new model is used to study effects of airway wall thickening on forced expiratory airflow and airway resistance during breathing.

PART I:

A theoretical analysis of the mechanics of individual components of the tracheobronchial tree

1. Introduction and literature review

A detailed understanding of area-pressure relationships of all airways in the human lung is crucial to an understanding of airflow in the lung. The factors which determine the area-pressure relationship of an airway are (i) the composition of the airway wall, or more specifically the individual elastic properties of each layer of the airway wall, and (ii) the surroundings in which the individual airway is embedded. When moving along the pathway of the bronchial tree one can see that the composition as well as the surrounding changes. One distinctive indicator for example is the presence and shape of cartilage. The cartilages of the trachea and the main stem bronchi are horseshoe-shaped, whereas in the smaller airways, deeper in the lung, the cartilages are less complete and consist of irregular plates. Following the pathway more distally, the cartilages become progressively smaller until in bronchi slightly under 1 mm in diameter they surround only the origins of the bronchioles arising from them. Furthermore, intrathoracic airways are embedded in lung parenchyma which consists mostly of alveolar walls and septa and provides an elastic medium in which the airways are embedded. A detailed discussion of the pulmonary anatomy is beyond the scope of this thesis. Comprehensive reviews of the morphology of the human lung can be found in an abundance of literature as for example in [15, 97, 103].

Structural changes of the airways as well as changes in the surroundings play an important role in the behaviour of an airway when subject to a pressure difference across its wall. Consequently, within the last forty years a considerable number of experimental studies on various parts of the airways under various conditions have been conducted. One of the earliest studies was conducted by Martin and Proctor [64]. They conducted pressure-volume studies on dog trachea and bronchi and concluded that the elastic retractive forces of the lungs and chest become extremely important in holding the bronchi open. Later Olson et al. worked with isolated cat trachea to learn how muscle constriction increases the ability of tracheae to withstand compressive narrowing. [79]. About this time Hyatt and Flath conducted pressure - diameter studies on dog bronchi with and without the influence of the surrounding parenchyma [34]. They concluded that observations made on excised bronchial segments can be taken as fairly representative of the behaviour of the bronchial tree when surrounded by lung parenchyma. In the seventies, Jones et al. predicted the maximal expiratory flow rates from area-transmural pressure curves of compressed airway [44]. They measured a series of area-pressure curves of trachea and main stem bronchi of dog lungs. In a subsequent paper they studied the effect of pharmacologically altered airway mechanics on maximal expiratory flow and presented further area-pressure curves of dog tracheae [45]. Mortola and Sant'Ambrogio studied the mechanics of the trachea in various species determining the pressure-volume relationships [75]. They concluded that the motion of the posterior membrane wall contributes most to the tracheal volume changes. *In vivo* pressure-volume measurements on canine trachea were made by Winter et al and Winter [110, 111]. They pointed out that their specific compliance values were notably less than the values reported for excised trachea. The effect of weakening the cartilaginous structure on pressure-volume curves was investigated by Moreno et al. using rabbit tracheae [74]. They concluded that airway cartilage softening increases the compliance of the trachea. Moreno et al also conducted *in vivo* measurements on human tracheae [72]. Lambert et al. obtained area-pressure relationships for rabbit tracheae by using nuclear magnetic resonance imaging techniques [57]. They showed that tracheal posterior membrane invaginated asymmetrically into the lumen area, thus the muscle appeared to favour one side of the cartilage ring system more than the other. Thus, there appears to be a considerable amount of experimental data available but little of it has been related to the structure and the mechanical properties of the tissues that make up the airways.

One of the few attempts to provide a theoretical base was published by Begis et al and consisted of a finite element analysis of tracheal collapse with which they were, with some success, able to compute parts of the transmural pressure area curve of a human trachea [8]. Later, Lambert analysed the role of bronchial basement membrane as a potential contributor to airway stiffness [53] and applied his model to the collapse of an airway undergoing bronchoconstriction [56]. The analysis was based on a homogeneous isotropic shell of uniform thickness. This model was also used as a starting point to investigate effects of surface tension and intraluminal fluid on the mechanics of small airways [32]. In this thesis Lambert's model will be applied and extended in order to investigate the possibility of a non-uniform stiffness of the basement membrane. Finally, by using the same elastica theory as used in Lambert's model a comprehensive theoretical analysis of tracheal collapse will be presented.

2. The contribution of bronchial basement epithelium membrane to airway collapse

2.1 Introduction

In non-cartilaginous airways the parenchyma and the outer wall of the smooth muscle both contribute to the stiffness of the airway. The contribution of the inner layer of the airway wall, the epithelial basement membrane has only recently been recognized as a potential contributor to the stiffness of the airway [53].

When the airway smooth muscle contracts and the diameter of the bronchus is reduced, the membrane develops folds to accommodate the reduction in diameter. The external pressure on the membrane is the pressure in the highly deformable region of the bronchial wall between the muscle and the membrane and the internal pressure on the membrane is the pressure in the bronchial lumen (both pressures are referenced to pleural pressure). The membrane which is probably composed mostly of collagen IV [100], can then be mechanically treated as a thin-walled elastic tube that is collapsing under the influence of a pressure difference across its wall. A micrograph of a partially collapsed airway is shown in Fig. 2.1.

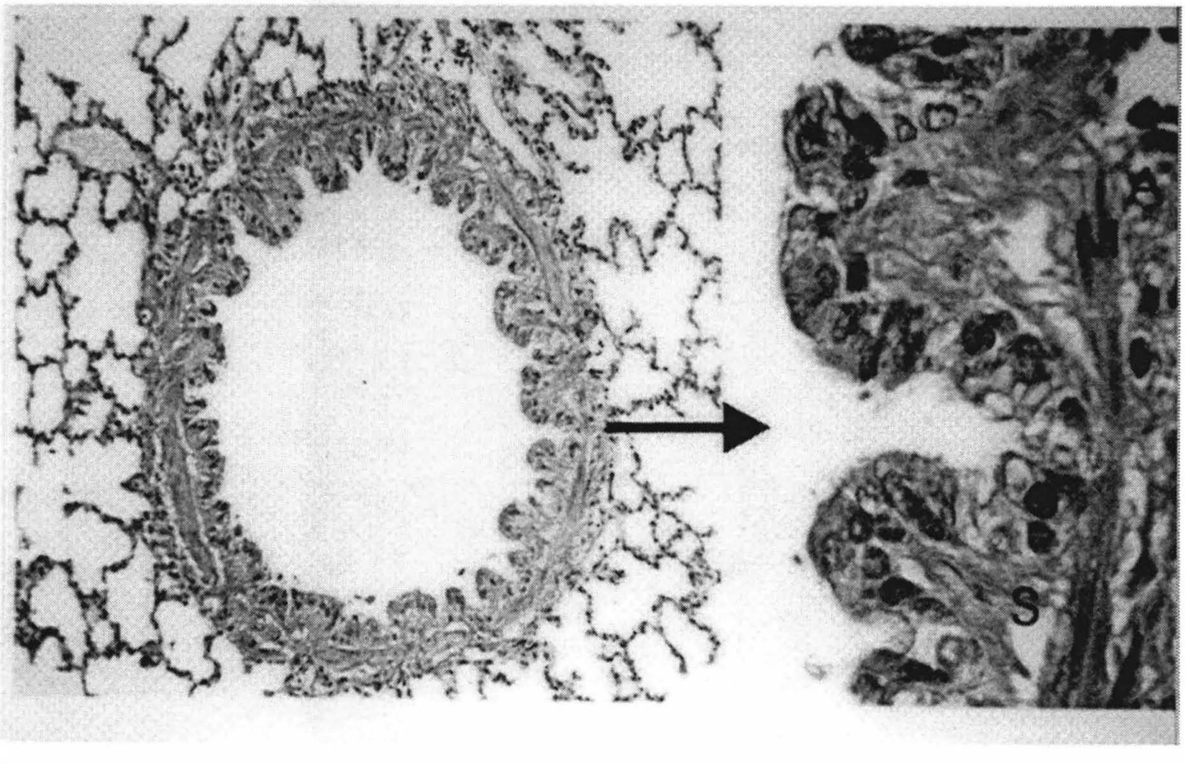

Fig. 2.1: Micrograph of section of partially collapsed rabbit airway (courtesy of Dr. M. Okazawa, Fujita Health Hospital, Japan)

The behaviour of thin-walled elastic tubes such as is observed in airways or blood vessels has been of interest for many years. In the early seventies three groups working independently first analysed elastic tubes collapsing under a pressure difference [22, 46, 60]. Lambert and Wilson analysed the case of an initially circular tube that developed two fold symmetry [60]. Kresch and Noordegraaf also examined this case and extended it to an elliptical initial state [46]. Flaherty et al also assumed an initially circular cross-section and presented results for n-fold symmetry for values of n of 2, 3 and 4 [22]. More recently Lambert presented results for up to 24-fold symmetry for pressures up to that at which opposite walls come into contact [53]. Ribreau et al have published a study of initially elliptical tubes with very high eccentricity [85]. Wiggs et al used a finite element method to study the collapse of a confined tube similar to that studied by Lambert et al [108]. This model differs from others in that the collapsing tube is embedded in a less stiff medium which absorbs some of the energy.

The analysis that is almost universally used is based on elastica theory assuming that the cross-sectional shape of the tube is uniform axially, the material of the tube is homogeneous and isotropic, the wall thickness is constant around the circumference of the tube and the thickness-to-radius ratio of the tube is very much less than unity. The applicability of these conditions to the biological systems is satisfactory as a first-order approximation. However, experiments on biological tissues have demonstrated non-linear elasticity [113]. Furthermore, it has been found that the elasticity is different in compression from in tension [113]. Examination of electron micrographs of cross-sections of airways and blood vessels clearly show that the collapsing tube is not of uniform thickness [42, 43]. It is also possible that the external force field is not uniform because of either attachments to, or contact with, other structures.

The following analysis is based on the same starting point as that of Lambert and Wilson [60] and of Flaherty et al [22]. It will be repeated for completeness and in order to provide an understanding of its extension to a non-uniform stiffness. Already published results will briefly be presented followed by the question of what determines the number of folds developing in a folding membrane.

Similar to various types of biological tissue the basement membrane might also behave differently when in tension or in compression which might also affect airway collapse. To accommodate this observation, a simple “two-layer-model” is presented followed by a discussion dealing with the applicability of this simple approach.

2.2 Mathematical analysis

2.2.1 Analysis of airway collapse

The conceptual model of a bronchus is illustrated in Fig. 2.2. The deformable region between the muscle wall and the basement membrane is essentially liquid and is modelled as being incapable of sustaining significant shear stress and bending moments. The luminal epithelium is assumed to have negligible elastic properties and has been omitted from the model.

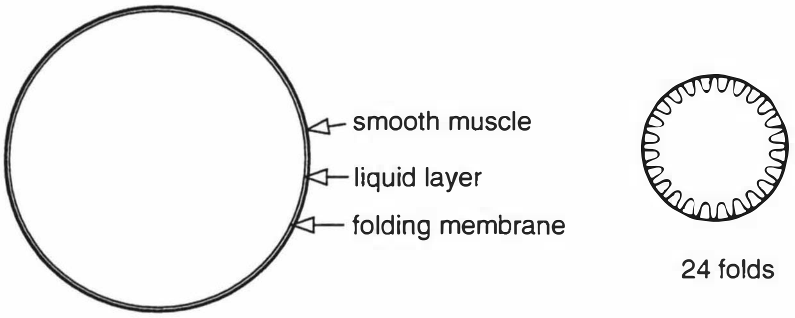

Fig. 2.2. Model bronchus with left: unbuckled basement membrane (or folding membrane) and right: developing 24 folds (adapted from reference [56]).

At this point it has to be stressed that the tube is a membrane only in a biological sense. A physical membrane is not capable of sustaining either shear forces or bending moments. The theoretical analysis presented here is based on the physics of a shell.

The governing equations describing the deformation of the tubes are obtained by analysing the static equilibrium conditions for a small segment of the tube and a constitutive (stress-strain) equation for the wall material. The free-body diagram for a small section of the tube arc length is shown in Fig. 2.3.

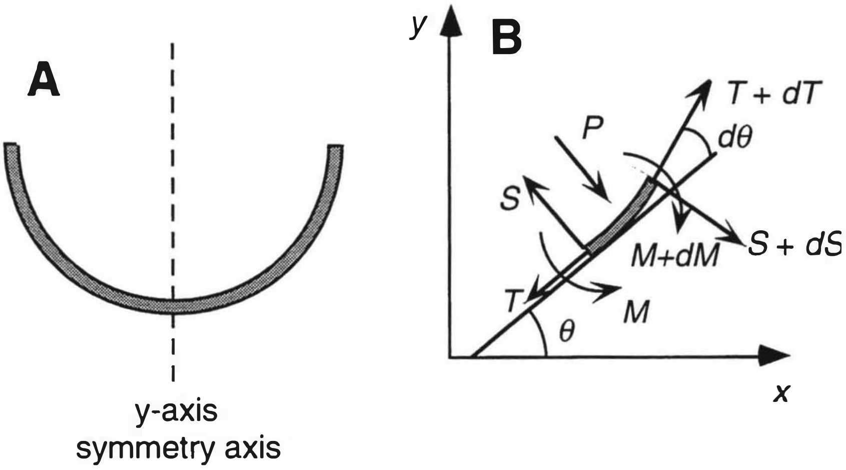

Fig. 2.3. A: Symmetry axis in fundamental two-lobe collapsing mode. B: Free-body diagram.

Summing, respectively, the tangential components of the forces, the normal components of the forces and the bending moments to zero results in Eqs. (2.1) - (2.3). In Eqs. (2.1) and (2.2) x is used to indicate the tangential direction and y the normal direction.

$$\sum F_x = 0: \qquad \frac{dT}{ds} + S\frac{d\theta}{ds} = 0 \tag{2.1}$$

$$\sum F_y = 0: \qquad \frac{dS}{ds} - T\frac{d\theta}{ds} - P = 0 \tag{2.2}$$

$$\sum M = 0: \qquad \frac{dM}{ds} - S = 0 \tag{2.3}$$

where T, S, M, P, s are the tensile force per unit axial length, the shear force per unit axial length, the bending moment per unit axial length, pressure and the arc length, respectively.

The constitutive relationship required is Winkler's development of Euler's constitutive relationship [7]. It links the difference in curvature, κ, between the deformed ($\kappa = d\theta/ds$) and the undeformed ($\kappa_0 = d\theta_0/ds$) states with the bending moment M. The flexural rigidity, D, depends on the Young modulus, E, the tube thickness, t, and the Poisson ratio, ν.

$$M = D(\kappa - \kappa_0)$$
$$D = \frac{Et^3}{12(1-\nu^2)} \tag{2.4}$$

The analysis presented by Lambert [53] is based on the assumption that D, the flexural rigidity, which determines the stiffness of the tube, is considered to be constant along the circumference of the membrane. From Eqs. (2.1) to (2.4) one can derive the "classical" differential equation for the shape of the membrane.

As a more general approach, the flexural rigidity D can be assumed to be a function of the arc length s and can be written as

$$D(s) = D_0 f(s) \tag{2.5}$$

$f(s)$ indicates a dimensionless variation of the flexural rigidity along the circumference and will be chosen to be always greater than unity. The resulting normalised differential equation written in terms of θ is then given by Eq. (2.6)

$$\begin{gathered}\theta'''' + \frac{f'''(\lambda)}{f(\lambda)}(\theta'-1) + 3\frac{f''(\lambda)}{f(\lambda)}\theta'' + 3\frac{f'(\lambda)}{f(\lambda)}\theta''' \\ -\left\{f''(\lambda)(\theta'-1) + 2f'(\lambda)\theta'' + f(\lambda)\theta'''\right\}\frac{\theta''}{f(\lambda)\theta'} \\ +\frac{P^*}{f(\lambda)}\frac{\theta''}{\theta'} + \left\{f'(\lambda)(\theta'-1) + f(\lambda)\theta''\right\}\frac{(\theta')^2}{f(\lambda)} = 0\end{gathered} \tag{2.6}$$

Here the radius R of the undeformed tube acts as the length scale, P^* is the non-dimensional pressure and λ the normalised arc length. The pressure scale is D_0/R^3. A more detailed derivation is given in appendix A. By setting D, the flexural rigidity, constant (and consequently $f(s) = 1$) the well-known, oft-solved equation for a uniform tube can be recovered.

$$\theta''''\theta' - \theta'''\theta'' + \theta''(\theta')^3 + \theta'' P^* = 0 \tag{2.7}$$

Symmetry means that solutions are required for only one half of one fold. Four boundary conditions are needed to solve either Eqs. (2.6) or (2.7).

(i) θ is arbitrarily taken to be zero at $\lambda = 0$.

(ii) Geometry and symmetry then require that $\theta = \pi/n$ at $\lambda = \pi/n$.

(iii) Symmetry requires that S be zero at $\lambda = 0$ and that

(iv) S be zero at $\lambda = \pi/n$.

where n is the number of folds into which the tube buckles. From Eqs. (2.2) and (2.4) it follows that $\theta'' = 0$, when $S = 0$.

Since the shear force has to be zero at $\lambda = 0$ and $\lambda = \pi/n$, $df(\lambda)/d\lambda$ also has to be zero at $\lambda = 0$ and $\lambda = \pi/n$ in order not to violate the boundary conditions. Furthermore $f(\lambda)$ should be smooth at $\lambda = 0$ and $\lambda = \pi/n$. Therefore a sinusoidal function was used to describe the variation of the stiffness along the circumference. Three cases were investigated involving different locations of the maximum stiffness along the integration path, which is shown in Fig. 2.4. I will use λ_0 and λ_{end} to denote the start and end of the integration path and λ_{mid} to indicate the mid-point.

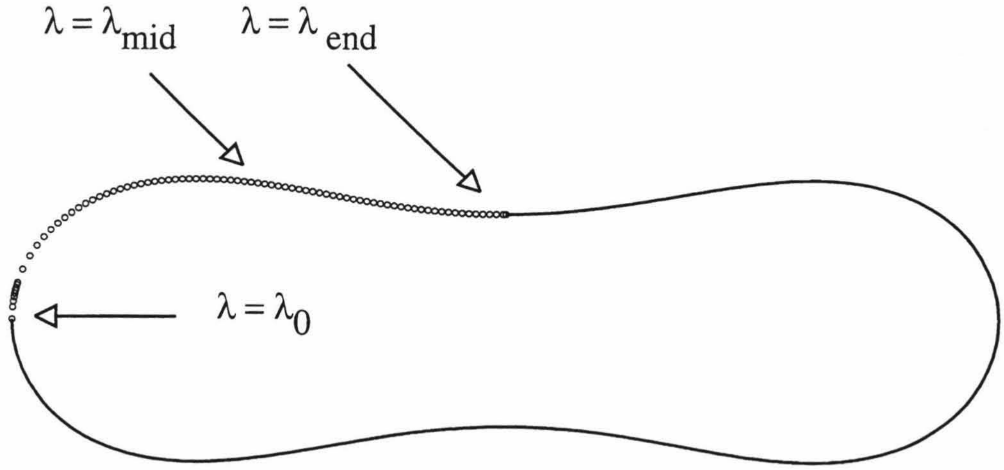

Fig. 2.4 Profile of a collapsed tube for $n = 2$, $P^* = 4.0$ and $\alpha = 0$ (uniform tube). The integration path is shown by the small circles. The rest of the profile was obtained by applying appropriate symmetry operations. The profile has been rotated 270° from that described in the text for ease of presentation.

(i) The maximum stiffness occurs at the end of the integration path (f_{max} at λ_{end}) as given by

$$f(\lambda) = 1 + \alpha \sin^2(n\lambda/2) \tag{2.8}$$

The dimensionless coefficient α can be thought of as a stiffness coefficient where α is the magnitude of the normalised stiffness variation. $\alpha = 0$ corresponds to a tube of uniform stiffness and $\alpha \neq 0$ corresponds to a non-uniform tube. The maximum flexural rigidity along the circumference is then $D_0(1 + \alpha)$.

(ii) The maximum stiffness occurs in the middle of the integration path (f_{max} *at* λ_{mid}) as given by

$$f(\lambda) = 1 + \alpha \sin^2(n\lambda) \tag{2.9}$$

(iii) The maximum stiffness occurs at the beginning of the integration path (f_{max} *at* λ_0) as given by

$$f(\lambda) = 1 + \alpha \cos^2(n\lambda/2) \tag{2.10}$$

Non-dimensional *x*- and *y*-coordinates of points on the tube wall can be calculated from θ as follows

$$\begin{aligned} x &= \int \cos\theta d\lambda \\ y &= \int \sin\theta d\lambda \end{aligned} \tag{2.11}$$

The cross-sectional area (A) enclosed by the tube can then be calculated from the following formula in which x_{end} and y_{end} denote the values of x and y at $\lambda = \pi/n$ [53].

$$A = 2n\left[\int_0^{y_{end}} x dy + {0.5x_{end}^2}\Big/{\tan(\pi/n)}\right] \tag{2.12}$$

Tubes exhibit critical buckling [99]. That is, for pressures below the critical pressure, no macroscopic deformation of the tube takes place. The critical pressure P_{cr} can be calculated analytically [99] for a uniform tube and is, in normalised units,

$$P^{*}_{cr} = n^{2} - 1 \tag{2.13}$$

2.2.2 Influence of the membrane having different elastic properties in compression than in tension

Complex biological tissue has different elastic properties in compression from those in tension [113]. This asymmetry can be incorporated into the existing model by a simplified two layer model based on a method given in a standard mechanics of materials text book [7]. Fig. 2.5 shows the simplified concept. The hoop stress in the tube is compressive because of the applied pressure field. The tube is in flexure because of its elastic collapse. The effect of the asymmetry in elastic properties can be examined approximately by adapting a standard analysis for a bar in pure bending.

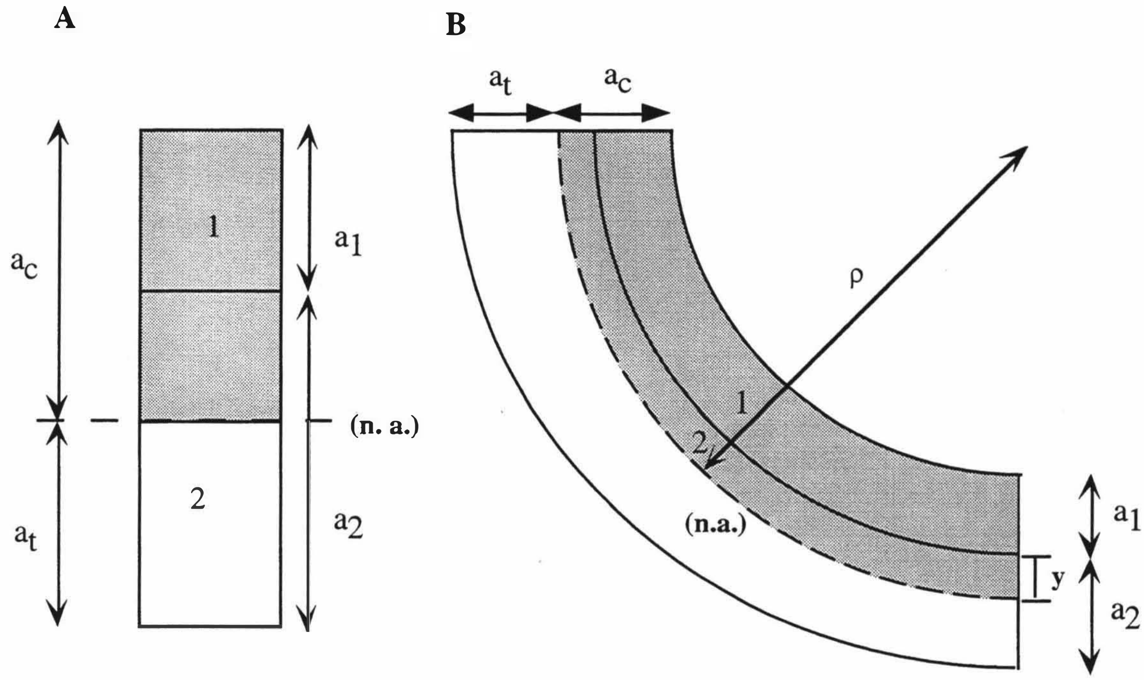

Fig. 2.5. Simplified model of bending of a bar made of two materials. The shaded regions show the sections in compression. Note that, in general, the widths (a_1 and a_2) of the different material layers do not coincide with the widths of the regions in tension (a_t) and in compression (a_c).

When a symmetric bar is subject to pure bending it will form an arc where ρ-y is the distance from the centre of the arc to the neutral axis (n.a) and y is an arbitrary radial outward distance from the neutral axis as shown in Fig. 2.5b. The longitudinal strain ε_x can be written as

$$\varepsilon_x = -\frac{y}{\rho} \tag{2.14}$$

where ρ denotes the radius of the arc (Fig. 2.5b).

The tensile circumferential stress σ_x at any distance y from the neutral axis and the bending moment are linked by the elastic flexure formula [7]

$$\sigma_x = -\frac{My}{I}. \tag{2.15}$$

where I is the second moment of area about the neutral axis and M is the bending moment. Since the moduli of elasticity E_1 and E_2 of the two different layers are different, the stress in each material at a given distance from the neutral axis will also be different.

$$\begin{aligned} \sigma_1 &= E_1\varepsilon_x = -\frac{E_1 y}{\rho} \\ \sigma_2 &= E_2\varepsilon_x = -\frac{E_2 y}{\rho} \end{aligned} \tag{2.16}$$

Generally the boundary of the material layers is not identical with the location of the neutral axis. However, complex biological tissue is not a material in a traditional sense. The neutral axis defines the boundary between the region in compression and the region in tension. Hence, the thickness of the material layers (a_1 and a_2) coincides with the "compressive thickness" a_c and the "tensile thickness" a_t.

The force dF_c exerted on an element of area dA of the upper portion of the cross section is

$$dF_c = \sigma_c dA = -\frac{E_c y}{\rho} dA \qquad (2.17)$$

The force dF_t exerted on an element of area dA of the lower portion can be obtained in the same way

$$dF_t = \sigma_t dA = -\frac{E_t y}{\rho} dA \qquad (2.18)$$

By defining

$$\eta = \frac{E_c}{E_t} \qquad (2.19)$$

as the ratio between the moduli of elasticity E_c and E_t, dF_c can be expressed as

$$dF_c = -\frac{(\eta E_t)y}{\rho} dA = -\frac{E_t y}{\rho}(\eta dA) \qquad (2.20)$$

Comparing Eqs. (2.17) and (2.20) indicates that the same force dF_c would be exerted on an element of area ηdA of the material (in tension). The resistance to bending of the bar would remain the same if both portions were made of the same material, providing that the width of each element of the lower portion were multiplied by η. The new cross section obtained in this way is called the *transformed* section. Consequently, $\eta > 1$ leads to widening and $\eta < 1$ leads to narrowing of the upper cross section as shown in Fig. 2.6.

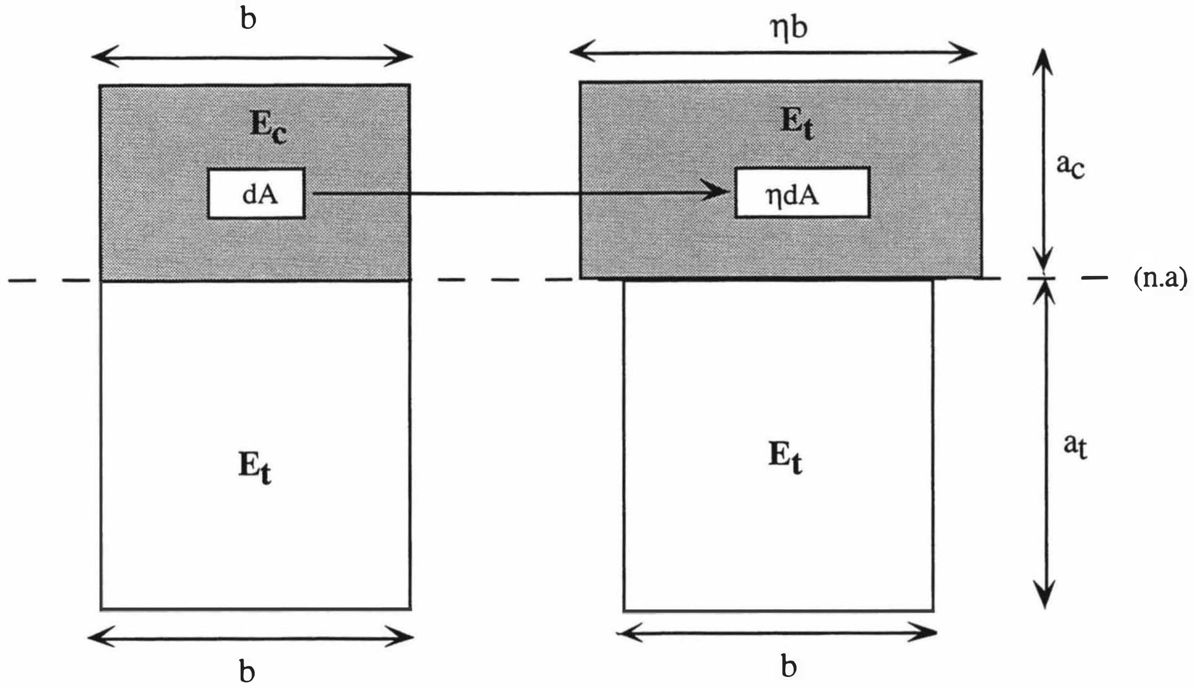

Fig. 2.6. Transformation of cross-section as a consequence of the different moduli of elasticity. The shaded region is in compression. Note that the location of the neutral axis (n. a.) coincides with the boundary between the compressive and the tensile layers.

The stiffness of the composite can be expressed in terms of the flexural rigidity *D* as [99]

$$D = \frac{E_t I_A}{1 - v^2} \tag{2.21}$$

which means that the influence on the stiffness caused by the asymmetry can be determined by calculating the second moment of area I_A of the transformed area.

The second moment of area of a composite shape such as the transformed cross-section is given by [7]

$$I_A = \frac{1}{3} b(a_t^3 + \eta a_c^3) \tag{2.22}$$

where the neutral axis is the line of intersection of the two areas.

The location of the neutral axis also dictates the location of the centroid, resulting in

$$A_t \frac{a_t}{2} = A_c \frac{a_c}{2} \tag{2.23}$$

which gives

$$a_t^2 b = \eta b a_c^2 \tag{2.24}$$

By using Eq. (2.24) the thickness of the layer in compression a_c and the thickness of the layer in tension a_t can be calculated by using $t = a_t + a_c$ for unit length ($b = 1$)

$$\begin{aligned} a_c &= \frac{t}{1+\sqrt{\eta}} \\ a_t &= \frac{t}{1+\frac{1}{\sqrt{\eta}}} \end{aligned} \tag{2.25}$$

Eq. (2.22) becomes

$$I_A = \frac{1}{3} \frac{t^3}{\left(1+\frac{1}{\sqrt{\eta}}\right)^2} \tag{2.26}$$

Hence, the flexural rigidity D per unit length is

$$D = \frac{1}{3} \frac{E_t}{1-v^2} \frac{t^3}{\left(1+\frac{1}{\sqrt{\eta}}\right)^2} \tag{2.27}$$

Therefore it follows that

$$D = \frac{E_t t^3}{12(1-\nu^2)} \cdot \beta(\eta)$$
$$\beta(\eta) = \frac{4}{\left(1 + \frac{1}{\sqrt{\eta}}\right)^2} \tag{2.28}$$

2.3 Numerical methods

Eqs. (2.6) and (2.7) are two-point boundary value problems and have to be solved numerically.

Generally, two standard methods are used to solve two-point boundary problems, the shooting and the relaxation method [82]. Since shooting provides a relatively simple implementation, the shooting method was preferred. Standard shooting is based on numerical integration of the equation from a starting point x_1 to a final point x_2 by using known and guessed initial values at x_1. Upon completion of the numerical integration, the final values at x_2 are used to estimate the discrepancy between the actual and the required values at x_1. By varying the initial values at x_1 the numerical integration is repeated until the discrepancy at x_2 is within an acceptable tolerance. Published results based on Eq. (2.7) have been obtained by using this method [53]. However, in the case discussed here, the standard shooting method failed due to the highly non-linear and sensitive behaviour of Eq. (2.6). For this reason shooting was performed by using a biased random walk method based on simulated annealing [14, 68, 82]. Simulated annealing requires a cost function, CF, which is used as a quantitative measure of the closeness of an arbitrary configuration to the optimised "ground state". I specified CF to be

$$CF = k_1\left(\frac{\Delta\theta}{\theta}\right)^2 + k_2(\Delta\theta'')^2 \tag{2.27}$$

where $\Delta\theta \,/\, \theta$ is the relative error in the angle θ and $\Delta\theta''$ is the absolute error in θ'' evaluated at λ_{end}. The parameters k_1 and k_2 served the purpose of adjusting the different magnitudes of the errors in order to provide a more-or-less uniform convergence of both terms towards the required accuracy $(\Delta\theta/\theta) < 10^{-3}$ and $\Delta\theta'' < 0.02$ at λ_{end}. The actual numerical integration was performed by using the Bulirsch-Stoer method [82]. The actual algorithm used is described more in detail in the appendix.

The use of good initial guesses almost guarantees a fast convergence of the shooting method. The correct initial values for Eq. (2.6) were expected to be in the vicinity of the known initial values of the homogeneous Eq. (2.7). Therefore systematic probationary integrations within a certain interval of the known initial guesses were performed. The initial guess with the least error at the end of the integration was used as an initial guess for the shooting method.

2.4 Results of computations

Solutions were obtained in terms of arc length around the tube wall and the angle that the tangent to the arc made with the horizontal at that arc length. From these data the x- and y- components of the points on the wall and the area inside the tube were calculated. Solutions for a uniform tube have been obtained from 2 to 24 folds. Solutions for a non-uniform tube could only be obtained for the simple "two-lobe" case (n = 2). Computations were started from the critical buckling pressure P_{cr}^{*} for the homogeneous tube up to the pressure at which opposite sides of the tube came into contact. As expected no solution other than the circular could be obtained at pressures below P_{cr}^{*}.

Figs. 2.7 to 2.9 summarises the results of the numerical computations for the uniform Eq. (2.7). Fig. 2.7 demonstrates how an entire folding pattern is constructed on a four-fold collapse. A more complex collapse (n = 20) is shown in Fig. 2.8. Fig. 2.9 shows the area-pressure curves starting from the critical pressure P_{cr}^{*} to the "wall-touching pressure" P_{c}^{*} for various numbers of folds.

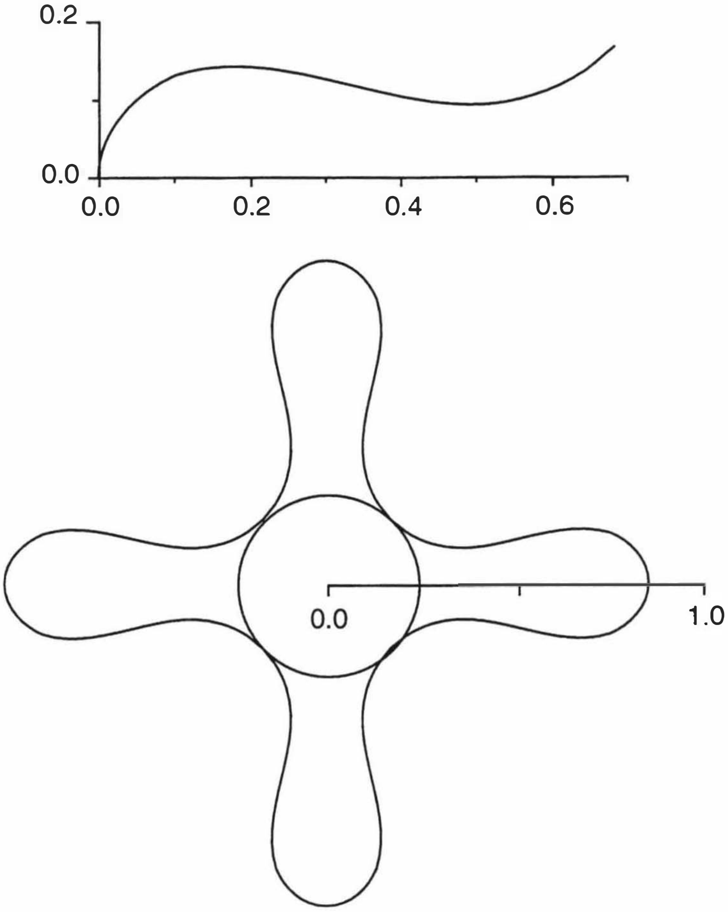

Fig. 2.7. Top: Result of integration of one half fold for $n = 4$. Scales are normalised on radius of undeformed tube. Bottom: tube cross section obtained by appropriate rotations of upper plot (adapted from reference [53]).

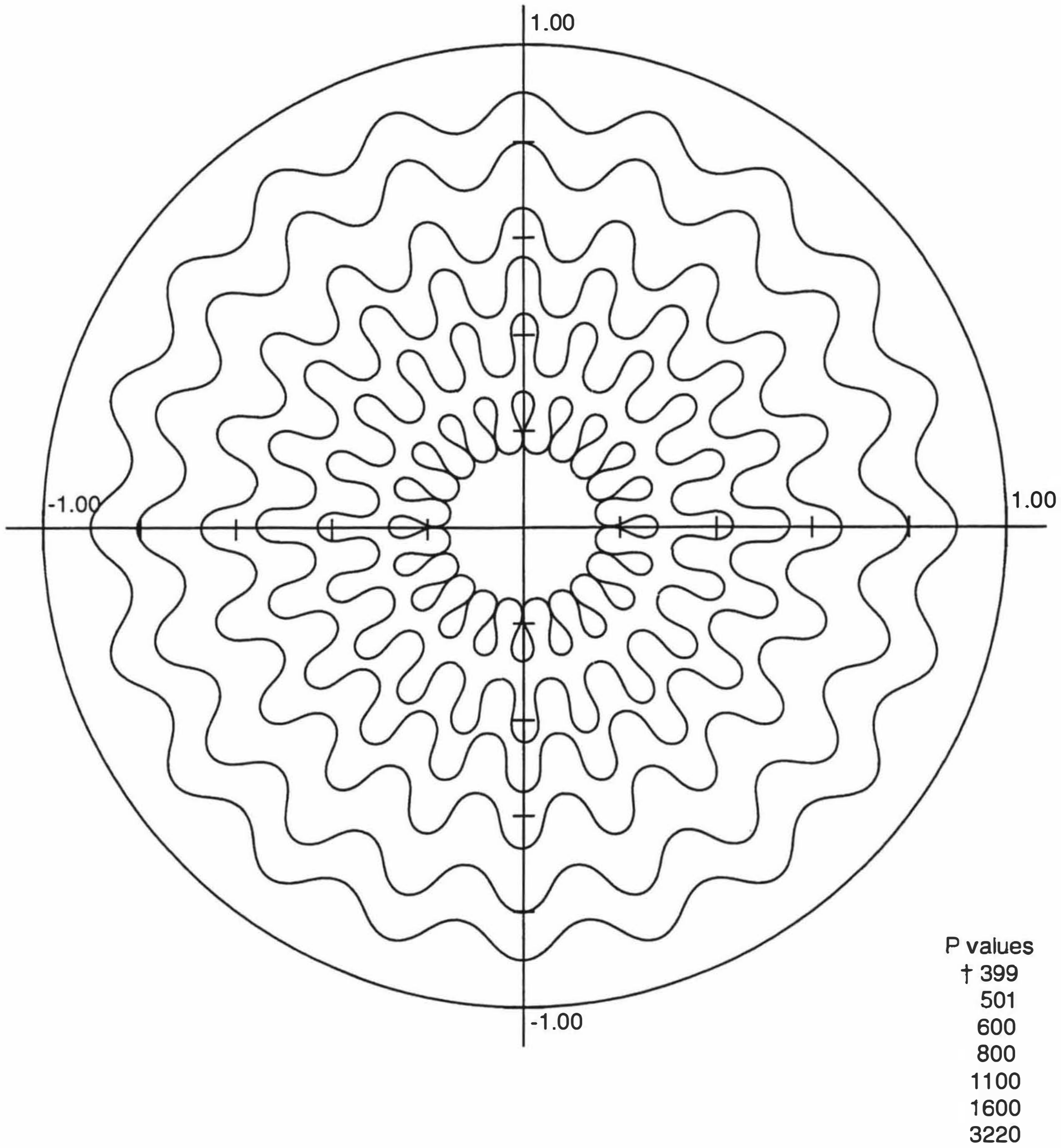

Fig. 2.8. Tube cross sections for the case of 20 folds at various pressures. Each cross section has the same circumference as undeformed tube. Non-dimensional transmural pressure differences, starting from outermost cross section, are ≤ 399, 501, 600, 800, 1100, 1600 and 3220. At $P^* = 3220$, opposites sides of a fold first touch (adapted from reference [53]).

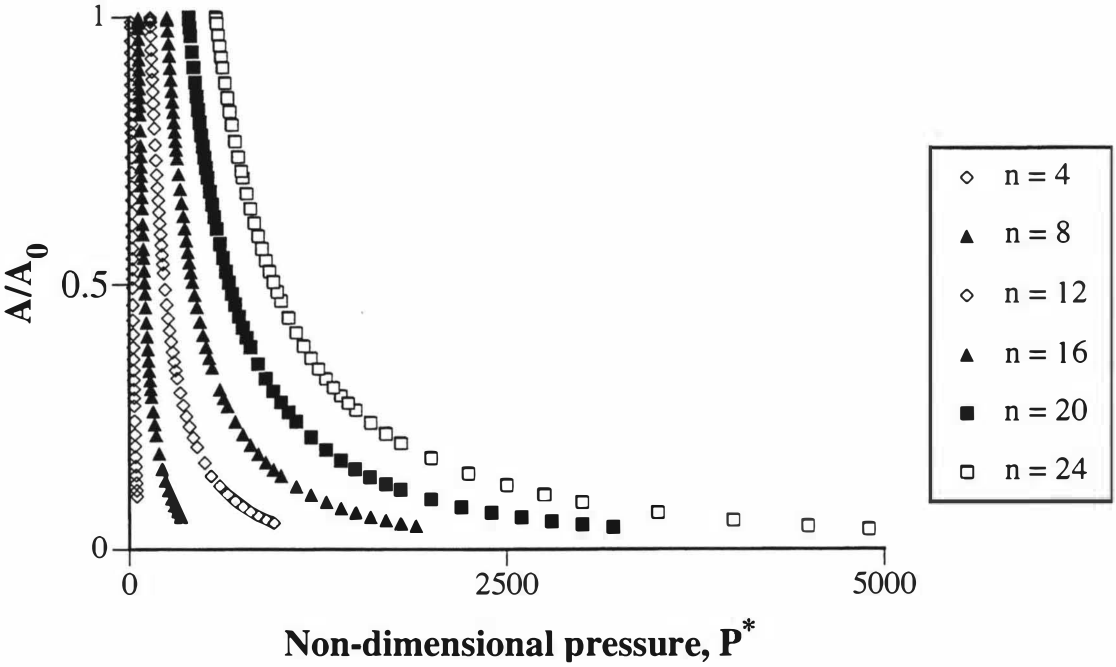

Fig. 2.9. Area-pressure curves for six folding patterns. Area has been normalised on area of undeformed tube (adapted from reference [53]).

Numerical solutions for the non-uniform case, Eq. (2.6) for the case of n = 2 were obtained for increasing values of P^* starting from the critical buckling pressure, P^*_{cr}, for the homogeneous shell case ($P^*_{cr} = n^2 - 1$ for $\alpha = 0$) up to the pressure at which opposite sides of the tube came into contact, P^*_c. P^*_{cr} for $\alpha > 0$ was always greater than P^*_{cr} for $\alpha = 0$. Solutions of the $\alpha = 0$ case were consistent with the previously published results. Solutions were obtained for values of α of 0, 0.3, 0.5 and 1.0. The case of α = 1.0 can be thought of as corresponding to the case of a constant Young modulus E and a maximal increase in thickness of about 26 % ($D \sim t^3$).

Fig. 2.10 show tube profiles at $P^* = 5.2$ (the value of P^*_c for $\alpha = 0.0$), $n = 2$ and $\alpha = 0.0, 0.3, 0.5, 1.0$ obtained using the three stiffness distributions. Fig. 2.11 shows the curves of luminal area, A (normalised on the undeformed area, A_0), vs P^* for the three stiffness functions. The change in critical buckling pressure with α is shown in Fig. 2.12. Fig. 2.13 shows the change of cross-sectional area with α at P^*_c.

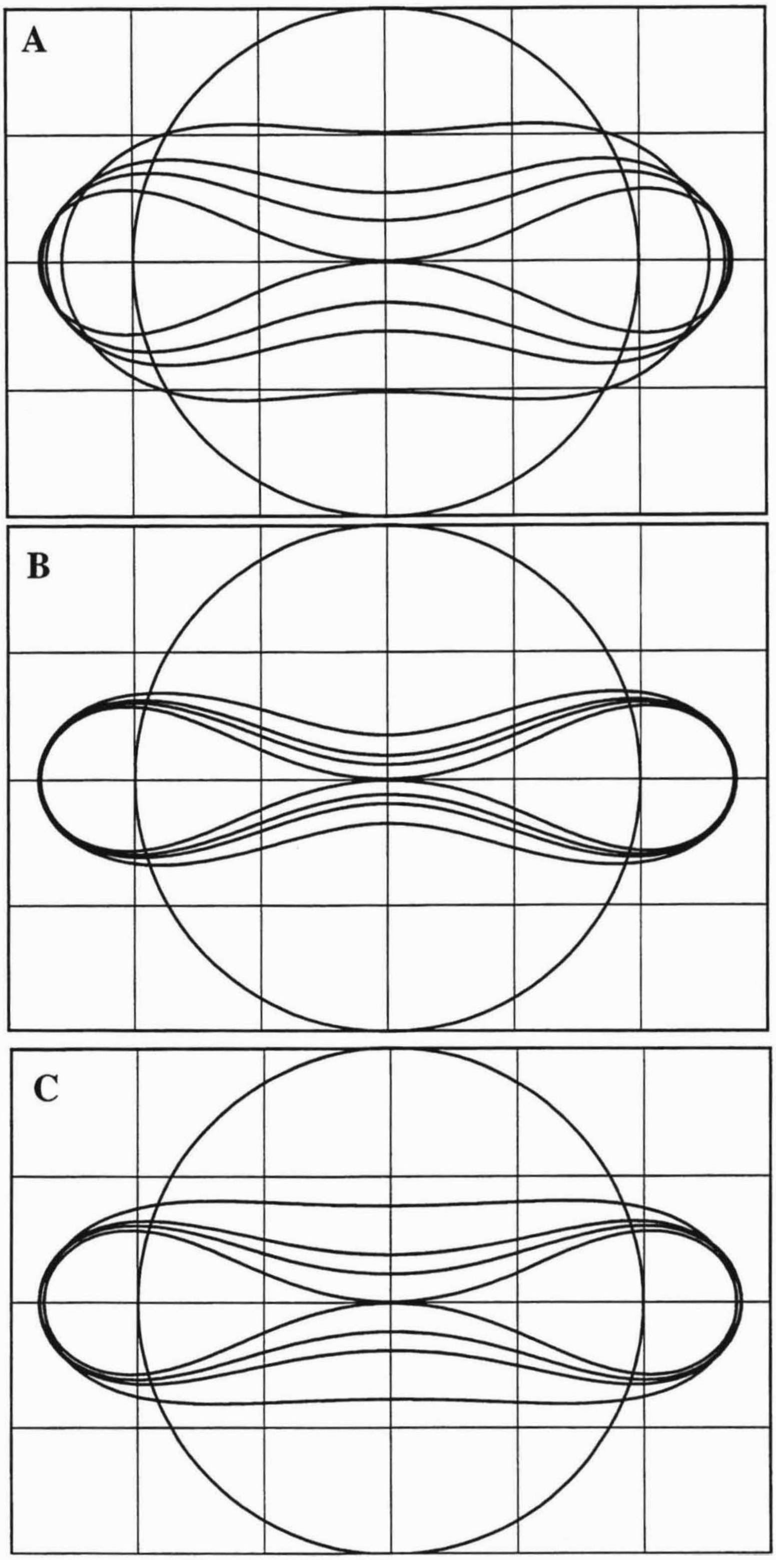

Fig. 2.10. Calculated profiles of a collapsed tube for $n = 2$, $P^* = 5.2$, and four values of α: 0.0, 0.3, 0.5, 1.0. The circle is the undeformed profile and α increases from 0.0 for the most deformed case to 1.0 for the least deformed. A: f_{max} at λ_0; B: f_{max} at λ_{mid}; C: f_{max} at λ_{end}.

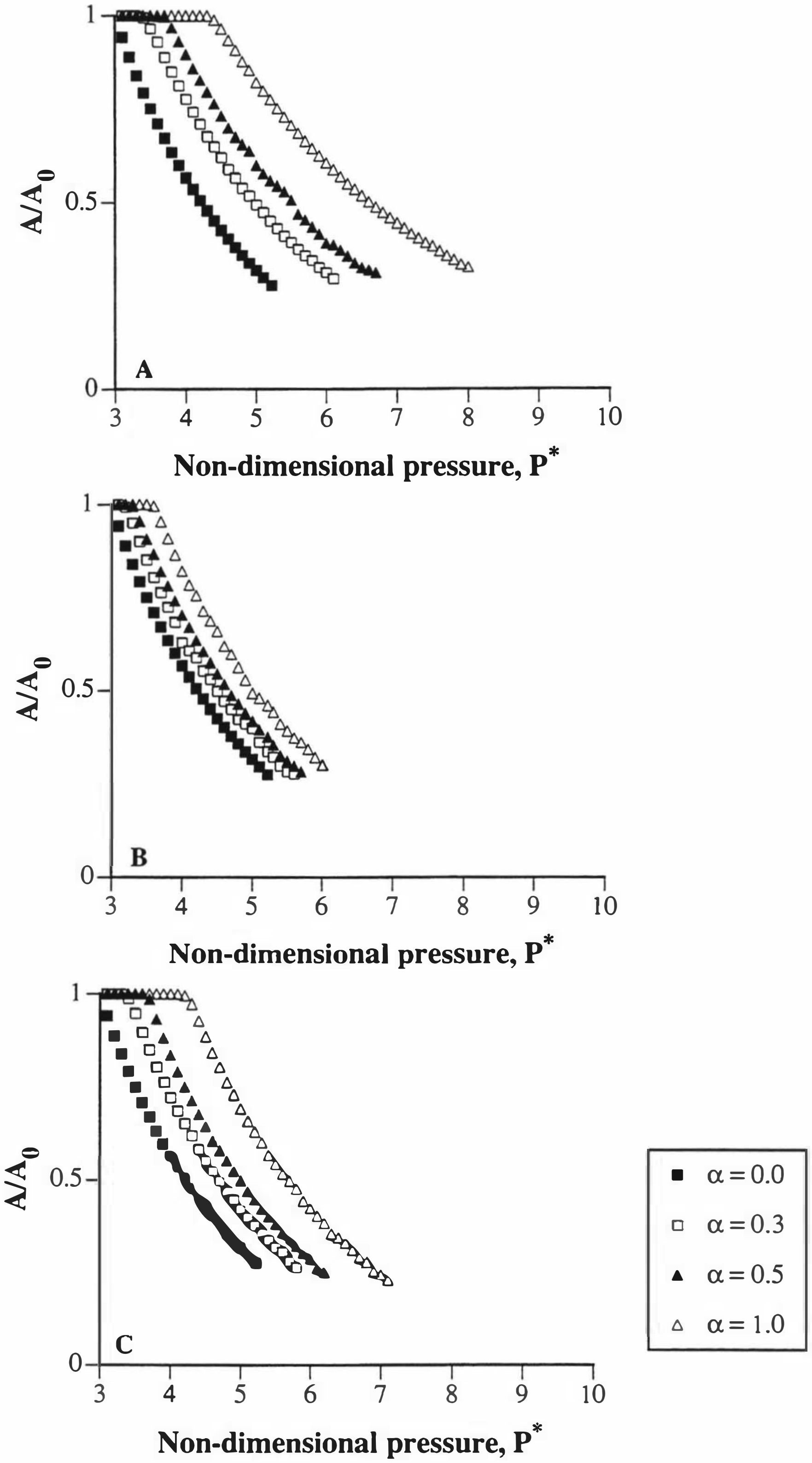

Fig. 2.11. Compliance curves for the four values of α. The cross-sectional area of the tube (A) has been normalised on the area of the undeformed circle (A_0). A: f_{max} at λ_0; B: f_{max} at λ_{mid}; C: f_{max} at λ_{end}.

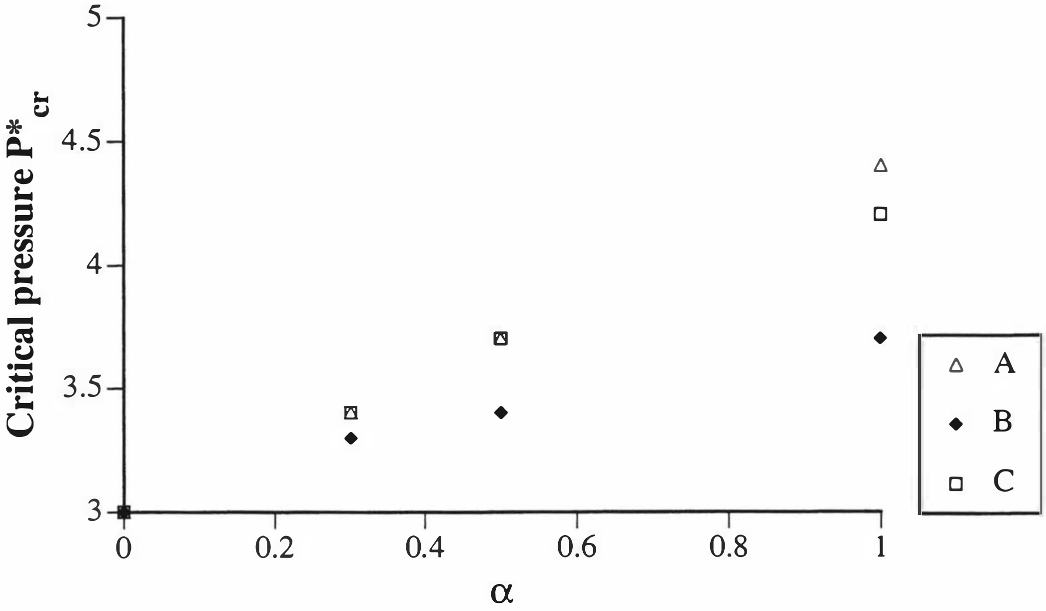

Fig. 2.12. Critical buckling pressure (P_{cr}^{*}) as a function of stiffness coefficient (α) for the three stiffness distributions. A: f_{max} at λ_0; B: f_{max} at λ_{mid}; C: f_{max} at λ_{end}.

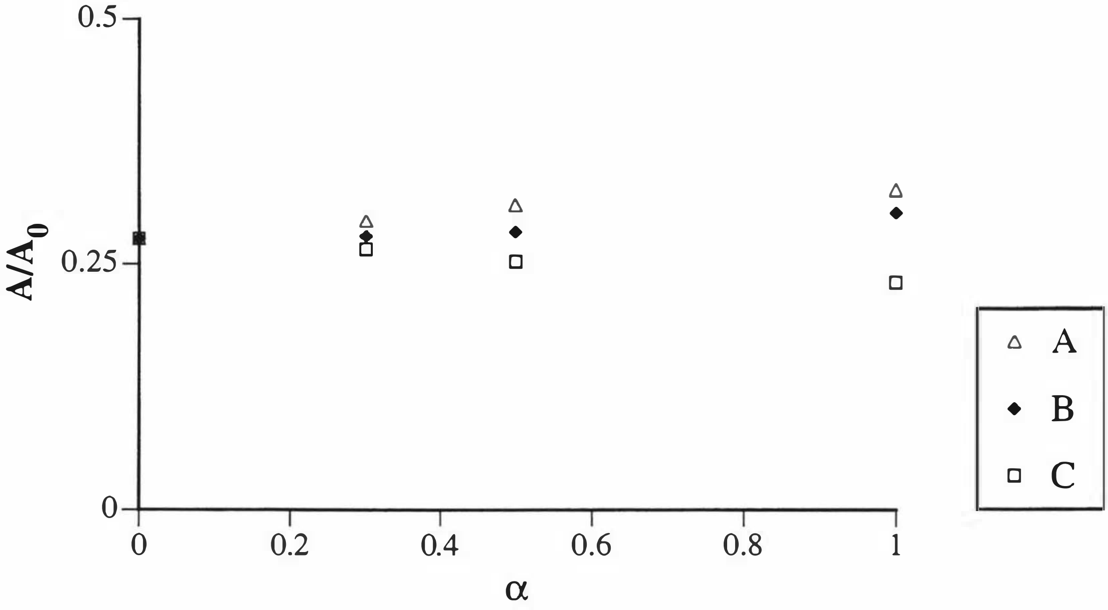

Fig. 2.13. A/A_0 at the contact pressures (P_c^{*} - see text) for the three stiffness distributions. A: f_{max} at λ_0; B: f_{max} at λ_{mid}; C: f_{max} at λ_{end}.

The function $\beta(\eta)$ (Eq. 2.28) which determines the flexural rigidity (D) of a composed area as derived in 2.2.2 is shown in Fig. 2.14.

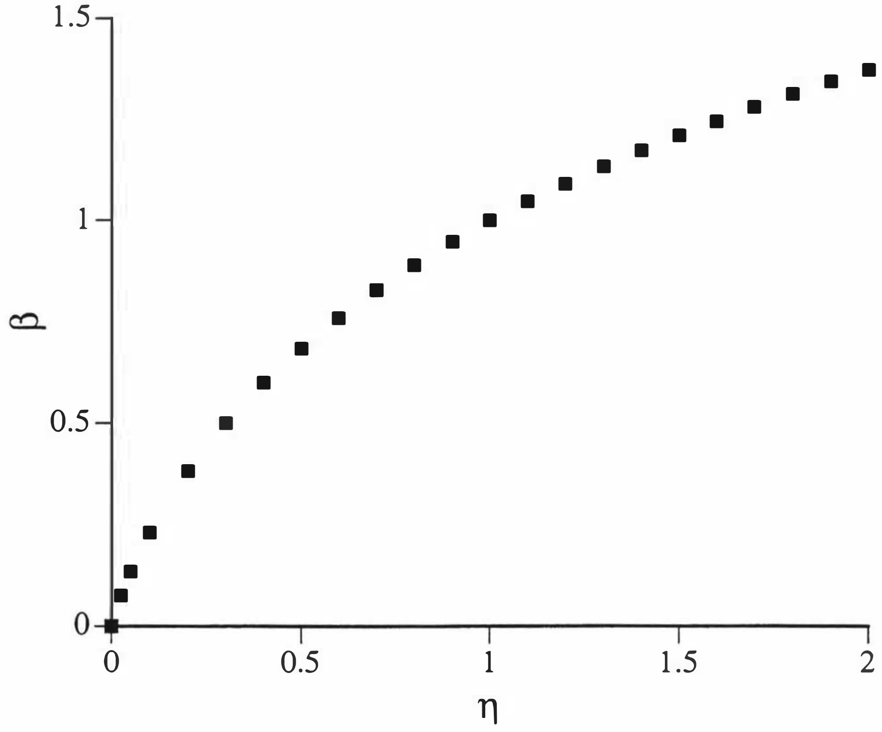

Fig. 2.14. Function β relating change of flexural rigidity of the composite area D, to the ratio of compressive and tensile moduli $\eta = E_c/E_t$. E_t is Young modulus of layer in tension. Further details see text.

2.5 Discussion

Non-uniform stiffness

Lambert showed in his paper that the basement membrane is a load bearing structure and that its load bearing ability increases with the number of folds into which the tube collapses [53]. One possible answer to the question of what determines the number of folds on airway collapse was extensively discussed in a paper by Lambert et al [56]. They postulated, as an extension of Lambert's theory [53] that the number of folds that develop during airway collapse depends on the degree of narrowing rather than being constant as was initially suggested. They proposed that the number of folds, n, is governed by a combination of minimum energy requirement and geometric constraints of the muscle boundary and the constant volume of tissue in the submucosa.

A further option of what determines, at least the initial number of folds is the possibility of a non-homogeneous basement membrane. This hypothesis has been investigated by extending the model initially presented in [53] by allowing the stiffness D to be non-uniform along the circumference of the tube. Although scanning electron microscopic examinations, for example, have shown that there are changes in thickness along the circumference, there are no data available about any possible regularity or pattern in the changes in thickness (if there is any) [42, 43]. The approach presented here of a periodic change of stiffness is, therefore, purely hypothetical. The idea behind introducing such a change in stiffness is to investigate the change in the compliance of a tube with various stiffness distributions. The stiffness coefficient α determines the maximal stiffness along the circumference and is $D_{max} = D_0(1 + \alpha)$.

Due to the highly non-linear nature of Eq. (2.6) only solutions for the fundamental "two-lobe" folding were obtained. However, mathematically, there is no difference between the fundamental $n = 2$ folding and any higher number of folds. One can therefore expect the same behaviour for any number of folds $n > 2$. As is to be expected, with increased stiffening ($\alpha > 0$) the compliance curves move to higher pressures. The most significant features are that P_{cr}^* increases with increasing α, but the slopes are essentially unchanged. The shift in P_{cr}^* appears to depend on the location of the region of maximal stiffness. When this region is either at λ_0 or λ_{end} (as shown in Fig. 2.4), P_{cr}^* is the greatest and the two cases are essentially indistinguishable over the investigated range. Buckling will start as soon as the critical pressure P_{cr} is exceeded.

Thus, the tube will collapse into the configuration with the lowest critical buckling pressure.

The examples of profiles of collapsed tubes (Fig. 2.10) show the influence of the different stiffness distributions on the cross-sectional shapes of the collapsed tube. An interesting point that reflects the effect of the stiffness distribution on shape is illustrated in Fig. 2.13. To plot this, the normalised area at the highest pressure point from each of the curves in Fig. 2.11 was taken and was plotted against α. This shows the cross-sectional area at P_c^* for each case. Whereas this area, in the f_{max} at λ_{end} case decreases with increasing α, the two other cases (f_{max} at λ_0 and f_{max} at λ_{mid}) show the opposite behaviour. This can be attributed to the change of curvature around the circumference. The f_{max} at λ_{end} case is stiffest at the vertical symmetry axis (as drawn in Fig. 2.4) of the collapse and is consequently less curved in these segments of the tube. With increasing stiffness (increasing α) these segments tend to become even straighter and thus force a decrease in the cross-sectional area. The opposite happens in the cases of f_{max} at λ_0 and f_{max} at λ_{mid}. The decreased curvature at the beginning of the integration path forces an increase in the curvature at λ_{end} and therefore the area increases with increasing α.

The compliance curves (A/A_0 vs. P^*, Fig. 2.11) show some lack of smoothness in the calculated cross-sectional areas for $\alpha > 0$. This is a result of the considerably more complicated differential equation when $\alpha \neq 0$. The sensitivity of the solutions to the initial conditions required the use of simulated annealing as well as a relaxation of the error tolerances compared with published solutions ($\Delta\theta/\theta < 10^{-5}$, $\Delta\theta'' < 0.01$ [53]). This appears to have resulted in some numerical noise in the results. The relaxation in the error tolerances has also lead to a reduced accuracy in the critical buckling pressures as depicted in Fig. 2.12. This explains why the critical buckling pressures for the cases A and C at $\alpha = 0.5$ are identical.

When applying these more general findings to non-cartilaginous airways one can conclude that the stiffness distribution of the basement membrane plays a certain role during a collapse. The computations show that, when the smooth muscle shortens and therefore generates a pressure difference across the wall, the basement membrane will show its initial macroscopic deformation at the weakest spot of the basement membrane followed by the next less weak spot etc. This suggests that the distribution of weak spots along the circumference might determine at least the initial number of folds in an early stage of collapse. In a more collapsed state the concept of geometric constraints as discussed in [56] might be the governing factor that determines the number of folds. An alternative explanation that has not yet been explored quantitatively, is the possibility of a uniform pressure field across the wall combined with some additional constraints. The membrane, for example, might be tethered in some way to the smooth muscle at several points around its circumference [53]. The tethering would force infolds to develop between adjacent tethers, thus controlling the membrane's collapse mode. This could prevent the membrane collapsing at a weak spot, thus forcing the collapse to be started at another, less weak, spot. Initial deformations ("dents") in the basement membrane could also affect the membrane's collapsing mode. For example Mitzner and Wagner showed that, in the airways of normal sheep, there is a blood vessel at the base of most, if not all, folds [70]. The presence of such vessels could well be a sufficient, but not a necessary, condition for the location of a fold [102]. However, the extensive theoretical analysis required to explore both hypotheses is beyond the scope of this work and theses might be issues to be addressed in the future.

Different elastic properties of basement membrane

When a beam becomes subject to bending or flexure the transversal section can be subdivided into a layer which is in compression and one in tension [7, 99]. When applying this principle to biological tissues one has to consider that in a variety of biological materials such as bones or various cartilage types the modulus of elasticity is different in tension than in compression [113]. Whereas no data exist for the elastic properties of basement membrane in compression, extrapolation from these other biological materials is at least suggestive that the properties might be different from the tensile properties. Eq. (2.28) expresses the flexural rigidity D of the composite structure as a function of the Young modulus E_t (in tension) and a function $\beta(\eta)$ that describes the influence of the second layer. $\eta = E_c/E_t$ is the ratio between the two Young moduli. Three cases are of interest.

(i) $E_t = E_c$. ($\eta = 1$), hence, $\beta = 1$ resulting in $D = Et^3/12(1-v^2)$ which is the classical equation for the flexural rigidity D of a structure having identical linear stress-strain curves for tension and compression.

(ii) $E_t > E_c$ ($\eta < 1$), hence $\beta < 1$, resulting in a reduced stiffness of the composite structure.
(iii) $E_t < E_c$ ($\eta > 1$), hence $\beta > 1$, resulting in an increased stiffness of the composite structure.

The asymmetry of $\beta(\eta)$ deserves some explanation. The resistance to bending is governed by the compressive stiffness of the composite and thus E_c and a_c of the layer in compression. $\eta < 1$ results in a reduced net stiffness D and thus in a reduced ability to withstand bending. The limiting case $\eta = 0$ results in $\beta(\eta) = 0$ and thus $D = 0$, no resistance to bending since $E_c = 0$. The opposite case, $\eta > 1$, results in an increased net stiffness of the composite. Interestingly, $\eta \rightarrow \infty$ gives $\beta(\eta) = 4$, a finite value thus resulting in a finite value for D of the composite. However, both limiting cases, imply that either a_c or a_t are infinitely small since $a_t^2 = \eta a_c^2$ (Eq. 2.23) and the thickness of the composite $t = a_c + a_t$ finite, lead to non-physical situations. For any practical applications one can assume η is in a reasonably narrow and finite range. Wet bones, for example are known to have a ratio of E_c/E_t in the range of about 0.4 to 0.5 [113].

The analysis assumes that tissue has a linear stress-strain behaviour in tension as well as in compression which is reasonable for sufficiently small flexures and therefore small strains in thin materials. Codd et al. for example showed that the stress-strain curve of ovine trachea wall is linear up to a strain of about 0.2 [12]. However, for highly folded and thus highly curved materials, such as airway basement membrane in an advanced state of collapse the resulting strains might already be outside the linear range, making this approach, at best, only a first order approximation.

What are the implications for airways? Non-collapsed bronchioles can be considered to have a circular basement membrane [5]. A transmural pressure difference P less then the critical pressure P_{cr} will force the basement membrane into a state of compression indicating a constant flexural rigidity along the circumference of the basement membrane. The situation becomes more complicated when P exceeds the critical pressure P_{cr}. When moving along the perimeter of the basement membrane the membrane of a partially collapsed airway can be subdivided into an inner as well as an outer layer. They undergo a periodic change from a state of compression into a state of tension and vice versa with increasing arc length. However, this has little effect on D since the membrane is a single material although there must be a sudden transition in the location of the neutral layer in the region of curvature reversal. This occurs where κ becomes equal to κ_0 implying that the internal bending moment M becomes zero since $M = D(\kappa - \kappa_0)$. This indicates that the basement membrane is, at these points, in a state of pure compression, caused by the pressure field. This also implies that, at these points, the neutral axis ceases to exist. This results in a periodic change of stiffness along the perimeter of the basement membrane. A quantitative estimate of the implications can not be provided since there are no data available stating the compressive strength of bronchial basement membrane. The net stiffness D in Eq. (2.28) is defined in terms of the tensile stiffness. It is very likely that, similarly to other biological tissue [113], the membrane is stiffer in compression than in tension. This would stiffen the entire structure and thus the folds would be in a slightly less collapsed state.

In conclusion, asymmetric stress-strain behaviour affects airway collapse, even though the effect is likely to be of only minor influence.

3. An analysis of tracheal mechanics

3.1 Introduction

Area - transmural pressure (A-P) relationships of all airways are crucial in understanding the nature of flow through the bronchial tree, especially when flow limiting mechanisms are investigated. Chapter two presented an analysis of noncartilaginous bronchioles that are located distally at the end of the air conducting zone of the bronchial tree. Modelling of more centrally located cartilaginous airways has not been attempted because of the lack of a regular structure. The trachea, however, is an attractive airway for mechanical analysis because of its reasonably regular and well-defined structure. Although there have been many roentgenographic, CT and fibreoptic studies of normal as well as abnormal tracheal behaviour, only a few have produced reliable A-P data [26, 29, 62, 76, 89, 95]. There has only been one attempt to analyse the mechanics of the trachea from the standpoint of theoretical mechanics [8]. This study was limited by both the modelling technique used and the available computer power.

The model developed to analyse tracheal mechanics is an adaptation of the analysis already used with non-cartilaginous bronchioles presented in chapter two. This adapted analysis will be used to compute A-P curves of both normal and abnormal tracheae. The model will be applied to investigate effects on the tracheal A-P curve of posterior membrane tension and length, cartilage shape and elasticity, and localised weakening of the cartilage.

3.2 Tracheal Mechanics

3.2.1 Analysis of deformation of cartilage

In principle, a trachea consists of horseshoe shaped cartilage "rings", a membrane containing smooth muscle that, in humans, joins the tips of the horseshoes, and intercartilaginous tissue that connects the adjacent horseshoes with each other. A schematic drawing of a trachea is shown in Fig. 3.1. Bronchoscopic photographs of human tracheae are shown in [18].

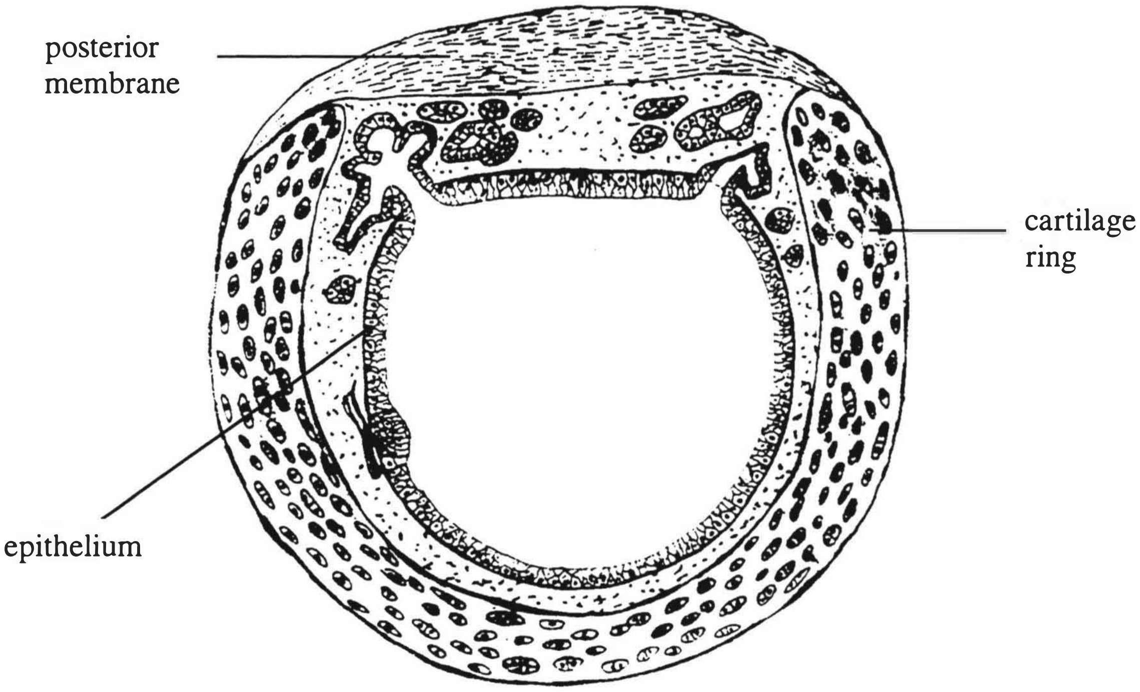

Fig. 3.1. Schematic drawing of a trachea (courtesy of Dr. R. Pack, Institute of Food, Nutrition & Human Health, Massey University).

The cartilage-membrane system can be deformed in two ways. (1) The muscle shortens ($L<L_1$, as shown in Fig. 3.2B, where L_1 is the maximum, fully relaxed length of the posterior membrane) and generates tension that forces the cartilage tips together and thus deforms the cartilage. (2) A transmural pressure difference P across the trachea wall causes the posterior membrane to invaginate ($P < 0$) into the lumen of the cartilage or to expand out of the lumen ($P > 0$). The invagination or expansion of the posterior membrane can happen at any state of contraction $L \leq L_1$. These possible deformations are shown in Fig. 3.2.

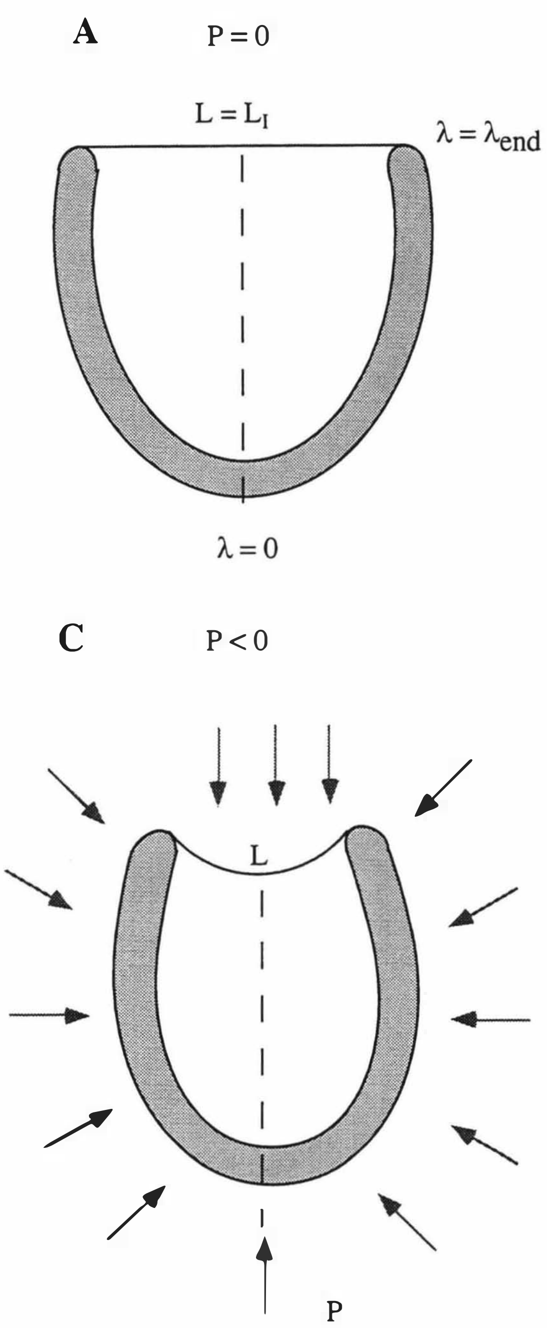

Fig. 3.2. Possible deformations a tracheal ring can undergo. A: basic structure of cartilage and posterior membrane. B: Shortening of the posterior membrane. C: The external pressure field causes an invagination ($P < 0$) of the posterior membrane. D: The posterior membrane expands out of the lumen area ($P > 0$).

The governing equations describing the deformations of the cartilage are based on the physics of a beam and have already been presented in detail in chapter two. Since the cartilage horseshoe hardly ever has an ideal semi-circular shape, that is, the curvature in the undeformed state (κ_0) varies around the "horseshoe" Eq. (2.6) had to be further generalised thus allowing the curvature (κ_0) to be a function of the (normalised) arc length. This yields Eq. (3.1) which is the normalised differential equation describing the deformation of the cartilage. θ is the angle, the cartilage makes with the reference direction and a prime indicates differentiation with respect to the normalised arc length λ. A more detailed derivation is given in appendix A.

$$\begin{aligned}&\theta'''' + \frac{f'''(\lambda)}{f(\lambda)}(\theta-\theta_0)' + 3\frac{f''(\lambda)}{f(\lambda)}(\theta-\theta_0)'' + 3\frac{f'(\lambda)}{f(\lambda)}(\theta-\theta_0)''' - \\ &\{f''(\lambda)(\theta-\theta_0)' + 2f'(\lambda)(\theta-\theta_0)'' + f(\lambda)(\theta-\theta_0)'''\}\frac{\theta''}{f(\lambda)\theta'} + \\ &\frac{q}{f(\lambda)}\frac{\theta''}{\theta'} + \{f'(\lambda)(\theta-\theta_0)' + f(\lambda)(\theta-\theta_0)''\}\frac{(\theta')^2}{f(\lambda)} = 0\end{aligned} \tag{3.1}$$

Eq (3.1) is normalised on the radius R of an initially semi-circular cartilage acting as the length scale. q is the non-dimensional pressure and $f(\lambda)$ is a function that allows the introduction of inhomogeneities through their effect on the flexural rigidity of the cartilage as was done in chapter two. The normalisation factor for pressure is D/wR^3 where $D = E_C I_A$ and E_C is Young modulus for the cartilage, w is the width of the cartilage ring and I_A is the second moment of area of the cross-sectional area (the "cut" through the cartilage ring) of the cartilage. The x and y coordinates of the cartilage ring can by computed by applying Eq. (2.11). At this point it has to be mentioned that Chapter two and three use different symbols for non-dimensional pressure. The reason for that is a different conversion between non-dimensional pressure and actual pressure. The analysis presented in chapter two is based on an elastic tube of infinite length and uses pressure/unit length. Chapter three is based on an elastic ring of finite width w.

Whereas cartilage horseshoes are not necessarily symmetric it seemed to me that the effort of solving the asymmetric problem would not yield sufficient new information to justify the extra cost in time and computational difficulty at this stage. Therefore the problem was solved by assuming that the cartilage is symmetric about the midline as shown in Fig. 3.2.

To accommodate the observation that a cartilage ring hardly ever has a semi-circular shape, an empirical formula for κ_0 of the undeformed cartilage was introduced [54]

$$\kappa_0(\lambda) = C + B\lambda^2 \tag{3.2}$$

The parameters B and C have to be chosen to provide a good match to real tracheal shapes [54].

The boundary conditions for Eq. (3.1) can be elucidated by summing to zero the x and y components of the applied forces and bending moments which are generated when the muscle contracts or an external pressure field is applied. Four boundary conditions are required in order to solve Eq. (3.1). Symmetry provides one of these, namely S , the shear force in the cartilage at the symmetry axis must be zero. The other conditions can be elucidated by applying the conditions of static equilibrium to the deformed cartilage as a whole. Deformation is caused either by the trachealis muscle shortening and generating a force, T_M, or by the application of an external, uniform, pressure field, P (or q, when normalised). This results in Eq. (3.3).

$$\begin{aligned}
&\sum F_x = 0 \quad : \quad T_{Mx} + T(0) + F_x = 0 \\
&\sum F_y = 0 \quad : \quad T_{My} + F_y = 0 \\
&F_x = \int_0^{\lambda_f} (q\lambda)_x = q y_f \\
&F_y = \int_0^{\lambda_f} (q d\lambda)_y = q x_f
\end{aligned} \tag{3.3}$$

where T_{Mx} and the T_{My} are the x and y components of the normalised tensile force generated by the contraction of the muscle, $T(0)$ is the normalised tensile force in the cartilage at the midline ($\lambda = 0$) and F_x and F_y are the normalised forces generated by the external pressure field. x_f and y_f are the final coordinates of the cartilage at $\lambda = \lambda_f$. The boundary conditions for the bending moments are given in Eq. (3.4).

$$
\begin{aligned}
&M_x + M_y + M_q + M_0 = 0 \\
&M_x = T_{Mx} y_f \\
&M_y = T_{My} x_f \\
&M_q = \int_0^{\lambda_f} q\left(\int_0^{\lambda} (d\lambda)_x\right)(d\lambda)_x + \int_0^{\lambda_f} q\left(\int_0^{\lambda} (d\lambda)_y\right)(d\lambda)_y \\
&M_0 = D(0)\left(\kappa(0) - \kappa_0(0)\right)
\end{aligned}
\qquad (3.4)
$$

M_q is the bending moment that is caused by the pressure field.

The deformation of the posterior membrane is modelled as a membrane penetrating into the lumen ($q < 0$) or expanding out of the lumen ($q > 0$). Since it is a membrane in a uniform pressure field, its cross-section must be part of a circle. The entire area (A) of the lumen is the area enclosed by the cartilage (A_C) plus or minus the area (A_M) of the circular segment bounded by the membrane and the straight line joining the cartilage tips.

$$
\begin{aligned}
&A = A_C \pm A_M \\
&A_C = 2\int_0^{y_f} x\,dy
\end{aligned}
\qquad (3.5)
$$

The length of the posterior membrane during the invagination or expansion process was assumed to be inextensible. This is a rather unrealistic assumption since it is known from several studies on various species that posterior membranes are capable of stretching [75, 78]. The stress-strain curve of the posterior membrane is, as an approximation, assumed to be linear. Thus, the tension T_M acting in the posterior membrane when it is subject to any deformation by an external pressure field is given by Eq. (3.6) in which the force normalisation given in Appendix A has been used.

$$T_M \frac{D_C}{R_C^2} = A_M E_M \varepsilon \tag{3.6}$$

where the subscript *C* denotes the cartilage and *M* denotes the muscle properties, and

$$\varepsilon = \frac{E_C I_C}{E_M A_M R_C^2} T_M \tag{3.7}$$

It is convenient to introduce a "stretch coefficient" c_S:

$$\varepsilon = c_S T_M \tag{3.8}$$

with

$$c_S = \frac{E_C \frac{\pi}{4} ab^3}{E_M A_M R_C^2} \tag{3.9}$$

In Eq. (3.9) the cartilage cross-section has been assumed to be elliptical. Thus I_C, the second moment of area of the cartilage is given by $I_C = \pi/4\ ab^3$, $a > b$. a and b are the half radii of the ellipse and A_M is the cross-sectional muscle area. The case of $c_s = 0$ corresponds to an inextensible posterior membrane. For any case $c_S \neq 0$ the parameter L becomes the "resting length" of the posterior membrane, that is when no external pressure field is present and the posterior membrane is in a fully relaxed state.

3.2.2 Analysis of intercartilaginous membrane deformation

An external pressure field causes an elastic stretching of the intercartilaginous tissue that connects the cartilage rings into part of an annular surface. The connective tissue between adjacent cartilage rings was treated as a linearly elastic membrane in simple tension that deformed (in cross-section) as an arc of a circle. With these assumptions it was a matter of straightforward geometry and elasticity theory to calculate (numerically) the stretching and the displacement of the membrane from the undeformed state as shown in Fig. 3.3.

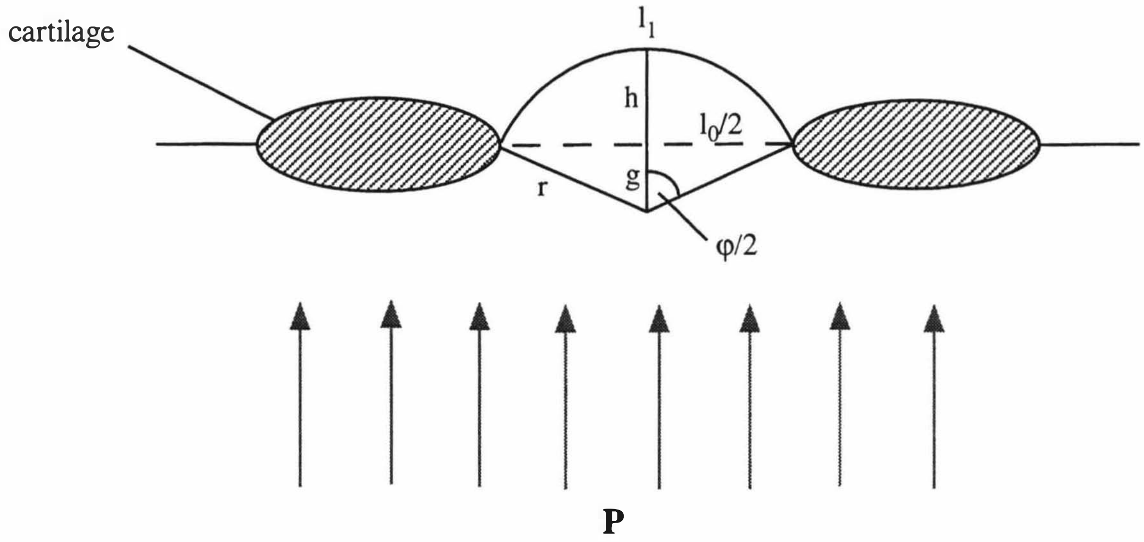

Fig. 3.3. Modelling of deformation of intercartilaginous tissue. Connective tissue is treated as a linearly elastic membrane in simple tension that deforms as an arc of a circle.

The resulting tensile force in the intercartilaginous tissue and the pressure across the tissue wall are related by the Laplace equation which gives

$$\frac{\Pr}{t_W} = E_W \varepsilon = E_W\left(\frac{\varphi r}{l_0} - 1\right) \qquad (3.10)$$

where r, φ, are the radius and the opening angle of the arc, respectively. E_W and t_W are Young modulus and thickness of the tissue wall, respectively. The radius r can be calculated geometrically and is

$$r = \sqrt{\left(\frac{l_0}{2}\right)^2 + g^2} \qquad (3.11)$$

Rearranging Eq. (3.11) and using $r = g + h$ yields Eq. (3.12)

$$r(h) = \frac{1}{2h}\left[\left(\frac{l_0}{2}\right)^2 + h^2\right] \qquad (3.12)$$

The equation that describes the elastic deformation is then Eq. (3.13).

$$\frac{Pl_0}{Et_W} = 2\sin^{-1}\left(\frac{l_0}{2r(h)}\right) - \frac{l_0}{r(h)} \tag{3.13}$$

Eq. (3.13) must be solved to obtain h as a function of P and from this an estimate of the reduction in lumen diameter caused by the stretching of the membrane can be deduced.

3.3 Numerical methods

Eq. (3.1) had to be solved numerically. In order to integrate Eq. (3.1) from $\lambda = 0$ to $\lambda = \lambda_f$ two initial values (κ and κ'') had to be guessed. Once the final coordinates x_f and y_f were known the x and y components of the forces and the bending moments can be calculated from Eqs. (3.3) and (3.4). In an equilibrium state, κ and κ'' have to be chosen such that (i) the sum of all forces is zero, (ii) the sum of all bending moments is zero and (iii) the calculated muscle length L_{comp} agrees with the required muscle length L. After an initial guess for κ and $\kappa''$the correct values were found by using simulated annealing as described in the appendix. The required cost function *(CF)* was specified to be

$$CF = \left|\sum M\right| + \left|L - L_{comp}\right| \tag{3.14}$$

The boundary conditions on the forces, Eq. (3.3), need not be considered explicitly in Eq. (3.14) since Eq. (3.3) is used to evaluate Eq. (3.4), the boundary condition for the bending moments. The choice of CF gives equal weight to satisfying the conditions for static equilibrium and to the requirement that the posterior membrane is extensible. It is not the only possible choice. However, it yielded solutions in which both requirements were met within the allowed fractional error.

The computed length L_{comp} of the posterior membrane can be calculated geometrically.

$$L_{comp} = \gamma R \tag{3.15}$$

where R is the radius of the circular segment of the deformed posterior membrane and γ is the opening angle of the arc.

The force boundary condition was used to evaluate the existing forces and thus does not need to be considered in Eq. (3.14). The problem was considered to be solved when $CF < 10^{-3}$. The algorithm used for the actual numerical integration of Eq. (3.1) was based on that described by Bulirsch and Stoer [82].

Eq. (3.14) had to be modified to allow the computation of the posterior membrane being stretchable. The coordinates of the cartilage ring as well as the components of the forces were computed as already described. Once the tensile force T_M in the posterior membrane is known Eq. (3.15) can be used to compute the strain ε. The new, stretched length $L_S > L$ is

$$\varepsilon = \frac{L_S - L}{L} \Rightarrow L_S = L + LT_M c_S \tag{3.16}$$

The stretched length L_S has to agree with the computed length L_{comp}. This results in the modified cost function (CF_S)

$$CF_S = \left|\sum M\right| + \left|L_S(T_M) - L_{comp}\right| \tag{3.17}$$

This problem was also considered to be solved when $CF_S < 10^{-3}$.

Solutions were obtained for values of q ranging from +1 to the (negative) value at which the posterior membrane first came into contact with the internal wall. At this point the boundary conditions altered and further solutions would have been wrong.

Eq. (3.13) which describes the elastic deformation of the intercartilaginous tissue was numerically solved with a standard rootfinder based on the Van Wijngaarden-Decker-Brent method [82].

3.4 Results

3.4.1 Tracheal mechanics

Fig. 3.4 shows calculated profiles of the initially semi-circular cartilage at several stages of deformation assuming a constant stiffness along the circumference of the cartilage ($f(\lambda) = 1$, Eq. (3.1)). Fig. 3.4A shows the cartilage when the posterior membrane is shortened to 50% of its maximal length (L_1) and $q = 0$, that is without any pressure difference across the walls. Fig. 3.4B shows the effect of an external pressure field alone on tracheal collapse at $L = L_l$ (that is, the posterior membrane has been assumed to be inextensible) at 3 values of q.

In order to investigate the effect of shortening of the posterior membrane on tracheal mechanics, I computed the compliance curves (A/A_0 vs. q) for the initially semicircular cartilage for four constant lengths $L \leq L_l$. These are shown in Fig. 3.5. In Fig. 3.5A the curves are normalised on the area of the base case A_B (which is a semi-circle) and thus give an idea of the relative sizes of the airway lumens and compliances. Fig. 3.5B shows the curves normalised on their own value of A_0 which gives some sense of the relative specific compliances. The compliance curves have been computed from $q = 1.0$ to the value of q at which the posterior membrane touches the inner wall of the cartilage.

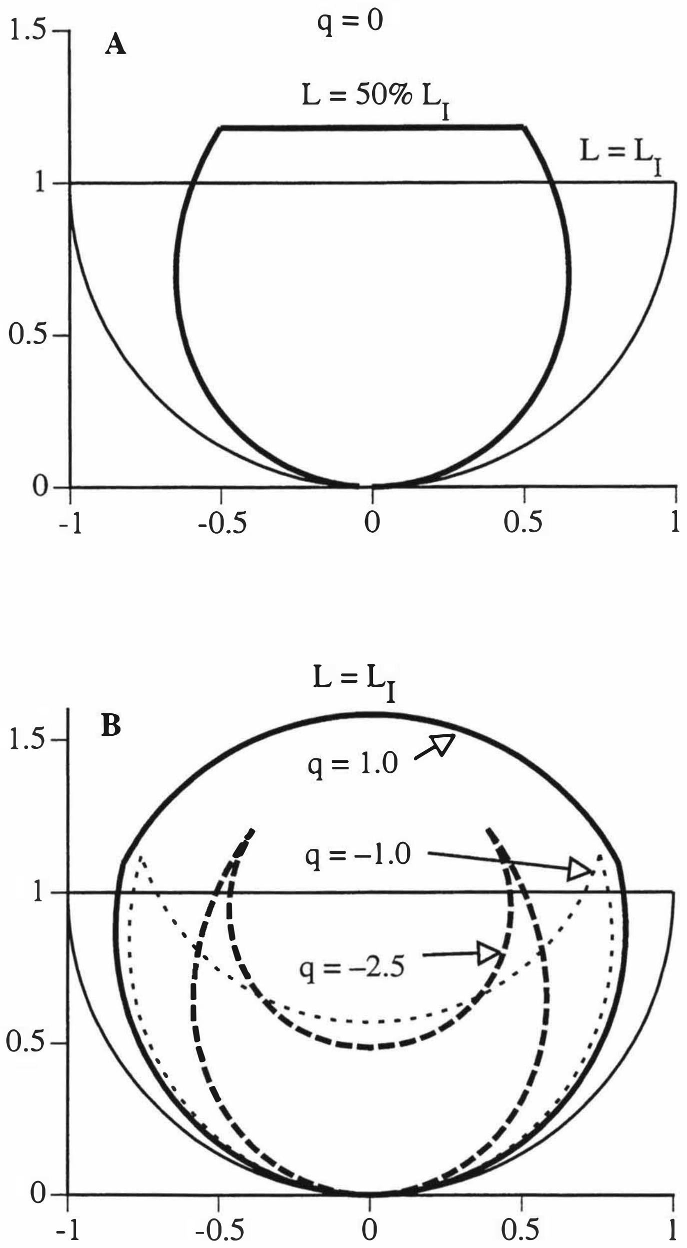

Fig. 3.4. Calculated profiles of the initially semi-circular cartilage at several stages of deformation assuming a constant stiffness along the circumference of the posterior membrane and the posterior membrane being inextensible. A: Posterior membrane is shortened to 50 % of its maximal length (L_I) and $q = 0$. B: Effect of external pressure field alone on tracheal collapse at $L = L_I$ at three values of q.

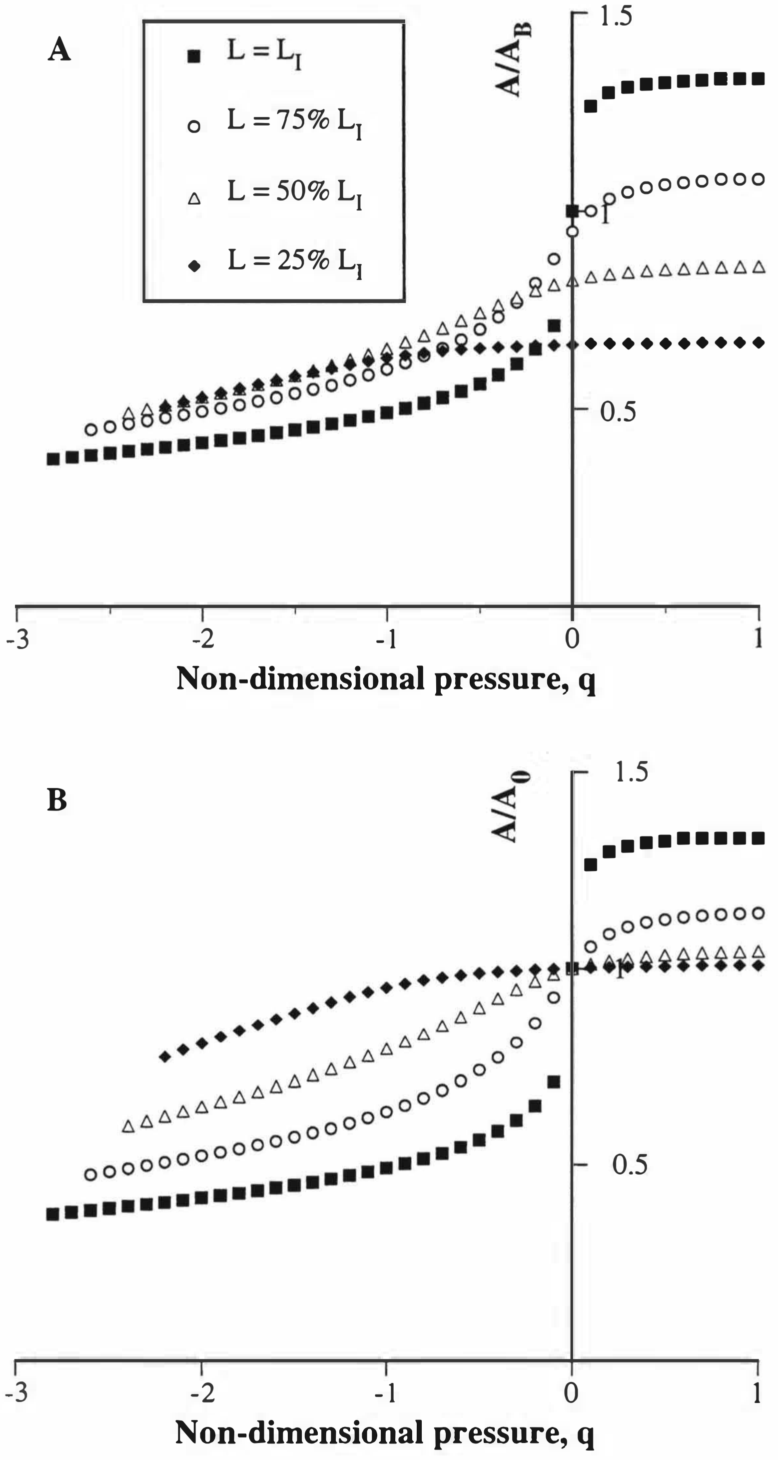

Fig. 3.5. Computed compliance curves at various posterior membrane lengths, *L*. Cartilage ring is assumed to be initially semicircular and of homogeneous stiffness. A: Normalisation on A_B (semicircular base area). B: Normalisation on A_0, value of *A* at $q = 0$ for each case.

Since the length-tension relationship of the trachealis *in situ* is unknown (and is likely to be very varied) under conditions of changing transmural pressure difference and is therefore not easy to model, I investigated, instead, the interrelationship between membrane length, membrane tension, and pressure (as expressed by the parameter q) for the deformation of an initially semicircular cartilage. The non-dimensional tensile force T in the posterior membrane as a function of q at several stages of shortening of the posterior membrane is presented in Fig. 3.6A. These data have been added to and replotted in Fig. 3.6B to show how the tensile force depends on membrane length at constant q. The graphs show that, once the transmural pressure difference is large enough, the required tension in the invaginating posterior membrane decreases as the membrane length decreases.

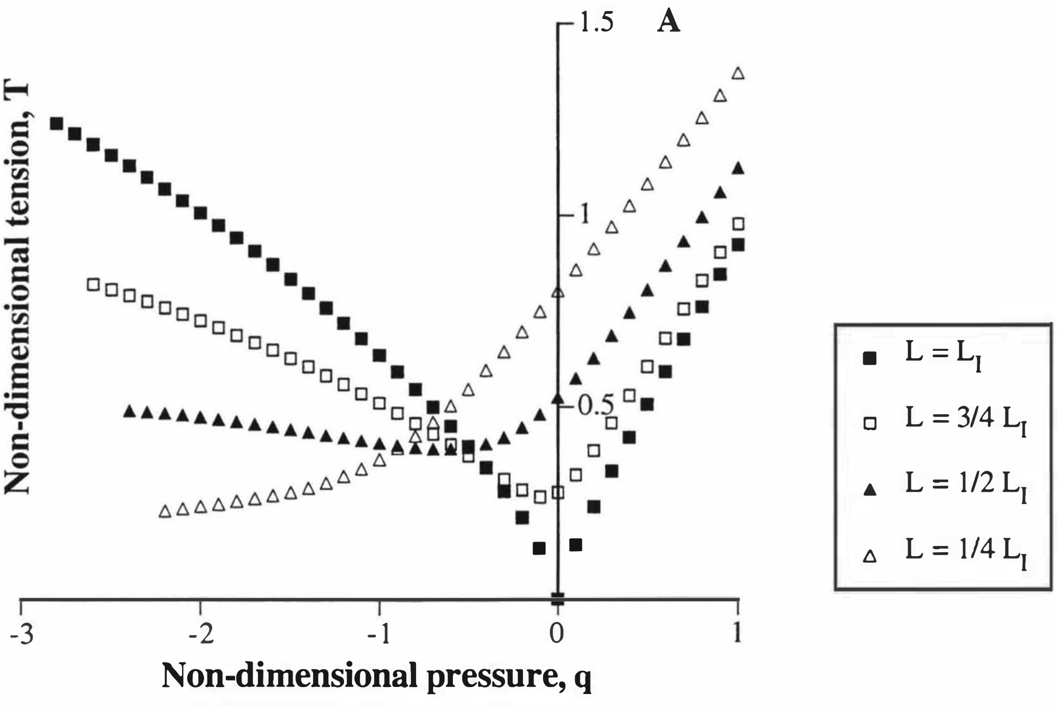

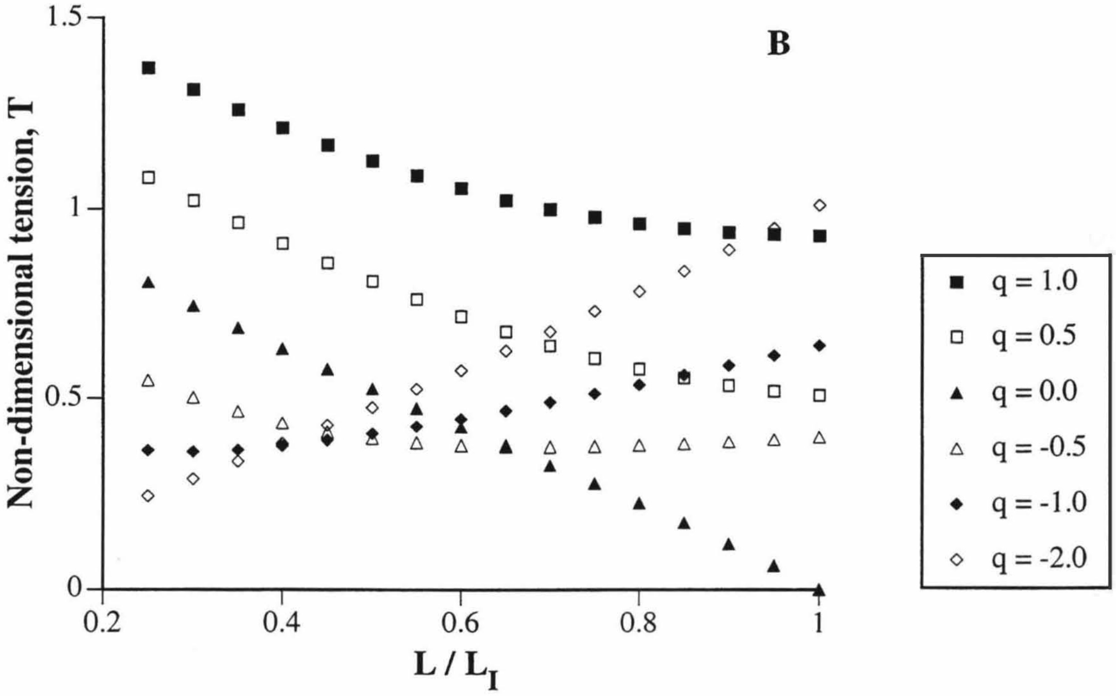

Fig. 3.6. Interrelationship between membrane length, membrane tension and pressure q. A: Non-dimensional tensile force T in the posterior membrane as a function of q at several stages of shortening of posterior membrane. B: Dependence of tensile force T on membrane length L at constant q.

Cartilage is most unlikely to have uniform stiffness around its circumference. To investigate this I studied three cases of smoothly varying non-homogeneous stiffness distributions for the cartilage by choosing the periodic functions for $f(\lambda)$ given by Eqs. (3.17) to (3.19). In these the magnitude of the stiffness is controlled by choosing a value for α between 0 and 1. $\alpha = 0$ corresponds to constant stiffness. Since the radius of the undeformed semicircular cartilage is used as the length scale of the problem, and the problem is solved over half the cartilage length (the cartilage is assumed to be symmetrical, λ takes values between 0 (at the line of symmetry) and $\pi/2$ at the cartilage tip.

$$f(\lambda) = 1 - \alpha \cos^2 \lambda \tag{3.17}$$

$$f(\lambda) = 1 - \alpha \cos^2 2\lambda \tag{3.18}$$

$$f(\lambda) = 1 - \alpha \sin^2 \lambda \tag{3.19}$$

Each function puts the point of maximum weakness in a different location: Eq. (3.17) at the line of symmetry ("centre"), Eq. (3.18) halfway between the line of symmetry and the tip ("mid-arc") and Eq. (3.19) at the tip. Results from these investigations are presented in Fig. 3.7 in which α was kept constant at a value of 0.5 and the unstressed cartilage was semi-circular. It is apparent that having a localised 50% decrease in stiffness anywhere along the circumference makes only a very modest change to the normalised compliance curves.

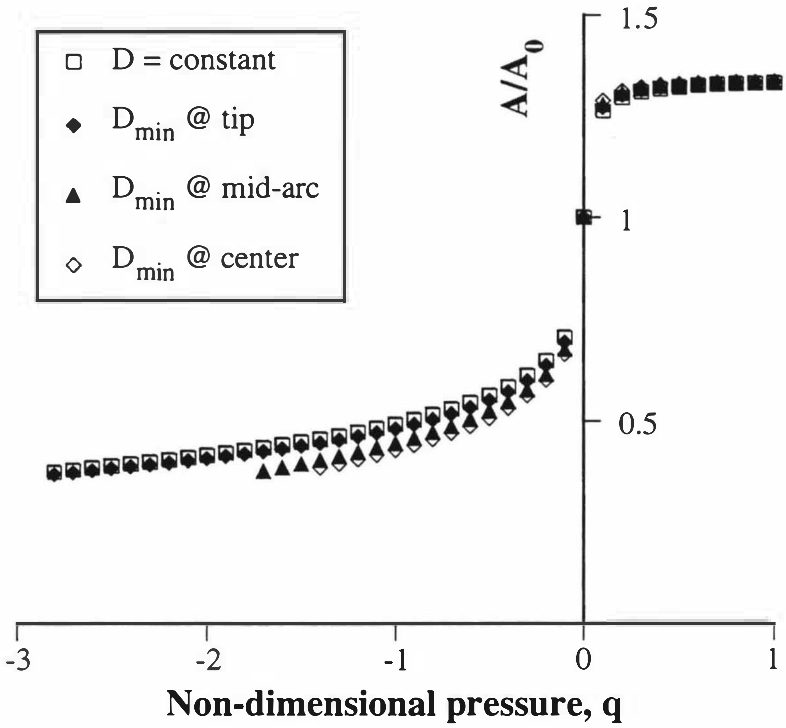

Fig. 3.7. Compliance curves for a cartilage ring having non-uniform stiffness ($\alpha = 0.5$) around its circumference. Undeformed cartilage ring is assumed to be semicircular.

In addition to initially semi-circular cartilage horseshoes, the analysis was extended to other cartilage profiles using Eq. (3.2). I chose profiles where the curvature was constant but greater than that for the initial semicircle, and the cases of semi-circular curvature at the line of symmetry but the curvature increasing (in one case) or decreasing (in the other case) towards the cartilage tips (Fig. 3.8A). Deformation of the profiles shown in Fig. 3.8A were computed with D held constant. A comparison of the compliance curves for $L = L_l$ is presented in Fig. 3.8B. The curves are self-normalised; that is, A_0 is the zero-pressure area in each case. The results in Fig. 3.8 show that unstressed cartilage shape is an important determinant of compliance.

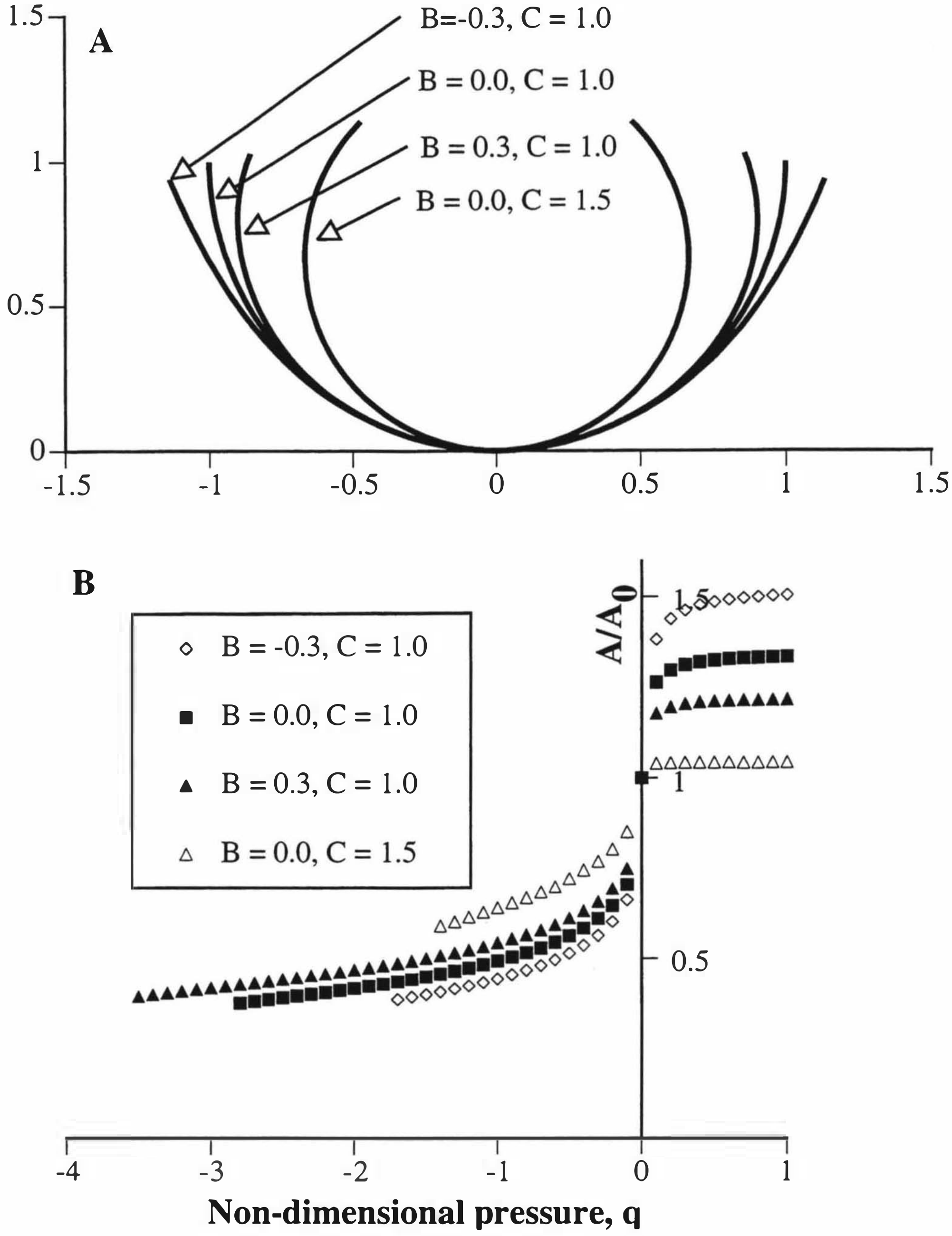

Fig. 3.8. A: Initially non-circular cartilage rings and B: the resulting computed compliance curves. Cartilage rings are assumed to be of homogeneous stiffness. Compliance curves are self-normalised. The parameters A and B are defined according to Eq. (3.2).

Tracheae can be characterised by the tracheal index which is the coronal/sagittal diameter ratio [62, 101]. The ability to alter the cartilage profile enabled me to investigate two well-documented pathological profiles – saber-sheath and lunate tracheae [29, 62]. A saber-sheath trachea is characterised as being narrowed in the coronal plane (tracheal index < 2/3) [101], whereas a lunate trachea is characterised by an index significantly > 1 [62]. The results for these pathological tracheae are given in Fig. 3.9 in which panel A shows both profiles with a relaxed posterior membrane and a membrane shortened to 75 % of its unstressed length. The relaxed semicircular case is included for reference. The compliance curves in panel B illustrate the complex interaction between profile and posterior membrane tension.

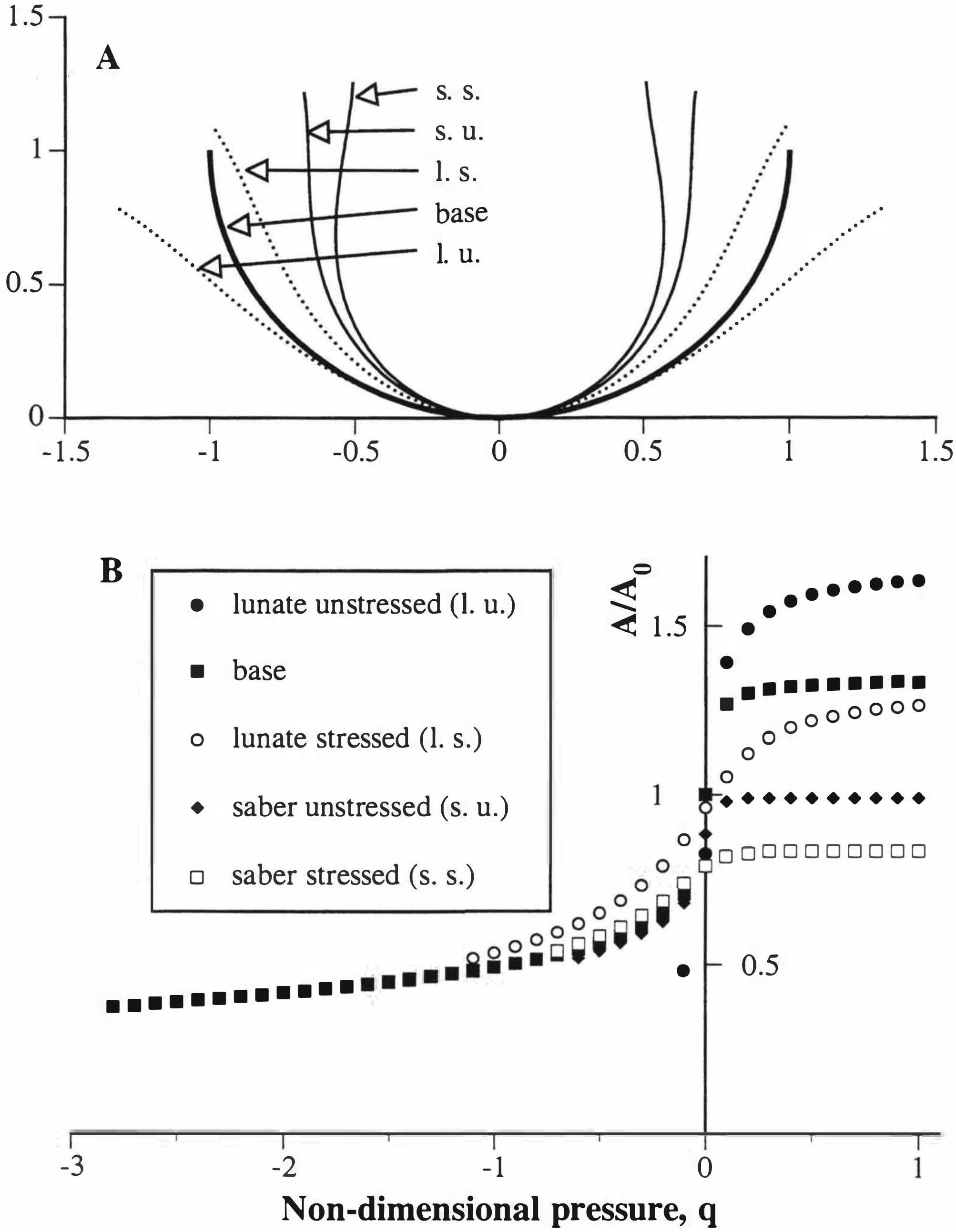

Fig. 3.9. Compliance curves of pathological tracheae in comparison with semicircular base case. A: Initial shape of cartilage rings at $q = 0$. B: Resulting compliance curves.

Fig. 3.10 shows the compliance curves for the case of an extensible posterior membrane in comparison to the membrane being inextensible. In this figure, $L = L_I$ and the cartilage ring is of an initially semicircular shape.

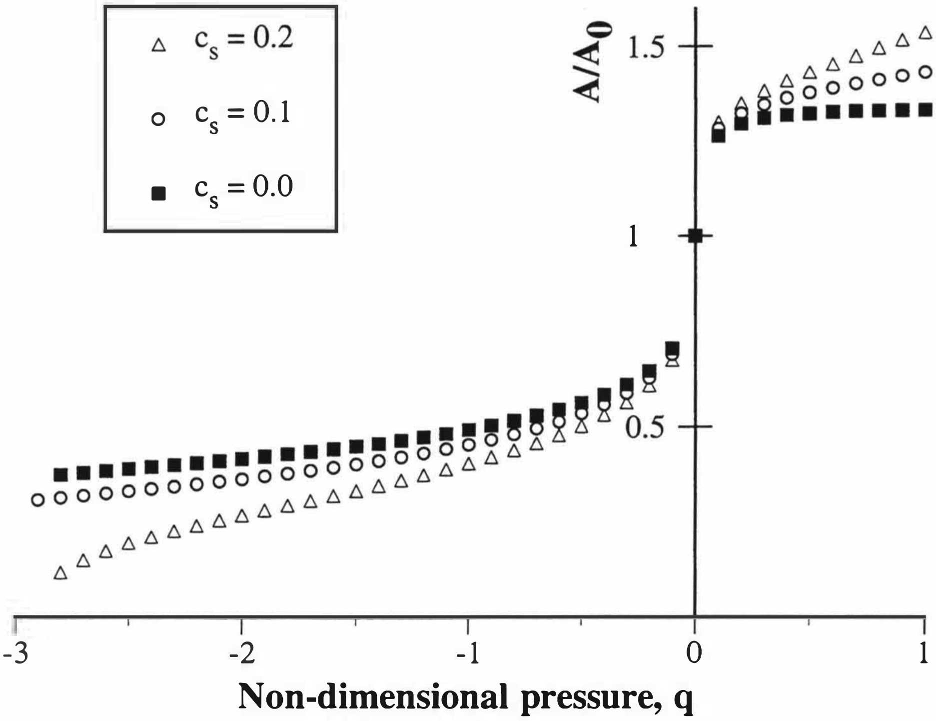

Fig. 3.10. Compliance curve of posterior membrane being extensible. Cartilage ring is assumed to be of homogeneous stiffness and of initially semicircular shape. The stretch coefficient c_s is defined according to Eq. (3.8).

3.4.2 Intercartilaginous tissue computations

Eq. (3.12), which is in a normalised form, was used to evaluate the invagination of the intercartilaginous membrane. However, the normalisation for pressure ($E_M t / l_0$ where E_m is the Young modulus for the membrane) in this equation is different from the normalisation used for the cartilage computations. Rather than have two different normalised pressures I chose to calculate results for the invagination of the intercartilaginous membrane for an "average" human trachea. In order to do this, the normalised pressure, q, has to be dimensioned. The conversion requires the geometric and elastic data for the cartilage. I used the following data taken from Begis et al.: a = 1.8 mm, ($w = 2a$), b = 0.8 mm and R = 10 mm, the average radius of the trachea [8]. I chose 10 MPa as a representative value for E_C based on the work of Rains et al [83]. The conversion is then $P_{tm} = 2100q$ Pa.

The elastic deformation of the intercartilaginous membrane is determined by its Young modulus and its thickness. In the absence of reliable data for these quantities, I used the product Et as an indicator of the stiffness of the connective tissue which is located between two adjacent cartilage rings. In order to obtain invagination information a value for l_0 (Eq. (3.12)) must be chosen. This involves deciding at which point on the cartilage the membrane is attached. It is not clear how to model the attachment of the membrane to the cartilage. Therefore, I chose to use 2 values for l_0: 1.0 mm, which would mean the membrane was attached at the minimum separation of the cartilage horseshoes, and 5.0 mm, which would mean that the membrane was attached near the middle of the luminal surface of the cartilage horseshoes. For the 1.0 mm value, the membrane does not stretch into the lumen even at the smallest value used for Et. The results for the 5.0 mm value are shown in Fig. 3.11. Fig. 3.11A shows the arc height of the stretched membrane as a function of the invaginating pressure and Fig. 3.11B shows the resulting compliance curves with A evaluated at the minimum cross-section of the lumen for five values of Et. The "cartilage alone" curve is the $L = L_t$ curve from Fig. 3.5. The pressure scale for this curve has been adjusted to take account of the extra invaginating force that the membrane exerts on the cartilage in addition to the pressure acting on the cartilage surface.

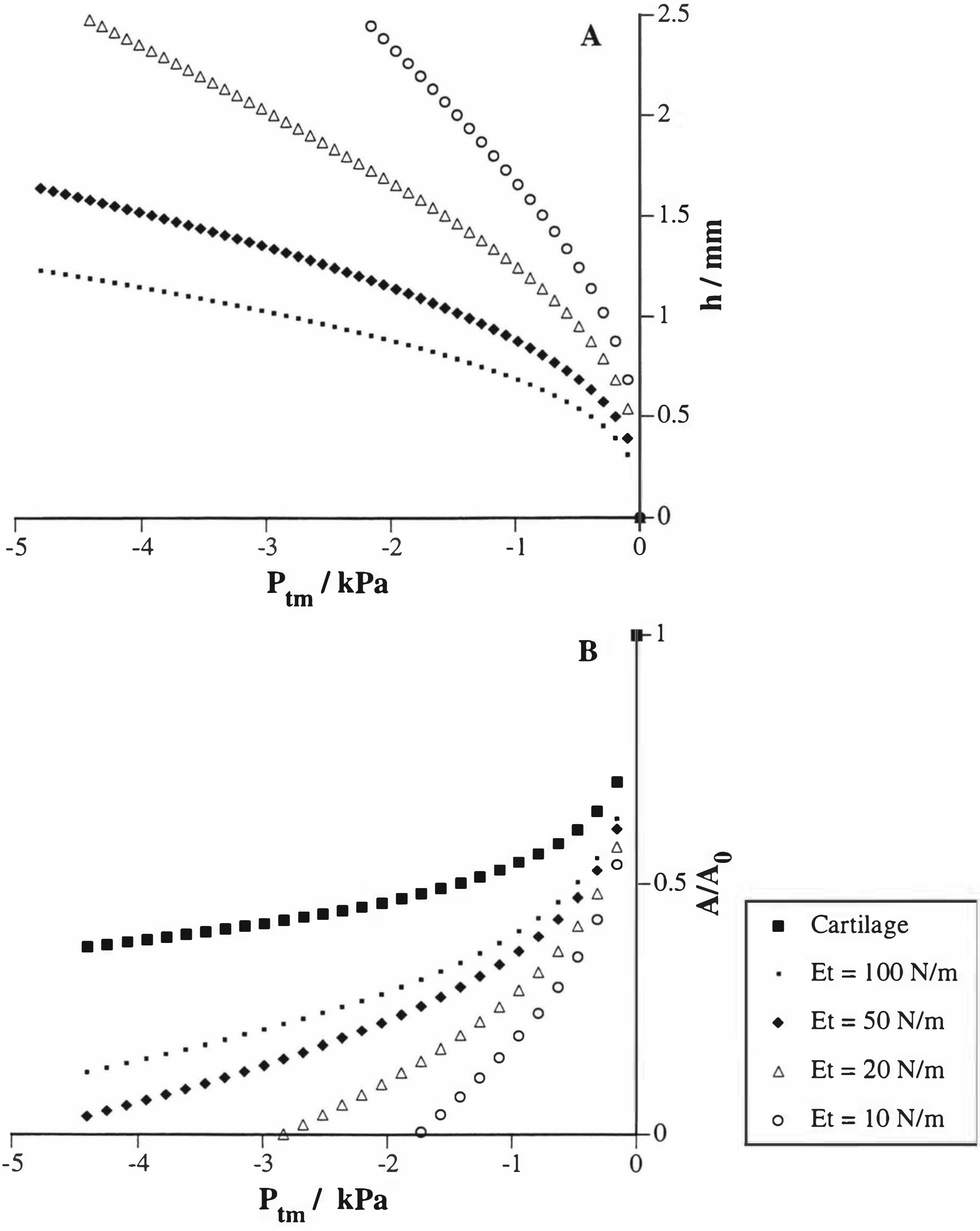

Fig. 3.11. Results of computations for intercartilaginous tissue. A: Arc height *h* as a function of invaginating pressure. B: Resulting compliance curves with *A* evaluated at the minimum cross-section of the lumen for five values of *Et*.

3.5. Discussion

The aim of this chapter was to produce a comprehensive analysis of tracheal mechanics that would provide information about the normal functioning of the trachea as well as some insight into abnormal function. This information is useful in that the resistance of an airway to airflow is determined by its cross-sectional area and how this changes with transmural pressure changes. I have analysed the trachea because its reasonably well defined geometry assists the formulation of a deterministic model. I would expect other cartilaginous airways to be more compliant with the compliance increasing as the quantity of cartilage in the wall decreased. Thus it might be possible to interpolate between the compliance curve of the trachea and those of the membranous bronchioles.

The only other analytical study of tracheal mechanics of which I am aware was that performed by Begis et al [8] who used a finite element approach but were greatly hampered by the lack of a sufficiently powerful computer. They produced only scanty area-pressure results. More powerful computers, a more idealised approach to the problem, and a faster computational procedure have allowed me to perform a much more extensive analysis.

I have used a well-established analytical technique to develop this model for the mechanics of the deformation of the tracheal cartilage under the influence of a uniform transmural pressure difference. The technique is valid for this situation of large displacement but small strain and has been used successfully in the past in studying the mechanics of deformable tubes [22, 46, 53, 60]. The applicability of thin curved beam theory to thick-walled cartilage was analysed by Lambert et al [54]. They concluded that the finite thickness of the specimen ($t/R \approx 0.3$) results in an error of about 3% in calculating the displacement of the cartilage tips and thus does not limit the analysis for the range of deformations investigated. The presented model is idealised in representing the basic unstressed shape of the cartilage as a semicircle. This seems to be a reasonable assumption since intrathoracic tracheae are most commonly round or oval [26]. However, by building in mathematical mechanisms for a variation of stiffness along the arc and for different initial curvatures and changes of curvature around the arc, I believe that I have allowed for the simulation of most real cartilage "rings". Since I made no attempt to model any of the time dependent changes of tracheal area such as those reported by Jones et al [44], this static equilibrium is a long-time limiting case. Although there is evidence that tracheae can collapse asymmetrically [57], no attempt was made to model an asymmetric collapse.

The test of any theory is its ability to predict experimental results. Compliance curves for rabbit tracheal cartilage rings obtained using MRI microscopy were published several years ago [57]. These data were compared with the predictions in Fig. 3.5A in which the following values for the rabbit tracheal cartilage were used: E = 10 MPa, b = 0.25 mm, R = 4 mm which yield P_{tm} = 960q Pa. The value of E is the same as that used in the calculations for human data (Fig. 3.11) for want of rabbit data, whereas the values of b and R were estimated from the MRI images. The comparison is shown in Fig. 3.12.

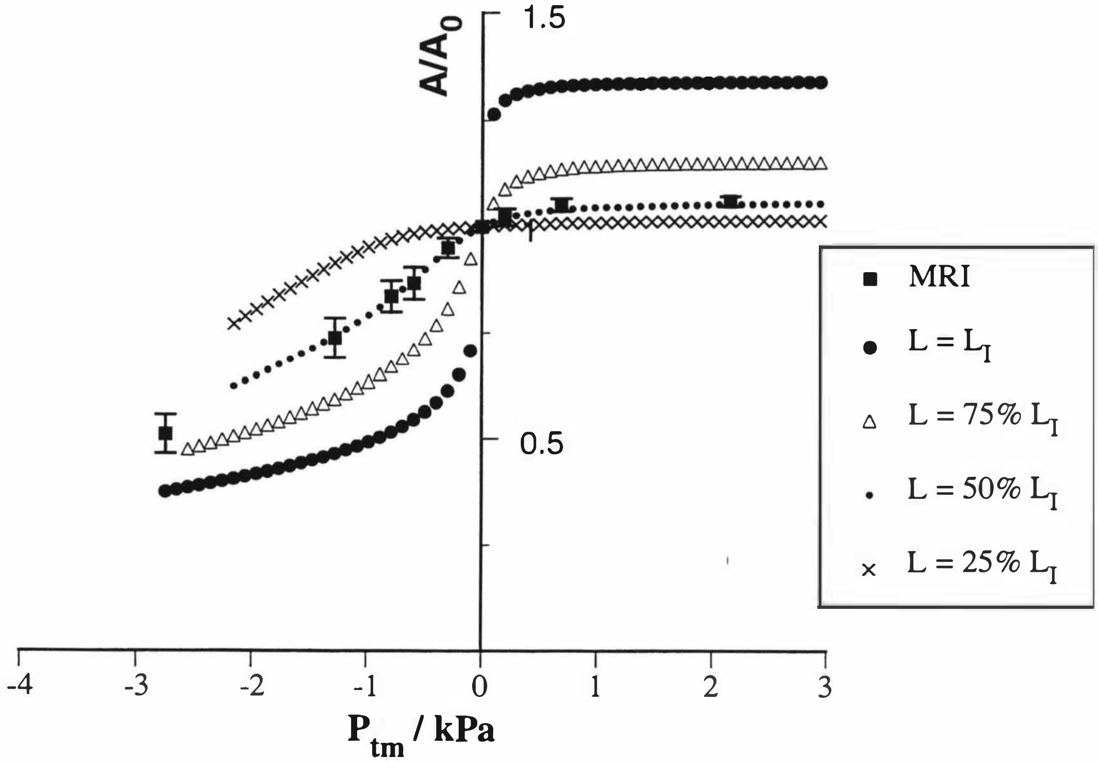

Fig. 3.12. Comparison of results from model computations with compliance curve for rabbit tracheal cartilage rings.

It is apparent that the MRI data closely agree with the theoretically predicted compliance curve for a trachea in which the posterior membrane is shortened to 50% of its tension-free length at zero P_{tm}. That the agreement is with a case that has a pre-stressed posterior membrane agrees with observation in that the mucosal membrane in rabbits is known to be in tension as it is in other mammals [37, 78, 87] as well as humans [18]. However, the agreement is probably fortuitous in that the posterior membrane in the rabbit trachea inserts into the cartilage on the outside and away from the tip and the model is for a membrane inserting into the tip.

The treatment of the posterior membrane as being inextensible is a further simplification. The membrane probably does change length with changes in the pressure field, but the length changes will be dependent on the tone in the smooth muscle and the time course of the pressure change, since the tissue is viscoelastic. Even though the assumption of the posterior membrane being inextensible seems to be reasonable for normal, quit breathing, it is unknown whether this assumption is applicable during forced expiration or violent cough. Linear air velocities during cough are in the range of 280 ms^{-1} [13] which would cause a pressure drop of about 40 kPa. The forces acting during cough could as well cause the posterior membrane to be passively stretched. Alternatively, the event could be too rapid to cause any appreciable changes in the posterior membrane. I have assumed that the membrane inserts into the cartilage tips. This is a reasonable assumption for humans but is not valid for other species.

In order to be able to investigate how a stretchable posterior membrane affects compliance curves, the analysis was extended. The assumption of the membrane being linearly stretchable is only a first order approximation. It is well known that the stress-strain curve of smooth muscle tissue is non-linear [38, 75]. However, for reasonably small strains ($\varepsilon < 0.3$) a linear approximation gives a reasonable idea of how a stretchable membrane changes a compliance curve. It is very likely that tracheal smooth muscle and bronchial smooth muscle tissue have at least a very similar composition. The range of Young modulus E_M of the unactivated smooth muscle tissue can be deducted from reference [38] and is likely to be less then 40 kPa. The actual smooth muscle area A_M is given and is approximately 0.44 mm^2 (8.7 % of tissue area). The resulting stretch coefficient is then $c_s \approx 0.04$ ($E_C = 10$ MPa, $a = 1.8$, $b = 0.8$ mm, $R_C = 10$ mm) thus justifying $c_s = 0.1$ and $c_s = 0.2$ as being in a reasonable range.

The compliance curves are limited by the decision not to attempt to calculate past the pressure at which the posterior membrane contacted the cartilage. It seemed that the pressure range in which the airway is most compliant offered the greatest opportunity for insight into the effect of shape, stiffness, and posterior membrane properties on tracheal compliance and thus on airway function. Once this part of the curve is established the extrapolation to more negative pressures is reasonably apparent in most cases. One case where this is not true is presented in Fig. 3.5. It is the very stiff case of $L = 25\% \, L_l$ for which the point of inflection appears not to have been reached at the most negative value of q. This curve has dubious physiological significance since it is unlikely that the membrane can be shortened to this extent. Exactly how much the membrane can be shortened from the zero-stress state is not known since the zero-stress state in the total membrane probably does not occur physiologically. There is probably tension in the connective tissue structures even when there is no active tension generation in the muscle.

The results shown in Figs. 3.6A and B require some comment. For positive q, T increases with q, as one would expect—the trachea is being blown up like a balloon. For negative q, it is not quite so obvious what will happen. If the pressure difference were applied to the cartilage alone, the membrane would go slack. However, the membrane must also support the pressure difference and meet the boundary conditions even as its radius of curvature changes. Thus there must be tension in the membrane but, as Fig. 3.6A shows, the tension depends not only on the pressure but also on the initial state of tension in the membrane. For the very shortest case ($L = 25\% L_l$), the tension steadily reduces as the pressure difference is increased whereas the longer membranes all require greater tension. The case of constant tension appears to be between 25% and 50% L_l.

I chose to normalise the area results on the area at zero P. This has the great advantage over all other normalisations that it does not change when the pressure axis is re-scaled. However, it makes comparison with experiments more difficult because most experimental results are normalised on the maximal area of the airway (usually taken as the area at $P = 2.5$, or 3.0 kPa) [57] for the good reason that this is the most reliable experimental measurement and it keeps the areas on a scale of 0 to 1. Often the area appears to have reached a plateau at this pressure. The presented model shows that this may indeed be the case provided that the posterior membrane is essentially inextensible.

Even small differences in the undeformed shapes can result in a considerably different compliance curve (Fig. 3.8). The ability to alter the cartilage profile enabled me to investigate two well-documented pathological profiles—saber-sheath trachea and lunate trachea [29, 62]. The unstressed lunate trachea is life-threateningly compliant near zero P_{tm}. However, some tension in the posterior membrane stiffens it remarkably. This can be observed quite commonly in cases of infant tracheomalacia [96]. The effect of posterior membrane tension on the saber-sheath trachea is almost entirely restricted to positive values of P_{tm}. This shape is very stiff.

It is highly likely that the cartilage is inhomogeneous in both its elastic and geometric properties. Whereas there is some experimental evidence for this, the experiments did not quantify the inhomogeneity [16, 86]. The attempts to simulate inhomogeneity (Fig. 3.7) by making the stiffness of the cartilage change around the arc produced relatively minor changes in the compliance from the base case. It appears that the state of tension of the posterior membrane (Fig. 3.5) and the shape of the horseshoe (Fig. 3.8) are more important determinants of tracheal stiffness.

The introduction of dimensioned pressure in Fig. 3.11 for the intercartilaginous membrane requires appropriate choices of mechanical and geometric parameters. I used geometric data based on that given by Begis et al since they measured a human tracheal cartilage horseshoe. The choice of 10 MPa for E appears to be of the right order based on the work of Rains and others [83]. Thus I am reasonably confident about this dimensioning. However, the appropriate values to be used for the intercartilaginous membrane and the posterior membrane are more difficult to assess. If one considers that the significant elasticity of the intercartilaginous membrane resides in the epithelial basement membrane, then the data of Welling et al [104] suggests that E is of the order of 1 MPa and t is of the order of 10μm yielding a value for Et of 10 N/m. On the other hand if one uses an average value obtained from the whole mucosa such as that obtained by Codd et al (E = 20 kPa) and assume a thickness-to-radius ratio of 0.01, then Et is approximately 20 N/m [12]. For the case shown in Fig. 3.10B of an initially semicircular cartilage with no tension in the posterior membrane, it appears that either of these two conditions would cause the airway to close at pressures where the trachea is know to be open. There are at least two possible explanations of this discrepancy. The first possibility is that I have simply chosen poor values for E and t. The second is that the model is unrealistic. I believe that the weakness lies in the model for the invaginating membrane which is treated as a very thin membrane subject only to the Laplace relationship and attached close to the centre of the internal surface of the cartilage. Both assumptions are likely to be invalid. It is not clear how the membrane should be modelled. The choice of attachment point provides an upper limit to the possible invagination. If a point closer to the "edge" of the cartilage had been chosen, l_0 would have been smaller thus resulting in a smaller value for h. Furthermore, the baseline from which h is measured would have been more distant from the longitudinal axis of the trachea. Both of these factors serve to reduce the invagination. Indeed when I attached the membrane at the points of closest separation of the (elliptically cross-sectioned) cartilage horseshoes, the membrane did not invaginate into the lumen defined by the cartilage. Thus I regard the results in Fig. 3.11B as representing an upper limit to the possible invagination of the intercartilaginous membrane. Comparison of intercartilaginous membrane invagination with MRI data additionally confirm that the model is poor (Fig. 3.12) [57].

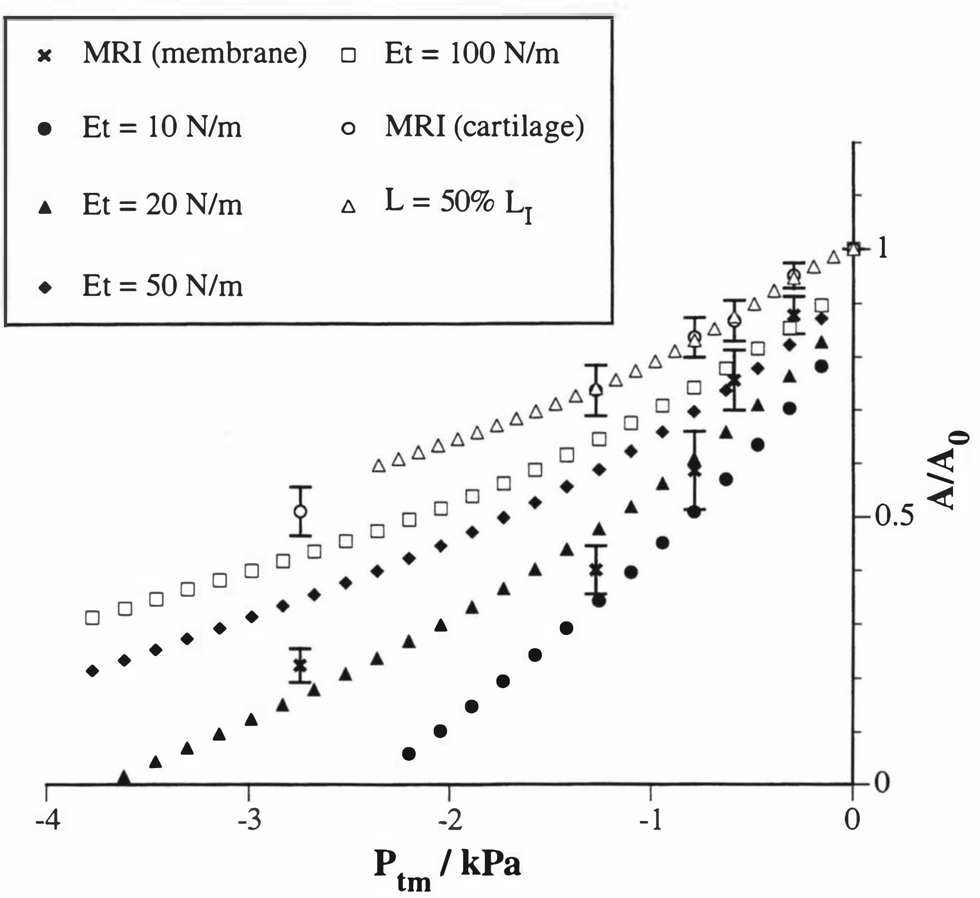

Fig. 3.12. Comparison with intercartilaginous membrane invagination with MRI rabbit data.

It is likely that the tissue must be modelled as a shell and not as a simple membrane. This would provide a further application of the theory on which this thesis is based. However, no attempts have been made to address this analysis

PART II:

Forced expiratory flow in the presence of muscle tone

1. Introduction and literature review

Both the lungs and the surrounding chest wall are elastic structures, that is they have a tendency to return to their base configuration when a distending force is removed. Consequently, the development of techniques which allow the characterisation of the elastic properties of these structures are of considerable importance in assessing the functionality of the lungs and any possible abnormality found in disease. One approach to the characterisation of the mechanical performance of the lungs would be to measure the elastic properties of the chest wall and the lungs. Clinically, this approach is difficult in the conscious subject. The more pragmatic approach is to assess the distensibility of the lungs by making measurements of lung volume and airway calibre by undertaking tests of maximum flow during a forced expiration. Such tests are well documented [6, 28, 88, 97, 105, 107].

Before discussing forced expiratory techniques it is convenient to introduce some of the terminology defining the relevant volume subdivisions of the lungs. At the end of a maximal inspiration, the lung is fully inflated to its total lung capacity (TLC). The vital capacity (VC) is the maximum volume of gas which can be expelled from the lungs following a maximal inspiration. The residual volume (RV) is the volume of gas that remains in the lungs at the end of a maximal expiration. RV can be determined by simply subtracting VC from TLC. Also of interest in the following discussion is the functional residual capacity (FRC) which is the volume of gas remaining in the lungs at resting expiratory level (normal tidal breathing) [28].

A convenient starting point for discussing the complexities of the deceptively simple forced expiratory manoeuvre is the relationship between driving pressure and flow—the so-called isovolume pressure-flow (IVPF) relationship which was first analysed by Fry and Hyatt [24, 25]. The subject performs a series of expiratory manoeuvres from total lung capacity (TLC) with varying degrees of effort and the relationship between expiratory flow and alveolar pressure is examined at a constant lung volume. The techniques used to measure those quantities are well established and can for example be reviewed in reference [28]. With increasing effort and, thus, increasing alveolar pressure (relative to atmosphere), the flow increases, but the increments of flow decline progressively until a plateau value for flow is reached. Above a certain pressure, a greater effort does not produce greater flow thus leading to the concept of flow limitation. A (computed) IVPF curve is shown in Fig. 1.1. Each expiratory effort produces one point on the curve. Examples of experimentally measured IVPF curves are depicted in [36, 66] for example.

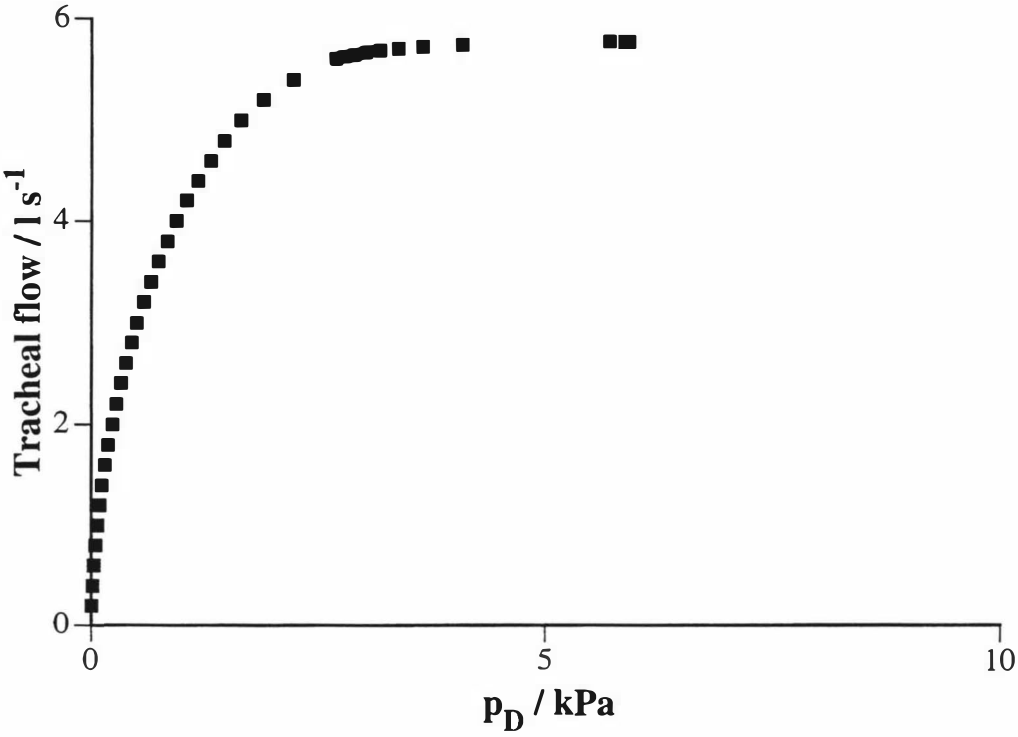

Fig. 1.1. Computed Isovolume-Pressure-Flow curve at 80% VC.

The IVPF curve, although of great theoretical interest, is not clinically useful because of the difficulty of measuring it and patient discomfort. The more common method is the maximal expiratory flow volume (MEFV) manoeuvre. The subject has to perform a single forced expiratory manoeuvre over the entire VC where the maximum flow at each volume is recorded against the expired gas volume. Fig. 1.2 shows a MEFV curve of a normal subject. With a forced expiration starting from TLC, flow rises rapidly to its peak value (at about 80 %VC) and then progressively declines.

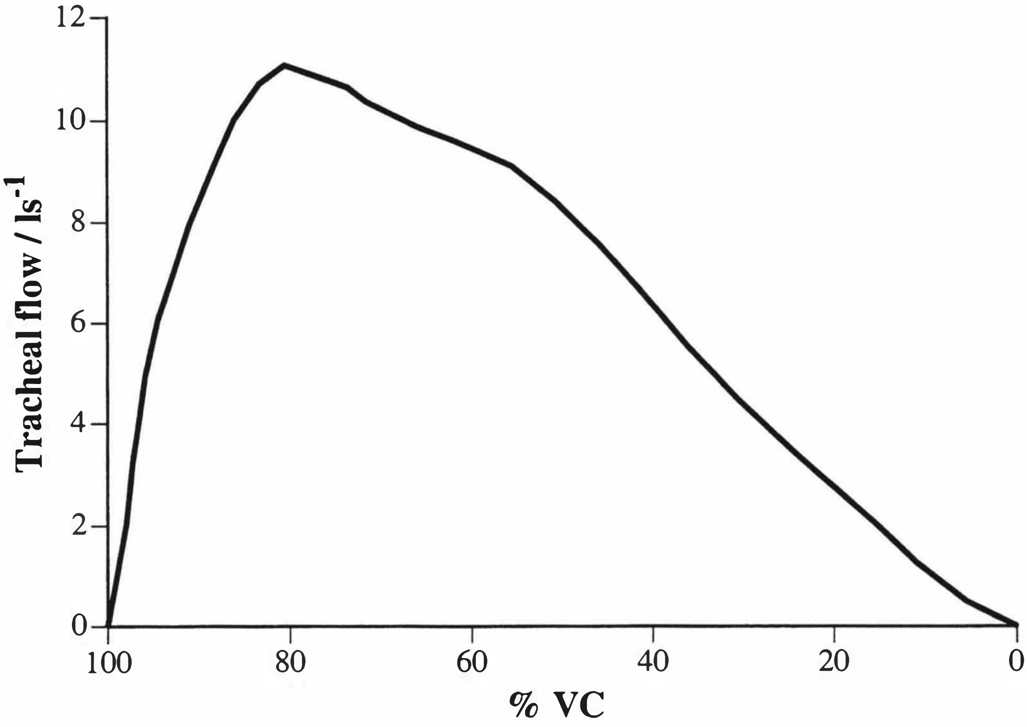

Fig. 1.2. Maximal expiratory flow volume curve (MEFV) obtained from a normal subject (reproduced from [6]). % VC refers to the fraction of VC remaining to be expired.

It is well established that after reaching maximal flow at about 80% VC flow becomes effort independent. Thus some property of the lungs determines maximal expiratory flow [6, 28, 97]. It was Fry in his seminal paper who first showed that the limitation of expiratory flow observed in the MEFV manoeuvre depends closely on the compliance characteristics of the airways [24]. Fry showed that if one recorded IVPF curves over a wide range of lung inflations one could use the plateau values to construct the MEFV curve. Each plateau value is one point on the effort-independent part of the MEFV curve. Consequently during the last forty years researchers have proposed various mathematical models in order to study the interrelationship between airway compliance and expiratory flow. Fry showed that flow could in principle be predicted by integrating the coupled equations representing the flow and airway mechanics from the periphery to the mouth [24, 25]. However, a lack of information about flow and airway properties restricted his results to a discussion of possible flow behaviour. The direct integration of the basic equations was applied with some degree of success by others [51, 81]. In 1977 Dawson and Elliott published a significant contribution to the understanding of expiratory flow limitation by introducing the concept of flow limitation at wave speed

[17]. They pointed out that elastic tubes could not carry a fluid at a mean speed greater than the speed at which deformations will propagate along the tube. The speed at which deformations will travel in a given fluid is the wave speed which is determined by the specific compliance of the tube wall and the density of the gas [17]. The location along the tube at which, with increasing flow, the local wave speed equals the airflow is called the choke point [17].

Lambert et al. published the first computational model for expiratory flow from human lungs that successfully predicted flows very close to those measured in excised human lungs [61]. Lambert's model will be reviewed in detail in the following chapter. Although his model reproduces many features of forced expiration it cannot be used to examine flows downstream from the choke point. Elad et al published an analysis in which they presented a mathematical model of forced expiration including solutions downstream of the choke point [21]. A more general analysis of flow limitation in collapsible tubes was published by Shapiro [91]. A brief review focusing on the then current understanding of expiratory flow limitation was written in 1983 by Hyatt [33].

The forced expiratory volume expired within the first second (FEV_1) is a commonly used measure of lung function based on the MEFV manoeuvre. This method effectively integrates the maximum flow over a large part of the vital capacity. The expired volume within the first second is greater then 70 % of the vital capacity of a normal subject [28]. Reductions in FEV_1 are associated with either acute or chronic airway disease, such as asthma, chronic bronchitis, and emphysema [28, 33].

An alternative method to assess the functionality of the lungs is to determine the resistance to airflow (Raw) in the airways [13, 28]. In general, the calculation of Raw requires the simultaneous measurement of the difference in pressure at the two ends of the system of tubes and the flow through the system. Resistance, similarly to Ohm's law for electrical resistance, can then be calculated as pressure difference divided by flow. The quantification of Raw in airways requires the pressure difference between mouth and alveoli and the flow rate. The latter can readily be determined at the mouth [13, 28]. The more difficult measurement is that of the alveolar pressure but various techniques have been developed to overcome this problem [28]. Normal values for Raw measured at FRC are about 0.005-0.15 kPa $l^{-1}s$ [13]. When Raw is above normal values, physicians usually believe that airways are somewhat obstructed. Resistance is partly dependent on the tone of the bronchial smooth muscle, which is controlled by the parasympathetic nervous system. The bronchial smooth muscle system can be challenged pharmacologically [19, 28, 31, 71, 106]. This can lead to narrowing of airways to a point at which further challenge is deemed to be unsafe. Consequently, the effect of tone in the smooth muscle system exerts an important influence on airway resistance. Several experimental studies have been undertaken concerning airway narrowing and the related increases in resistance to flow [11, 19, 27, 31, 71, 106]. However, theoretical studies to date are only very few in number. One of the first papers concerned with a more theoretical analysis of the mechanics of airway narrowing was published in 1986 by Moreno et al [73]. They concentrated on the geometrical effects of changes in airway wall structure. Based on this work, Wiggs et al published a computational model that simulated airway narrowing induced by a hypothetical muscle stimulant [109]. This model provides useful insights into the effects of changes in airway morphology on airway resistance but did not take into account airway mechanics during bronchoconstriction. In 1993 Lambert et al extended Wiggs' model by incorporating airway smooth muscle length-tension relationships, limit to muscle stress and interaction with the parenchyma [59]. This model was used to investigate the mechanically most important airway wall changes. The authors concluded that, in disease, the most compromising factor is the airway smooth muscle mass. A more detailed review of this model is given in chapter 2.2.

Airway smooth muscle tone is, at least in non-cartilaginous airways, the governing mechanism, that determines the Raw characteristics. Although much work is being done to understand airway smooth muscle [9, 23, 37, 38, 63, 67, 78, 80, 92, 93] the factors that control and limit smooth muscle shortening as well as the consequences of structural and functional changes are still not fully understood [90, 94]. Structural changes in the airway smooth muscle as they for example occur with asthmatic subjects might result in different mechanical properties [90]. Consequently, within the last ten years, various studies were conducted on airway smooth muscle tissue of various species aiming to elucidate its mechanical properties and its ability to contract. Ishida et al. conducted an *in vitro* study investigating the elastic loading of porcine trachealis muscle [37]. They concluded that elastic loading significantly alters the mechanical properties of airway smooth muscle *in vitro*, effects which are likely to be relevant *in* *vivo*. In 1992 Okazawa et al conducted *in vivo* as well as *in vitro* studies on dog trachealis muscle [78]. They observed that muscle shortening *in vivo* is decreased in comparison with *in vitro* and concluded that this is primarily due to the elastic afterload provided by the cartilage. In the same year, Ishida et al. published *in vitro* data obtained from human bronchial smooth muscle [38] and demonstrated that mechanical properties of human main stem bronchi differ dramatically compared with those of porcine data [37]. Thus there appears to be major species-dependent differences in smooth muscle behaviour, and hence using data obtained from one species in analysing airway behaviour in another (as has been done by Lambert [58, 59]) could give rise to misleading results.

In this part of the thesis I am going to address some of the weaknesses in Lambert's two models [59, 61] by combining them. A weakness of Lambert's computational model for forced expiratory flow [61] is the fact that the compliances of the individual airways are given by a set of mathematical functions that do not take into account the structure of the airway walls. Thus this model cannot be used to simulate the effects of wall remodelling on the MEFV curve. In contrast to this, Lambert's model of resistance to airflow when subject to smooth muscle constriction is based on a system of tubes which do not deform as a result of transmural pressure differences across the airway walls during flow. A combination of both models would therefore allow the computation of forced expiratory flow and resistance to flow, with dynamically compliant airways when subject to bronchoconstricting agents. This section of the thesis is concerned with merging both models. Lambert's resistance model (RM) was used to generate a new "dosed" set of mathematical functions that were used to compute "dosed" MEFV curves. The resulting MEFV curves were used to compute FEV_1 volumes as a function of a "mathematical dose" of a hypothetical bronchoconstricting agent. Raw at a fixed volume flow against dose at various VC's, was also computed during the calculation of the MEFV curve. Morphometric data, obtained from normal subjects as well as from patients suffering from chronic obstructive pulmonary disease (COPD) and asthma, provided information on airway wall structure [10, 40, 47].

In the following chapter the expiratory airflow model and the resistance to airflow model as well as the new, combined model will be reviewed. The computational procedures are discussed in chapter three and results of the computations are presented in chapter four followed by a discussion in chapter five.

Finally, a remark regarding nomenclature has to be made. In the previous chapters, P has been used to denote pressure — the convention in respiratory mechanics. However, for the work about to be presented, this nomenclature becomes ambiguous because P is also conventionally used for a geometrical measure — the perimeter of a cross-section. Therefore, in the remainder of this thesis, pressure will be denoted p.

2. Review of the model

2.1 Review of expiratory airflow computations

The anatomic basis of the computational model [61] is the idealised airway branching geometry proposed by Weibel [103]. The bronchial tree is assumed to form a symmetrically bifurcating tree, subdivided into generations z, which range from $z = 0$ (trachea) to 16 at the periphery (bronchioles). Thus, the total number N of airways within one generation is $N(z) = 2^z$. The local average flow speed U in generation z is given by the total volume flow $\dot{V}$ divided by the total cross-sectional area A of one generation. All pressures are referenced to the pressure on the outside surface of the lung, the pleural pressure. Since the lung is elastic, the pressure in the alveoli will be greater than pleural pressure by an amount that depends on the state of lung inflation. This pressure is called the static recoil pressure of the lung and is denoted p_L. Alveolar gas pressure is assumed to be uniform and equal to static recoil pressure p_L at each volume. Following the suggestion of Mead et al [65] which later received empirical support [49], peribronchial pressure is assumed to be equal to pleural pressure and transmural pressure is therefore equal to pressure in the airways p. Also, when flow approaches flow limitation, pressure losses are considerably higher than any losses due to acceleration effects which therefore can be ignored. The pressure at any point in the airway is given by

$$p = p_A - \tfrac{1}{2}\rho U^2 - \int_0^x f dx \qquad (2.1)$$

where p_A is alveolar pressure, ρ is the fluid density, f is the dissipative pressure loss per unit distance and x is the distance along the airway axis from the alveolus. Assuming the volume flow $\dot{V}$ is held constant, the pressure gradient can be obtained by differentiating and rearranging Eq. (2.1).

$$\frac{dp}{dx} = \frac{f}{1 - \left(\frac{U}{c}\right)^2} \qquad (2.2)$$

The wave speed, c, which was introduced by Dawson and Elliot [17], is given by

$$c^2 = A(p) \Big/ \rho \frac{dA(p)}{dp} \tag{2.3}$$

where $A(p)$ denotes the tube law of the tube. From Eq. (2.2) it can be seen that the pressure gradient dp/dx becomes infinite when the local flow speed U equals the wave speed c. The flow for which $U^2/c^2 = 1$ is the critical flow [17]. Generally, flow behaviour in collapsible tubes can undergo transitions from sub-critical flow ($U^2/c^2 < 1$) to supercritical flow ($U^2/c^2 > 1$) [91]. The computational model was not designed to study flow downstream of the choke point.

The dissipative pressure loss/unit length f is described by the following empirical relationship taken from a human cast study [84]

$$f = \frac{8\pi\mu\dot{V}}{A^2(p)}(1.5 + 0.0035\,Re) \tag{2.4}$$

where μ is the viscosity of the fluid and Re is the local Reynolds number: $2\rho\dot{V}/\mu\sqrt{\pi A}$. The coefficient $8\pi\mu\dot{V}/A^2$ is the pressure loss per unit length in Poiseuille flow.

The pressure in an airway is computed by starting at the periphery (generation 16) and integrating Eq. (2.2) along the length L of each airway. The transition from one generation to the next is assumed to take place over such a short distance that dissipative pressure losses fdx can be neglected and only convective changes have to be considered. Eq. (2.1) can then be used to obtain the following relationship (Eq. 2.5) between the pressure p_{n+1} at the downstream end of the $(n+1)$th generation and the pressure p_n at the upstream end of the nth generation. If the area at the convergence of two airways increases in the direction of flow, that is $A_n(0) > A_{n+1}(L)$, it is assumed that there is no pressure recovery. In this case $p_{n+1}(L) - p_n(0)$ is set to zero.

$$
\begin{aligned}
&p_{n+1}(L)-p_n(0)=\tfrac{1}{2}\rho\dot{V}^2\left[\left(\frac{1}{A_n(0)}\right)^2-\left(\frac{1}{A_{n+1}(L)}\right)^2\right], && A_n(0)<A_{n+1}(L)\\
&p_{n+1}(L)-p_n(0)=0, && A_n(0)\geq A_{n+1}(L)
\end{aligned}
\tag{2.5}
$$

The airway mechanics are described by the value of maximal airway area A_{max} and the curves of normalised airway area, $\alpha = A/A_{max}$. The normalised curves are represented by two rectangular hyperbolae, matched for intercept and slope at zero pressure.

$$
\begin{aligned}
&\alpha(p)=\alpha_0\left(1-\frac{p}{p_1}\right)^{-n_1}, \; p\leq 0\\
&\alpha(p)=1-(1-\alpha_0)\left(1-\frac{p}{p_2}\right)^{-n_2}, \; p>0
\end{aligned}
\tag{2.6}
$$

with

$$
\begin{aligned}
p_1&=\frac{\alpha_0 n_1}{\alpha_0'}\\
p_2&=-\frac{n_2(1-\alpha_0)}{\alpha_0'}
\end{aligned}
\tag{2.7}
$$

α_0 is the value of α at $p = 0$. α_0' is the value of $d\alpha/dp$ at $p = 0$.

The curvature changes sign and is therefore discontinuous at $p = 0$. The parameters A_{max}, α_0, α_0', n_1, n_2 have to be chosen for each z in order to specify the mechanical behaviour of the bronchial tree. Fig. 2.1 depicts the airways' properties.

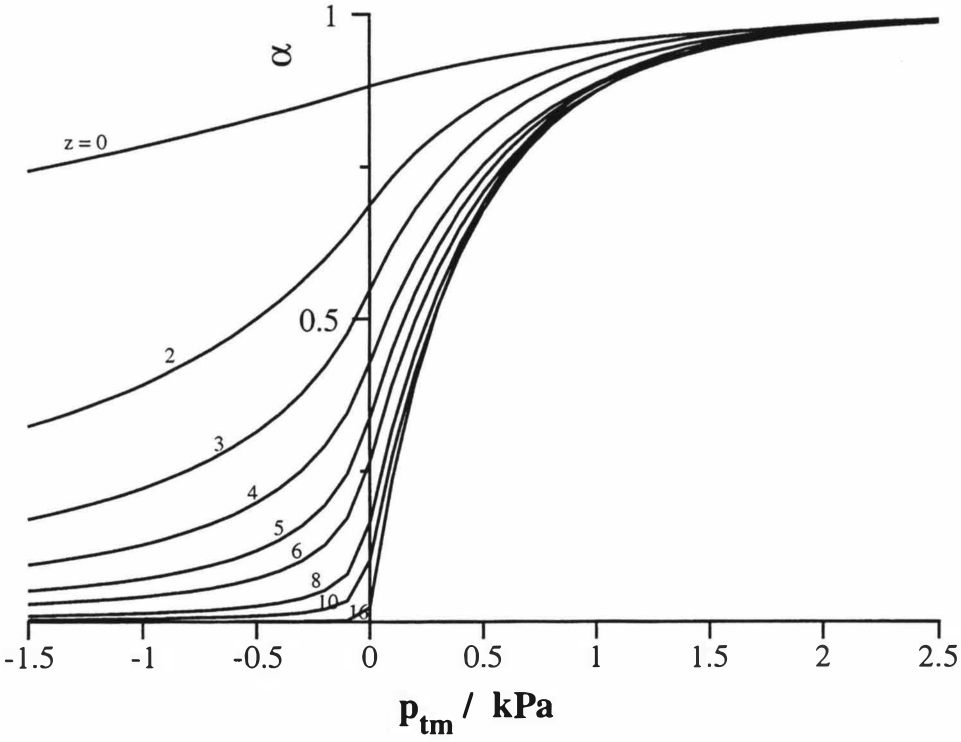

Fig. 2.1. Normalised airway cross-sectional area (α) plotted against transmural pressure for selected generations *z*.

Literature data on airway morphometry and mechanics does not provide enough information to describe all of the parameters of the model airways. The choice of the parameters was primarily guided by data provided by Hyatt et al for central airways [35] and Weibel's data for the more peripheral airways [103]. The unknown values were obtained by trial and error extrapolation and interpolation. The complete set of parameters used is given in the appendix. The length *L*, of each generation *z* of airways at 75 % of total lung capacity was computed from Weibel's values. Lengths at other lung volumes were then computed by scaling the length with the cube root of the actual lung volume.

The average pressure-volume curve of five lungs, reported by Hyatt et al. [35] was used to relate inflation pressure p_L to lung volume *V*. Fig. 2.2 shows the $V(p_L)$ relationship used in the model.

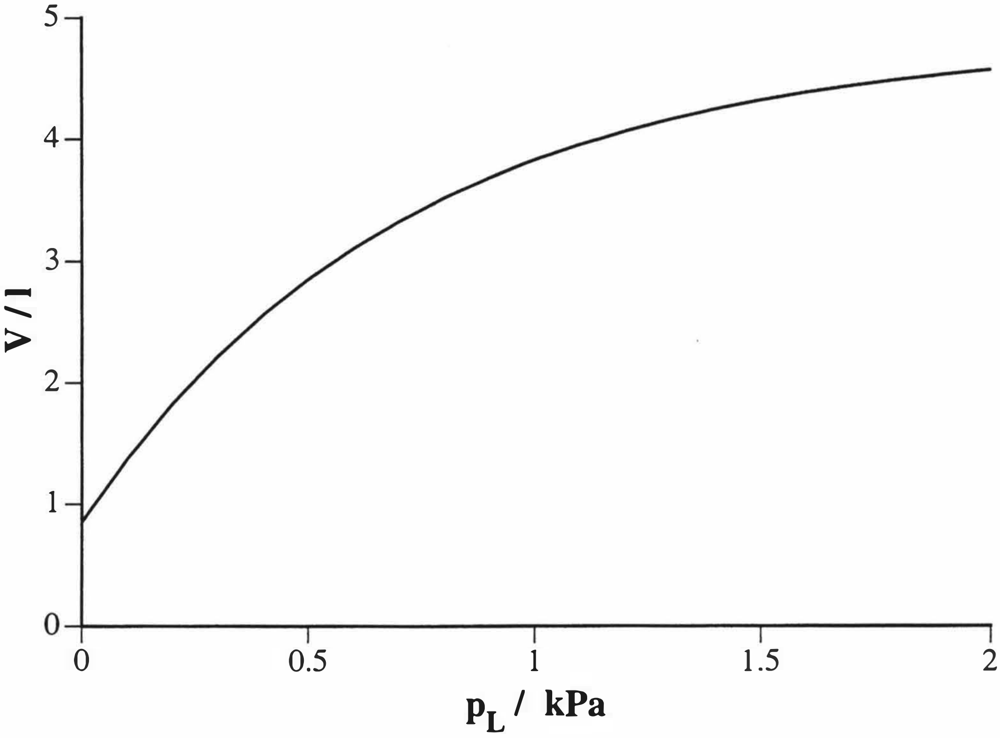

Fig. 2.2. Volume-pressure $V(p_L)$ relationship used in the model. The curve shown is an average curve of five lungs reported by Hyatt et al. [35].

The function used to describe the pressure-volume curve is given by

$$V(p) = V_T - V_{VC}\left(1 - \frac{p}{p_0}\right)^{-n}$$
$$p_0 = -\frac{n(1 - V_0)}{V_0'} \qquad (2.8)$$

where V_T is the total lung capacity TLC, V_{VC} is the vital capacity volume and $V_0' = dV/dp$ at $p_L = 0$. $V(p_L) = 0$ is the lung residual volume (RV). The actual values used are given in the appendix.

2.2 Review of resistance model

The model to be reviewed is a modification of the model initially developed by Wiggs et al [109]. It was designed to simulate dose-response relationships of airway resistance against the dose of a hypothetical bronchocontricting agent that causes smooth muscle shortening. The bronchial tree in the model is depicted as the symmetric bifurcating tree proposed by Weibel [103]. The composition of a model airway and the nomenclature used are shown in Fig. 2.3.

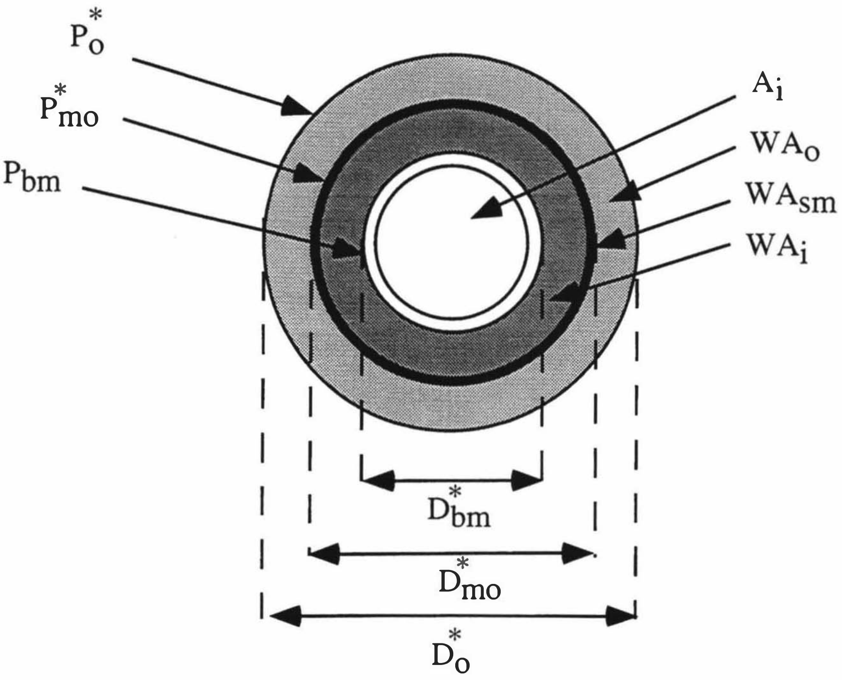

Fig. 2.3. Schematic diagram of fully distended airway showing subdivisions of wall area and nomenclature used (see text for details). Wall areas have been greatly exaggerated for clarity of labelling.

The idealised model bronchus shown in Fig. 2.3 is assumed to be of circular shape and its wall subdivisions are arranged around the lumen area. P_x, D_x and WA_x are external perimeters, external diameters and wall areas, respectively. The subscripts are *o*: outer, *e*: external to smooth muscle, *bm*: basement membrane, *i*: internal, and *sm*: smooth muscle. An asterisk indicates the maximal value of the parameter. A_x is the area enclosed by P_x. The outer adventitial perimeter P_o^* is defined as the perimeter of the border between the adventitia and the surrounding alveolar spaces P_{mo}^* is defined as the external perimeter of the outer border of the smooth muscle. The thickness of the basement membrane is assumed to be negligible. The subdivisions of the airway wall are related to the areas bounded by the different perimeters

$$
\begin{aligned}
WA_0 &= A_0 - A_{mo} \\
WA_i &= A_{mo} - A_{bm} \\
WA_{sub} &= WA_i - WA_{sm}
\end{aligned}
\tag{2.9}
$$

where WA_{sm} is the area of the wall consisting of smooth muscle. The wall areas WA_x are assumed to remain constant during smooth muscle contraction [39].

The perimeter of the basement membrane P_{bm}, which is assumed to be independent of transmural pressure differences, can be used as a marker for airway calibre [10, 41]. The relationship between airway size and different wall components were incorporated by the method of Kuwano et al. [47].

$$\sqrt{WA_x} = slope_x \times P_{bm} + Intercept_x \tag{2.10}$$

The parameters ($slope_x$ and $intercept_x$) used in the model are given in the appendix. Baseline airway diameters are assumed to be measured at a recoil pressure p_L of 0.8 kPa (~75 % TLC) [103]. Since the thickness of the epithelial layer was assumed to be negligible, P_{bm} is assumed to be equal the internal perimeter P_i at 0.8 kPa. P_{bm} can be computed by using Eq. (2.6) and is

$$P_{bm} = \sqrt{4\pi\alpha(0.8\,kPa)A_{max}} \tag{2.11}$$

The model is concerned with the forces acting in and on a bronchus. Three pressures, namely p_p, p_L and Δp, are used to quantify the equilibration of wall forces when the smooth muscle contracts. p_p is the pressure required to equilibrate effective passive tension in the wall. In the absence of any accurate quantitative information about the elastic properties and the passive tensions of the constituents of the airway wall, the net effect of theses forces was modelled by using Eq. (2.6). p_L is the pressure required to equilibrate static recoil pressure of the lung and Δp is the pressure which is required to balance the increased stress imposed by the distortion of the parenchychmal network. Δp has been quantified by use of linear elasticity theory [51] and is

$$\Delta p = 2G\frac{\delta D_0}{D_0} \tag{2.12}$$

where G is the elastic shear modulus of the lung parenchyma. Lai-Look et al. showed that the value for G is between $0.5p_L$ and $0.7p_L$ for dog lungs [50]. G was chosen as $0.7p_L$.

As a result of local parenchymal distortion, the transmural pressure p_{tm} is increased

$$p_{tm} = p_L + \Delta p \tag{2.13}$$

Thus T, the active tension in the muscle, has to balance the difference between p_{tm} and p_p as determined by the Laplace relationship.

$$T/R_{sm} = p_{tm} - p_p \tag{2.14}$$

R_{sm} is the radius of the airway in the middle of the smooth muscle. It is convenient to normalise Eq. (2.14). The natural normalising pressure is p_L and the natural normalising radius is R_{sm} measured at zero smooth muscle shortening. The normalised tension is

$$\begin{aligned} T_N &= \frac{T}{R_{sm}(0)p_L} \\ &= \left(1 + \frac{2G}{p_L}\frac{\delta D_0}{D_0} + \frac{-p_p}{p_L}\right)\frac{R_{sm}}{R_{sm}(0)} \\ \frac{R_{sm}}{R_{sm}(0)} &= 1 + \frac{PMS}{100} \end{aligned} \tag{2.15}$$

where PMS is the percentage by which the smooth muscle is shortened.

The passive stress p_p is given by inverting Eq. (2.6)

$$p_P = p_2\left(1-\left(\frac{\alpha_0 - 1}{1-\alpha}\right)^{\frac{1}{n_2}}\right), \alpha = \frac{A_i}{A_i^*} \tag{2.16}$$

The airways are embedded in the parenchymal network and cause a local distortion of the parenchyma. When no active tension (T= 0) is present in smooth muscle Eq. (2.15) can be used to compute the actual outer diameter of the airway as a result of the parenchymal distortion.

$$1+\frac{2G}{p_L}\frac{D_{OB}-D_{OP}}{D_{OB}}+\frac{-p_P}{p_L}=0 \tag{2.17}$$

where D_{0B} is the "base outer diameter" of the airway, that is when no local parenchymal distortion is present and D_{0P} is the diameter of the airway in the presence of local parenchymal distortion. Eq. (2.17) is solved numerically for the value of D_{0P} at which T is zero. The value of $\delta D_0 = D_{0B} - D_{0P}$ is geometrically related to PMS by Eq. (2.18) [58].

$$\frac{\delta D_0}{D_{OB}} = 1-\sqrt{\frac{WA_0}{A_0}+\left(1-\frac{WA_0}{A_0}\right)\left(1-\frac{PMS}{100}\right)^2}+\left.\frac{\delta D_0}{D_{OB}}\right|_{PMS=0} \tag{2.18}$$

The dose-response characteristic of muscle shortening is based on *in vitro* studies of airway smooth muscle. When a muscle strip is stimulated with increasing doses of an agonist and s the response measured either as isometric tension or as isotonic muscle shortening, the resulting curves are sigmiodal in shape when plotted as the log of the dose versus response on a linear scale [73]. One characteristic feature of smooth muscle dose-response curves in vitro is that no response can be detected, once a particular dose of agonist has been exceeded [69, 73, 112].

The model is driven by a "mathematical dose" of a hypothetical bronchoconstricting agent which provides a systematic method to describe the characteristic S-shaped dose-response curve of smooth muscle shortening as a result of administration of a bronchoconstricting agent. Woolcock proposed the following relationship [112].

$$muscle\,shortening = \frac{10^{\alpha+\beta\log_{10}(dose)}}{1+\left(\dfrac{10^{\alpha}}{1+10^{\alpha}}\right)} \tag{2.19}$$

In Eq. (2.20) α shifts the dose-response curve relative to the dose-axis, with more negative values moving the curve to the right and β controls the slope of the curve, where larger values give a "steeper" response. Eq. (2.19) can be modified to Eq. (2.20) that is, PMS equals zero at a log dose of 1 and reaches a maximum of 1 in an S-shaped manner.

$$PMS = \frac{\left(\dfrac{10^{\alpha+\beta\log_{10}(dose)}}{1+10^{\alpha+\beta\log_{10}(dose)}}\right)-\left(\dfrac{10^{\alpha}}{1+10^{\alpha}}\right)}{1-\left(\dfrac{10^{\alpha}}{1+10^{\alpha}}\right)}\times 100 \tag{2.20}$$

The values of α = -1.9 and β = 1.2 were used to obtain a 50% response in 1.5 log "doses". Fig. 2.4 shows the dose-response curve based on Eq. (2.20) [109].

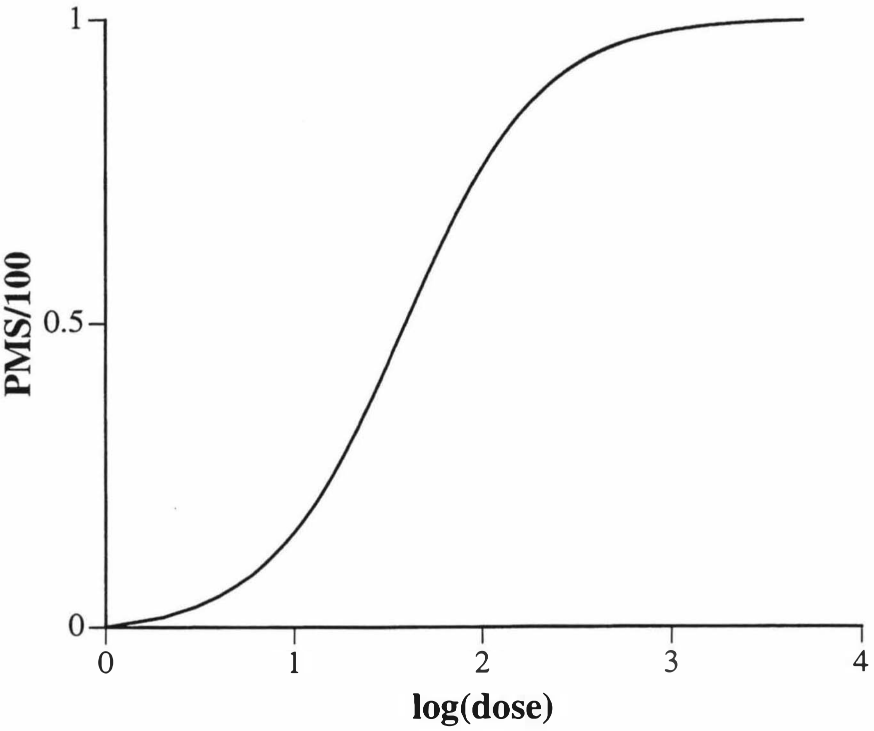

Fig. 2.4. S-shaped dose response curve based on Eq. (2.20)

Eq. (2.20) is used as a mathematical analogy for a (hypothetical) agonist causing smooth muscle shortening as the result of a mathematical dose. The model evaluates T_N from Eq. (2.15) for every dose. From this tension, the stress σ in the muscle is calculated and this value is compared with the maximal stress, the muscle is capable of generating at this muscle length. If the computed stress does not exceed the maximal value the new reduced cross-sectional lumen area A_i is calculated. Maximal smooth muscle shortening, in response to airway smooth muscle stimulation, is determined by the balance of maximal muscle tension determined from the active stress-length relationship of airway smooth muscle and the calculated elastic loads against which the muscle is working. The resulting maximal value in Raw (or FEV_1) is therefore generally not dictated by the plateau shown in Fig. 2.4. The resulting plateau shown in Fig. 2.4 is primarily a consequence of paramacologically induced muscle activity. The plateau value in Raw (or FEV_1) is determined by the balance of forces.

Lambert's published model [58, 59] used data from porcine trachealis for the active stress-length relationship [37]. More recently, Ishida et al. obtained stress-length data from human main stem bronchi [38]. In the work reported here the human data were incorporated into the model. In agreement with the published RM, L_{max}, the length at which maximal active tension can develop was assumed to be at a transpulmonary pressure of $p_L = 1$ kPa [30]. The stress σ, that the circumferential airway muscle of any generation could develop was calculated by using the thickness of smooth muscle t_{sm} at $p_L = 1$ kPa [59] and is

$$\sigma = T_N p_L \frac{R_{sm}}{t_{sm}} \tag{2.21}$$

2.3 Merging of models

The computation of expiratory flows through airways subject to bronchoconstrictive agents requires that one knows how the airway compliance is affected by the muscle activity. That is, it is necessary to know how α_0, α_0', n_1 and n_2 and the reduced maximal luminal cross-sectional area A^*_{Dosed} change with muscle activity.

In vitro data, recently obtained from isolated human airways showed that the specific compliance of airways subject to smooth muscle contractions are very similar if not identical to airways in which there is no active tension present [55]. This together with the absence of any in vivo information, dictates the assumption of α_0, α_0', n_1 and n_2 being identical for dosed and non-dosed airways.

The new reduced maximal cross-sectional area A^*_{Dosed} can be computed from geometric considerations.

$$A^*_{Dosed} = \frac{A_i}{\alpha(p_{tm})} \tag{2.22}$$

With the knowledge of the new set of "dosed" functions one can start the expiratory airflow computations described below.

3. Computational procedure

The new model computes IVPF curves as a function of bronchoconstrictor dose by the following procedure. For each value of VC, a small value for $\dot{V}$ is chosen (0.1 ls^{1}). Eqs. (2.5) and (2.6) are solved at the entrance of generation 16. Then Eq. (2.2) is integrated along the airway, using A^{*}_{Dosed}, α_0, α'_0, n_1 and n_2. Eq. (2.5) and (2.6) are solved numerically at the entrance to the next junction. The procedure is repeated for each generation up to generation 0 (trachea) to obtain the overall pressure decrease at the assumed flow. The value of $\dot{V}$ is then incremented ($\Delta\dot{V}$ = 0.1 ls^{-1}) and the procedure repeated until one of the following conditions occurs: (i) U exceeds c at some point in the bronchial tree (ii) there is no simultaneous solution to Eqs. (2.5) and (2.6) indicating that wave speed would have been exceeded passing through the junction, or (iii) the pressure becomes less than –10 kPa. When one of these occurs, the flow increment is halved. Computations are stopped when maximal flow is exceeded and the flow increment is 0.0025 $\mathrm{l\ s}^{-1}$.

IVPF curves are generated from 80% VC to 5% VC in 5% decrements. The plateau values of the IVPF curves are used to generate a MEFV curve. The effort-dependent part (> 80% VC) of the MEFV curve is approximated by linear interpolation from zero (100% VC) to maximal flow (80% VC). The expired volume within 1 second (FEV_1) is computed as the lung volume difference between total VC and the VC after the time of one second expiration. The calculation of FEV_1 requires a knowledge of the time course of expiration. Time is not expicit in the model. Therefore a subsidiary calculation is performed as follows.

The time Δt_i to deflate the lung from any V_i to V_{i+1} is

$$\Delta t_i = \int_{V_i}^{V_{i+1}} \frac{dV}{\dot{V}} \tag{2.23}$$

As an approximation, flow is assumed to decrease linearly between V_i and V_{i+1}.

$$\Delta t_i = \int_{V_i}^{V_{i+1}} \frac{dV}{mV+b} = \frac{1}{m} ln(mV+b)\Big|_{V_i}^{V_{i+1}} \qquad (2.24)$$

The parameters m and b are calculated from the two known end-points of the line. The total time t_{tot} required to deflate the lung to any VC can then be evaluated by

$$t_{tot} = \sum_i \Delta t_i \qquad (2.25)$$

The FEV_1 calculation was stopped when t_{tot} exceeded one second. The exact expired volume at t_{tot} = 1s was evaluated by linear interpolation.

Smooth muscle dosing was performed starting from a dose of zero in increments of one dose "unit". For each increment, the geometry (A^*_{Dosed}) was computed for all generations at the actual VC. If a new increment would have produced (i) muscle tension larger than maximal tension or (ii) muscle shortening (PMS) less then minimal PMS for any generation, A^*_{Dosed} of the previous dose for that generation was used. IVPF curves were then computed for that geometry. The maximal flow values were used to generate the MEFV curve which, in turn allowed the computation of FEV_1. Computations were stopped when all generations reached the maximal dose for all VC's.

Airway resistance as a function of dose was computed at a relatively low airflow ($\dot{V}$ = 0.5 l s^{-1}). The choice of a low airflow allows the computation of resistance at most VC's and dose without encountering flow limitation.

4. Results

4.1 The normal MEFV curve

The MEFV curve was generated by computing IVPF curves from 80% VC to 5% VC in 5% decrements. Examples of computed IVPF curves are shown in Fig. 4.1.

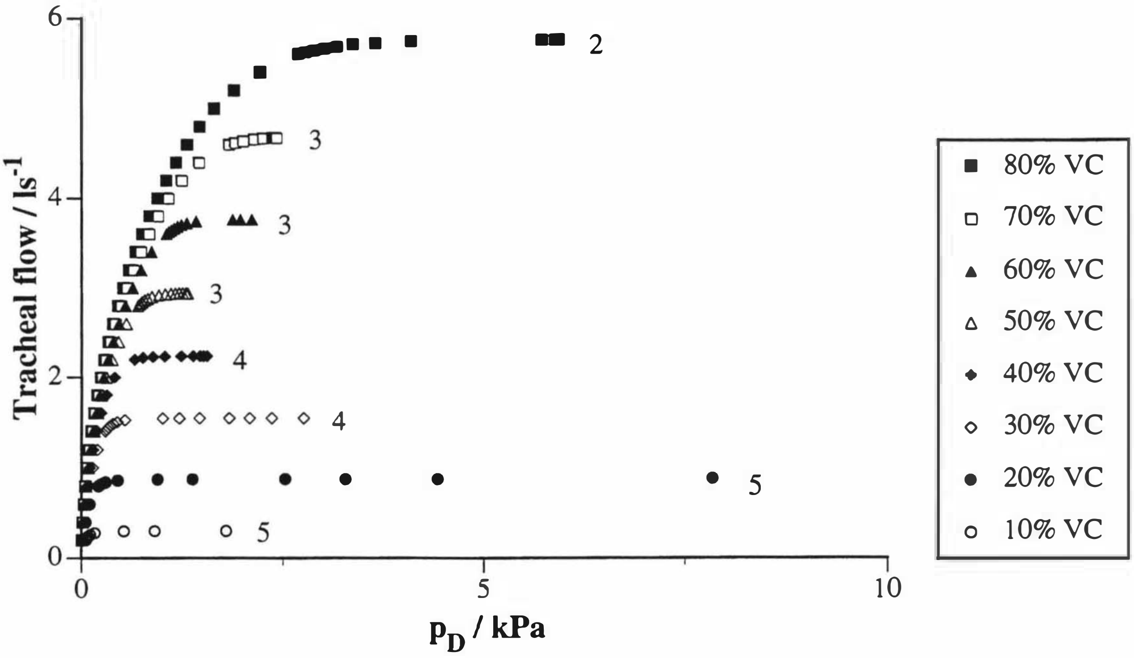

Fig. 4.1. Computed IVPF curves at various VC's. The numbers in the graph indicate the airway generation in which volume flow $\dot{V}$ reached wave speed c and therefore computations had to be stopped. Pressure p_D shown is the computed pressure difference between alveolar pressure and the pressure in the flow at the downstream end of generation 0.

The resulting "normal" MEFV curve is shown in Fig. 4.2. The effort dependent part of the curve (region 1) was linearly interpolated. The filled diamonds represent the plateau values generated by the IVPF computations. To obtain this curve, model parameters were adjusted until the resulting MEFV curve matched the mean data from five excised human lungs [61].

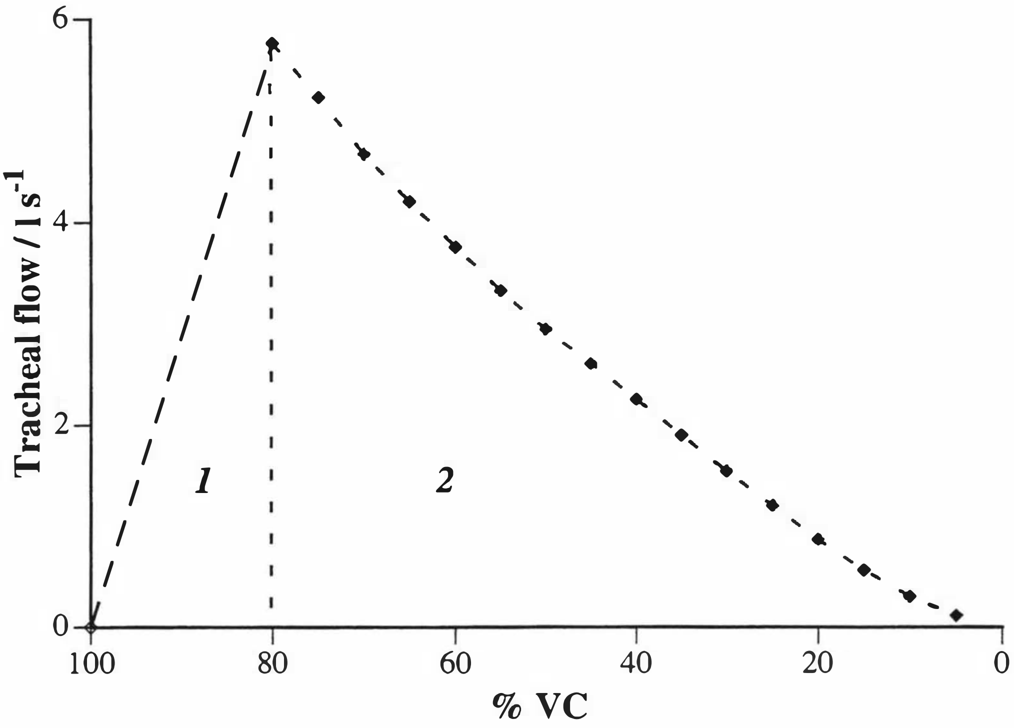

Fig. 4.2. Computed MEFV graph. The effort dependent part of the curve (region 1) is approximated by linear interpolation from zero flow at 100% VC to the maximal flow at 80% VC. The bold diamond symbols in the graph are the plateau values from the IVPF computations (region 2).

4.2 Effect of thickening of airway wall components

The effects of increased airway smooth muscle thickness, adventitial thickness and submucosal thickness on FEV_1 and Raw were investigated using the new model. FEV_1 and Raw were computed as a function of the previously described dose "unit".

Measurements of airflow resistance are normally made at FRC ($p_L \approx 0.5$ kPa). The volume-pressure curve used in the model (Fig. 2.2) shows that p_L equals 0.5 kPa at 2.8 l total lung volume (TLC = 4.85 l, see appendix). This is at approximately 50% VC (VC = 4.18 l, see appendix). Thus Raw computations shown were computed at 50% VC and $\dot{V} = 0.5$ l s^{-1}.

The effect of thickening the adventitial region on FEV_1 and Raw is shown in Fig. 4.3.

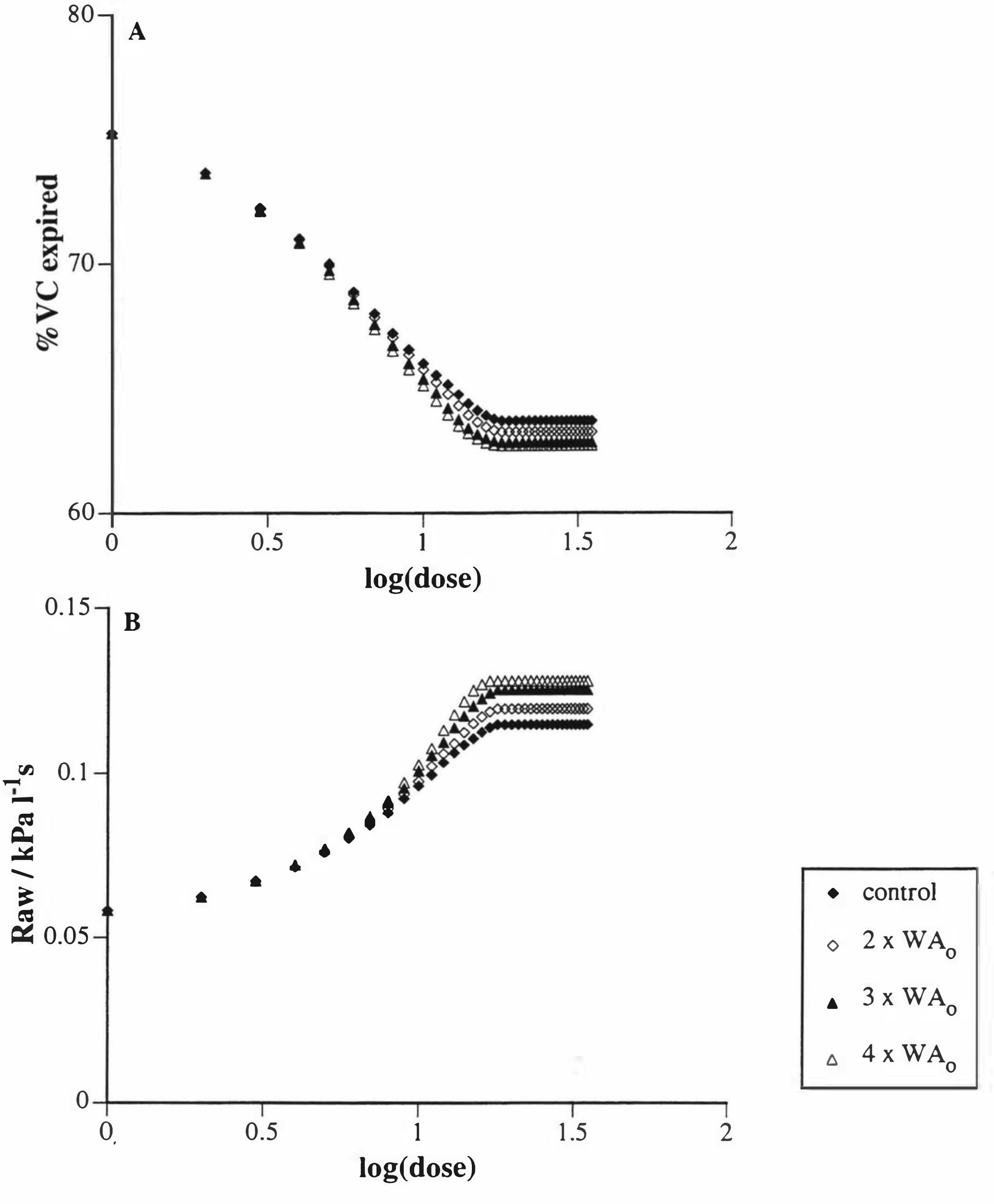

Fig. 4.3. Effect of thickening of the adventital region on A: FEV_1 and B: Raw as a function of log(dose). Raw was computed at 50% VC ($p_L \approx 0.5$ kPa) and $\dot{V} = 0.5$ l s^{-1}.

Fig. 4.4 shows the effect of thickening of the submucosal region on FEV_1 and Raw.

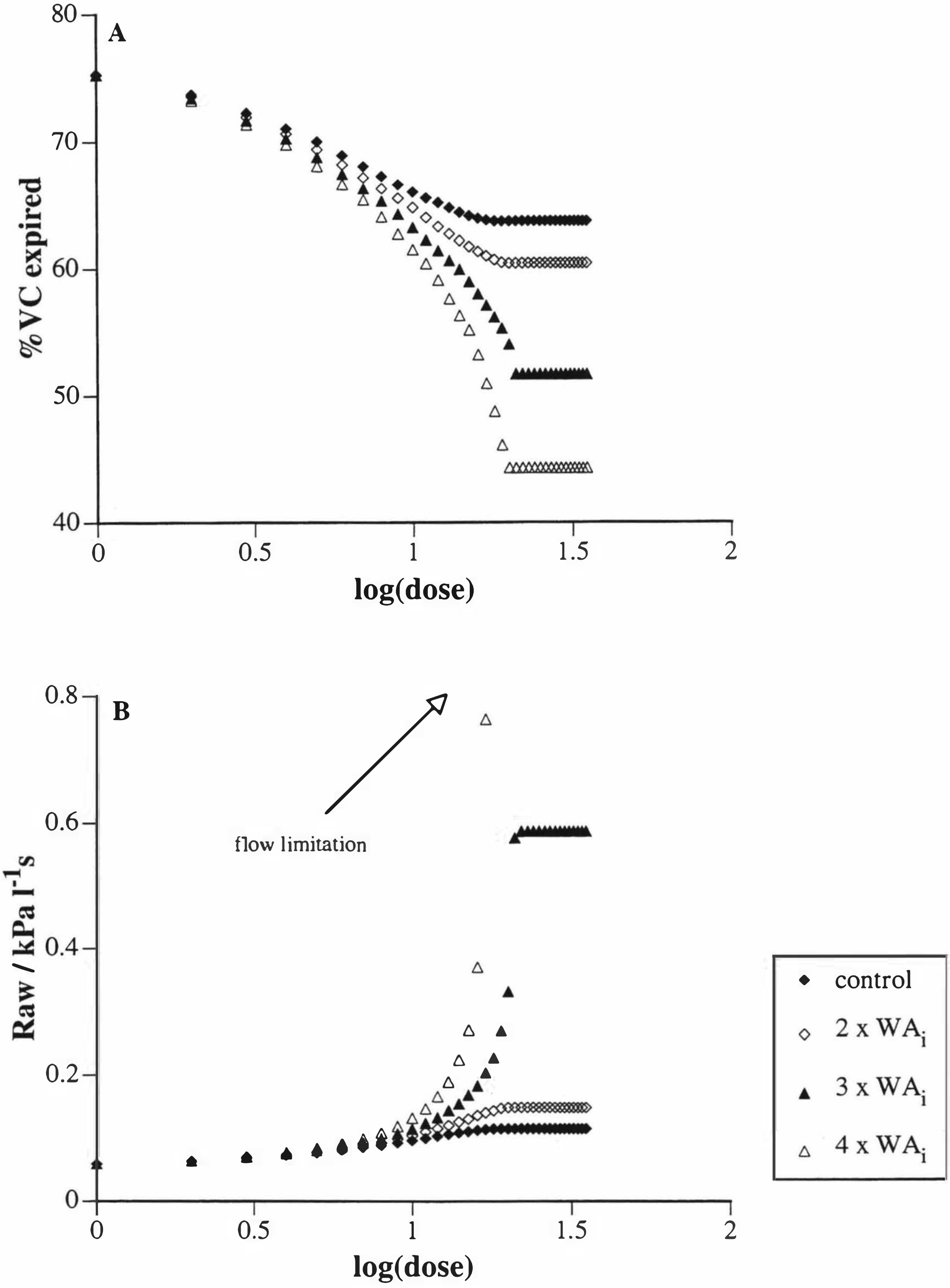

Fig. 4.4. Effect of thickening of the submucosa on A: FEV$_1$ and B: Raw as a function of log(dose). Raw was computed at 50% VC ($p_L \approx 0.5$ kPa) and $\dot{V} = 0.5$ l s^{-1}. For the 4 × WA$_i$ results, flow limitation was encountered at a flow less than 0.5 l s^{-1} and Raw calculations were stopped.

The effect of increasing the airway smooth muscle mass is depicted in Fig. 4.5.

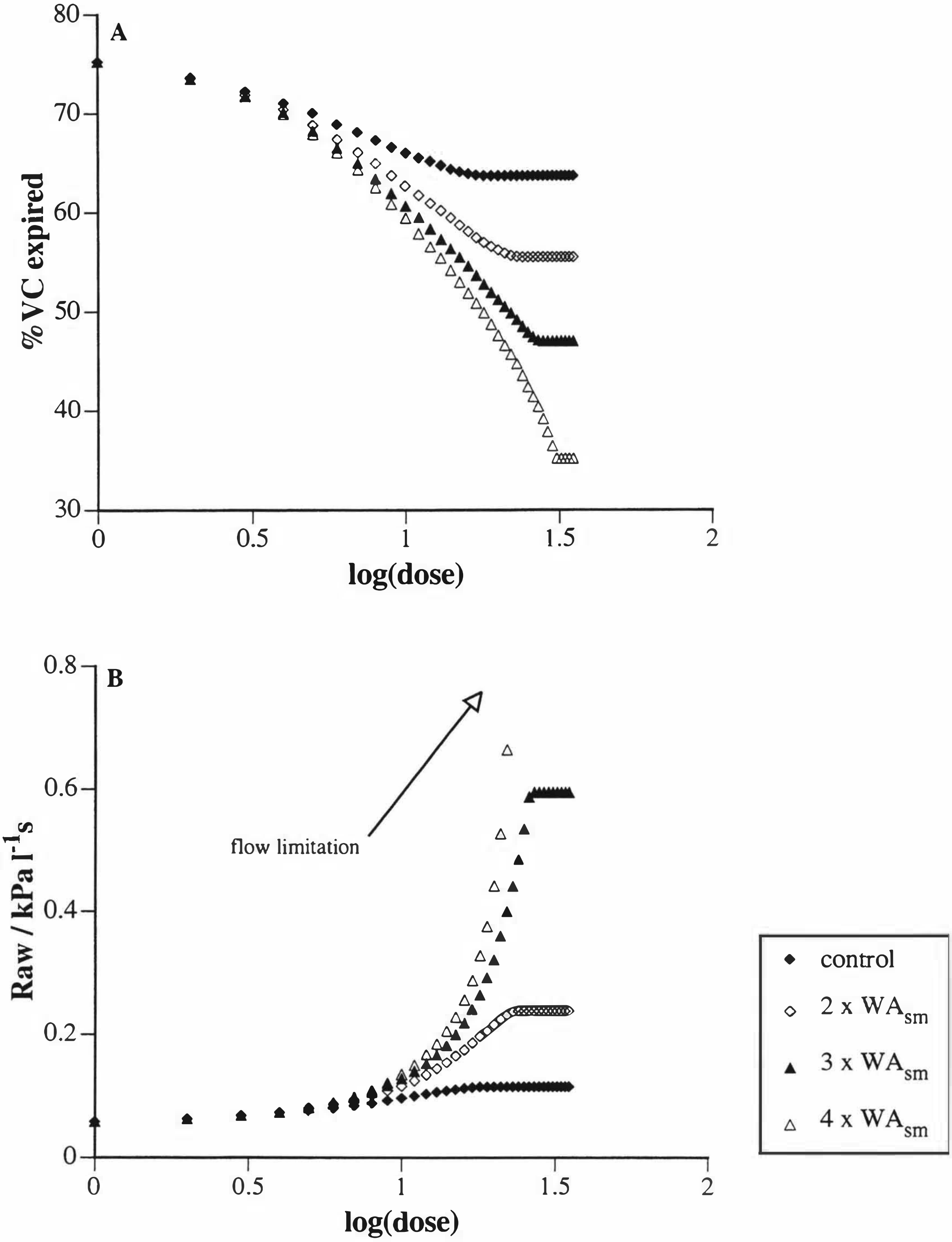

Fig. 4.5. Effect of thickening of smooth muscle mass on A: FEV$_1$ and B: Raw as a function of log(dose). Raw was computed at 50% VC ($p_L \approx 0.5$ kPa) and $\dot{V} = 0.5$ l s^{-1}. For the 4 × WA$_{sm}$ results, flow limitation was encountered at a flow less than 0.5 l s^{-1} and Raw calculations were stopped.

Morphological wall data are also known from asthmatics and COPD patients [48]. The results of employing these data for the wall areas is shown in Fig. 4.6.

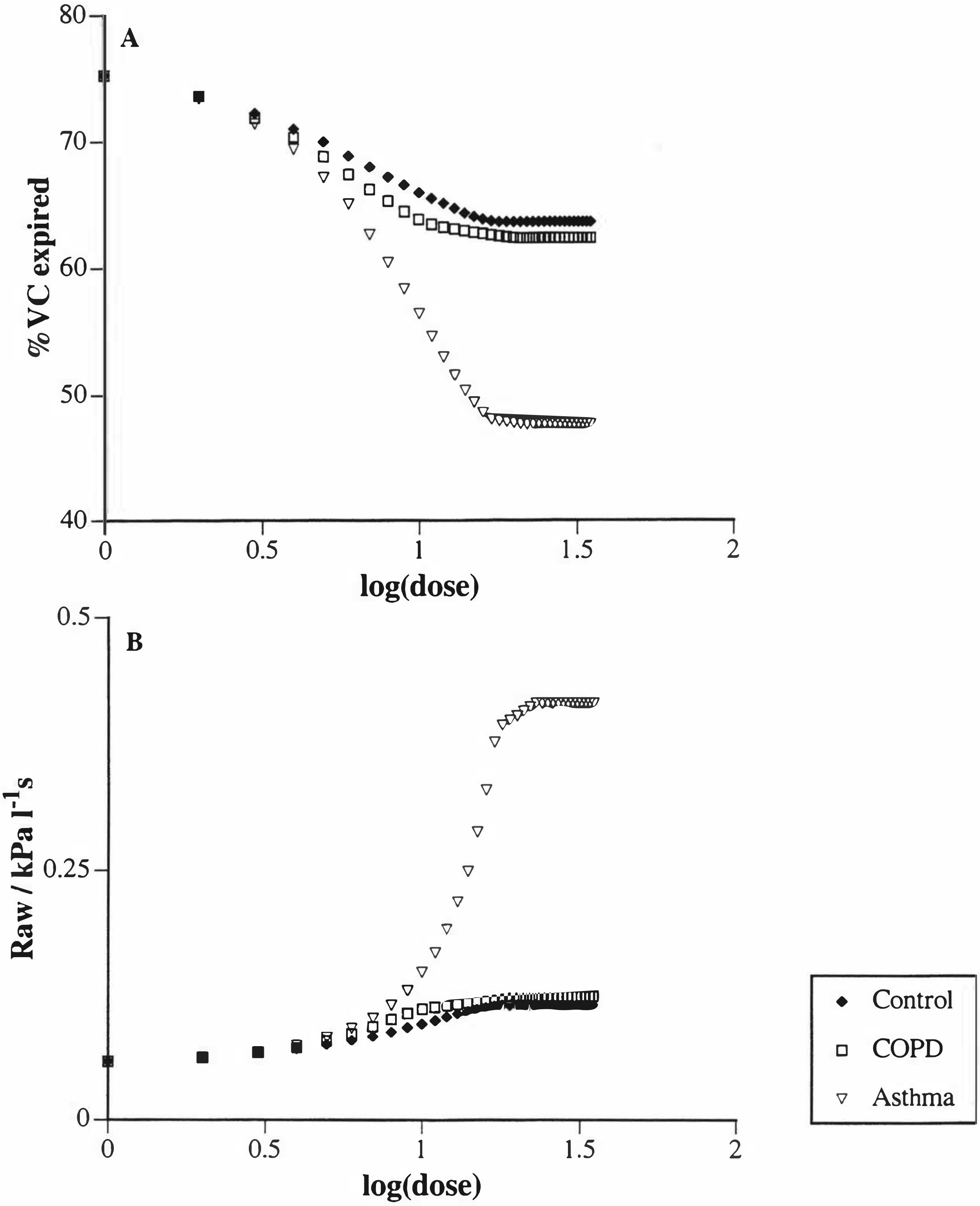

Fig. 4.6. Effects of employing morphometric data from asthmatic and COPD patients on A: FEV_1 and B: Raw as a function of log(dose). Raw was computed at 50% VC ($p_L \approx$ 0.5 kPa) and $\dot{V} = 0.5\ \mathrm{l\ s^{-1}}$.

5. Discussion

The model presented here is based on the well-established model for forced expiratory flow [61] and on the "resistance model" (RM) which was developed to investigate effects of airway remodelling on airway resistance [59]. The weakness of the forced expiratory airflow model is that it does not consider any structural changes in the airway walls. On the other hand, the RM cannot be used to study effects of airway remodelling on dynamically compliant airways. Merging of both models should therefore give more realistic insights into how morphometric changes of the airways as they occur in disease affect forced expiratory airflow and resistance to airflow during quiet breathing.

Changes from published models

One of the major differences between the published RM and the new model is the active stress-length relationship used. Lambert et al used data from porcine trachealis muscle [37]. The active stress-length relationship implemented in the new model is based on data obtained from human main stem bronchi [38]. The previously used porcine data show a maximal isometric stress of 1.47×10^5 Pa and a maximal shortening to 32% of L_{max} [37]. Human main stem bronchi, however, are only capable of generating a maximal isometric stress of 4.9×10^4 Pa and a maximal shortening to 54% of L_{max} [38][1].

An additional difference between the published RM and the new model is the value of dose "unit" increments. Increments in the published RM were chosen to be dependent on the change in Raw between two dose increments. If the difference was too large, the step size was reduced and resistance was re-calculated for the smaller step size thus making the computation more sensitive to the onset of the plateau. The new model simply increments dose units in steps of one, independent of the magnitude of resistance changes. This has the advantage of a unified "dose scheme" for all states of lung deflation but also results in a decreased sensitivity of the computational model.

A further important difference is that in the new model the airway compliance is reduced with increasing dose. It has been known for many years that an airway is

---

[1] The data published by Ishida et al. are not clear regarding the maximal active muscle shortening. The value of 54% is therefore the shortest length value shown in Fig. 1 of reference [38].

stiffened by the activation of the smooth muscle. However, it has not been clear how this stiffening should be modelled. The new data from Tiddens's laboratory [55] was used as a basis for the stiffening incorporated in the new model. The compliance of the airways is now re-computed at each dose step rather then being held constant as was previously done [59, 61], although the specific compliance remains unchanged (α_0, α'_0, n_1, n_2). The maximal airway cross section A^*_{Dosed} becomes a function of dose and recoil pressure p_L. Fig. 5.1 depicts as an example the change of the compliance of generation 5 with increasing dose at 80% VC.

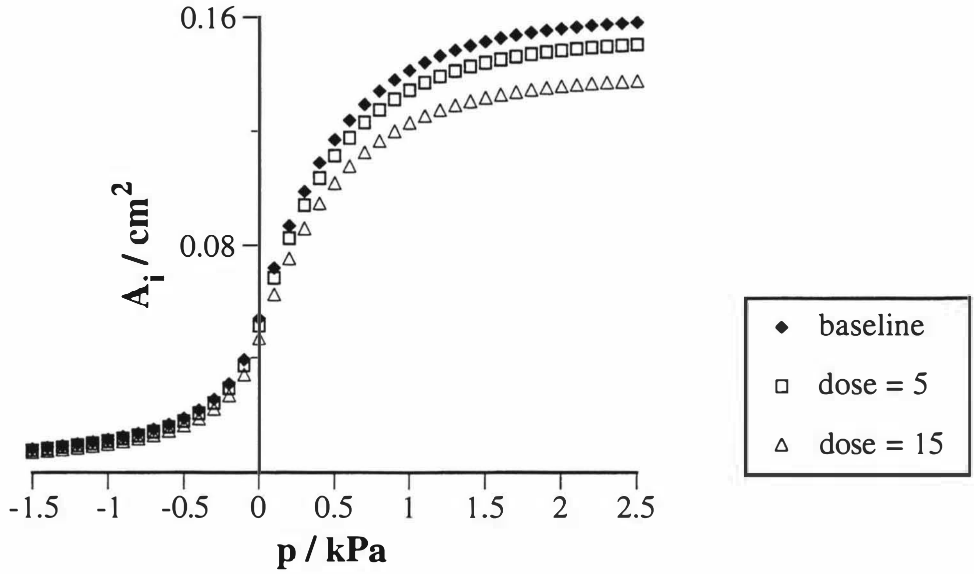

Fig. 5.1. Change of compliance curve as a consequence of dose "unit" for airway generation 5 (control). p is airway transmural difference.

A subject of controversy is the question of whether thickened smooth muscle can generate more tension than normal muscle. The very little data available are conflicting [90]. Therefore, in agreement with the published RM I assume that the maximal stress thickened smooth muscle can generate is the same as in normal muscle and thus the maximal tension with thickened muscle is greater than in the normal case.

Baseline values

FEV$_1$ was computed by subdividing the MEFV curve into two regions, region 1, the effort-dependent part and region 2 which was generated by using the plateau values given by the IVPF computations. Although the effort-dependent onset of the MEFV curve is known to be non-linear [97, 105] it was linearly approximated. The computed time to deflate the lung from 100% VC to 80% VC (region 1) was approximately 0.15 s which is in good agreement with experimental data [1] thus making this a good approximation. Literature data are conflicting regarding FEV_1 in health. Some define a normal FEV_1 value at about 80% VC [105], others consider FEV_1 less than 70% VC as the threshold for disease [28]. The computed baseline FEV_1 value was 75.3% of VC, which can be considered to be near the lower limit for a healthy lung.

The computed baseline value for Raw was 0.06 kPa l^{-1} s at 50% VC (0.09 kPa l^{-1} s at 30% VC) which is lower than most data known from experimental studies. Ding et al, for example, reported baseline data from normal subjects in the range of Raw = 0.1 – 0.3 kPa l^{-1} s at FRC [19]. Wheatley et al. published data from normal humans ranging from Raw = 0.15 – 0.3 kPa l^{-1} s at 30% VC and $\dot{V} = 0.5\ l\ s^{-1}$ [106]. One reason for this discrepancy is that the computational model does not include any resistance downstream of the intrathoracic trachea, that is in the extrathoracic trachea, larynx, pharynx or in the mouth. Resistance changes in the larynx and pharynx for example are known to be in the range of 0.05 kPa l^{-1} s [28]. In addition the model does not include any viscous tissue resistance losses of the lung and the chest wall, which account for about 20% of the total measured resistance in young normal subjects [105]. Also, Ding et al did not state the actual flow at which they measured Raw [19]. Experimental measurements are normally made at higher flows in the range of 1 l s^{-1}. The computational results are based on $\dot{V} = 0.5\ l\ s^{-1}$. Computations at a larger $\dot{V}$ value would have yielded a higher Raw because of the increased contribution from the turbulent dissipation term in f (Eq. 2.4). Considering these effects would bring the computed value of Raw in the range of Raw $\approx$ 0.15 kPa l^{-1} s at 50% VC ($\approx$ 0.17 kPa l^{-1} s at 30% VC) for $\dot{V} = 0.5\ l\ s^{-1}$ which is within the range known from experiments.

Thickening of airway wall compartments

Morphometric changes such as thickening of wall areas of the airways are well known features in asthmatic and COPD patients [10, 20]. The major finding of the RM was that increased smooth muscle is likely to be the most compromising abnormality that is responsible for increased airway resistance [59]. The more realistic approach of the new model raises the question of whether these findings are still valid. Therefore, computations were performed to elucidate to which extend the remodelling of each airway wall compartment compromised lung function as measured by FEV_1 and Raw.

Results shown in Fig. 4.3 to 4.5 have been replotted on a normalised basis in Fig. 5.2 to 5.4 for the ease of comparison. Increasing of WA_0 up to four times the baseline value had only a very moderate effect on the depression of FEV_1 and the increase in Raw. The relative changes caused by thickening the adventitia are shown in Fig. 5.2. Thickening of the submucosal region of the wall caused a considerably more severe change in FEV_1 and Raw. The relative changes are shown in Fig. 5.3. Thickening of airway smooth muscle caused similarly severe changes as shown in Fig. 5.4.

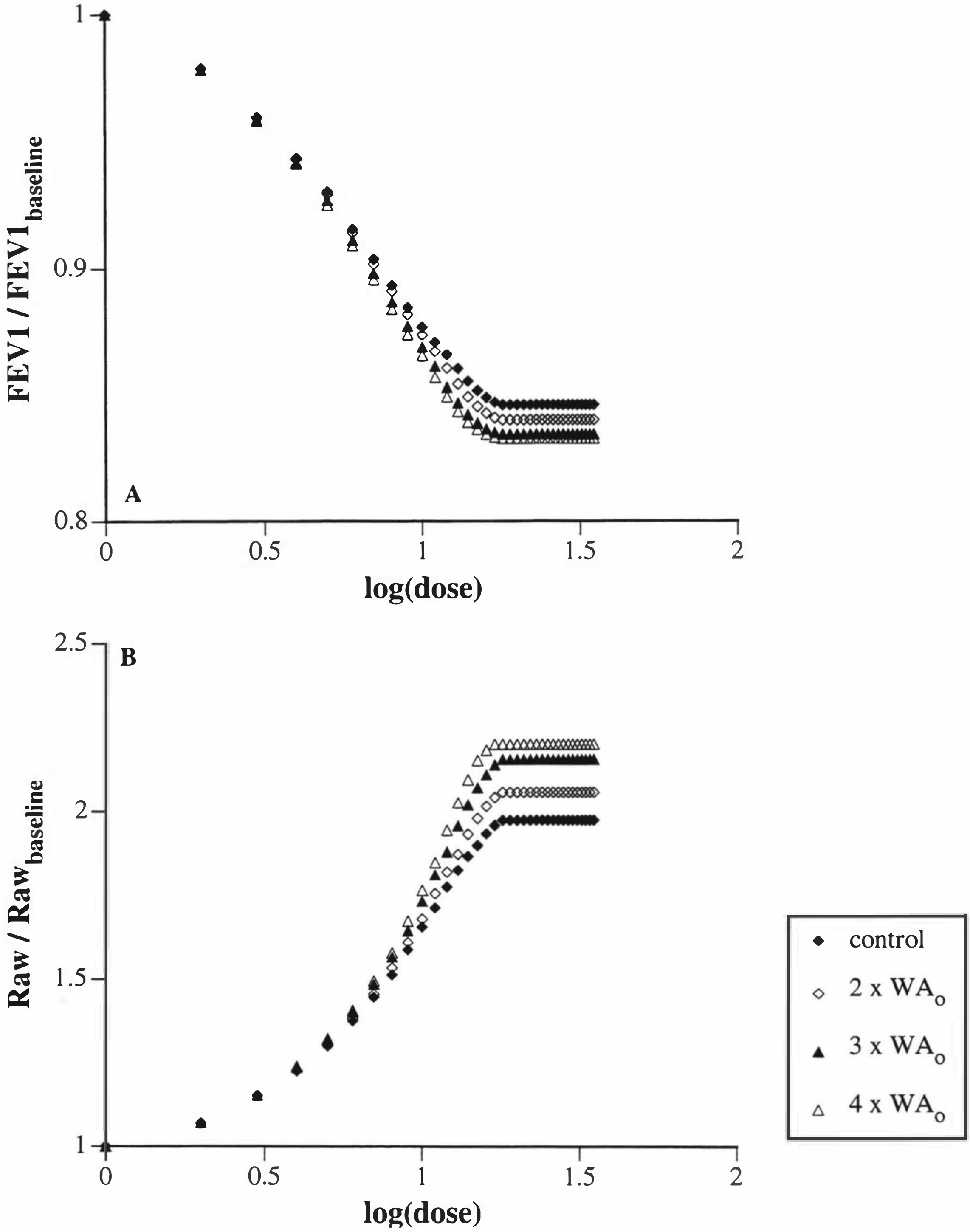

Fig. 5.2. Relative changes of A: FEV$_1$ and B: Raw as a result of increasing the adventitial area WA$_o$.

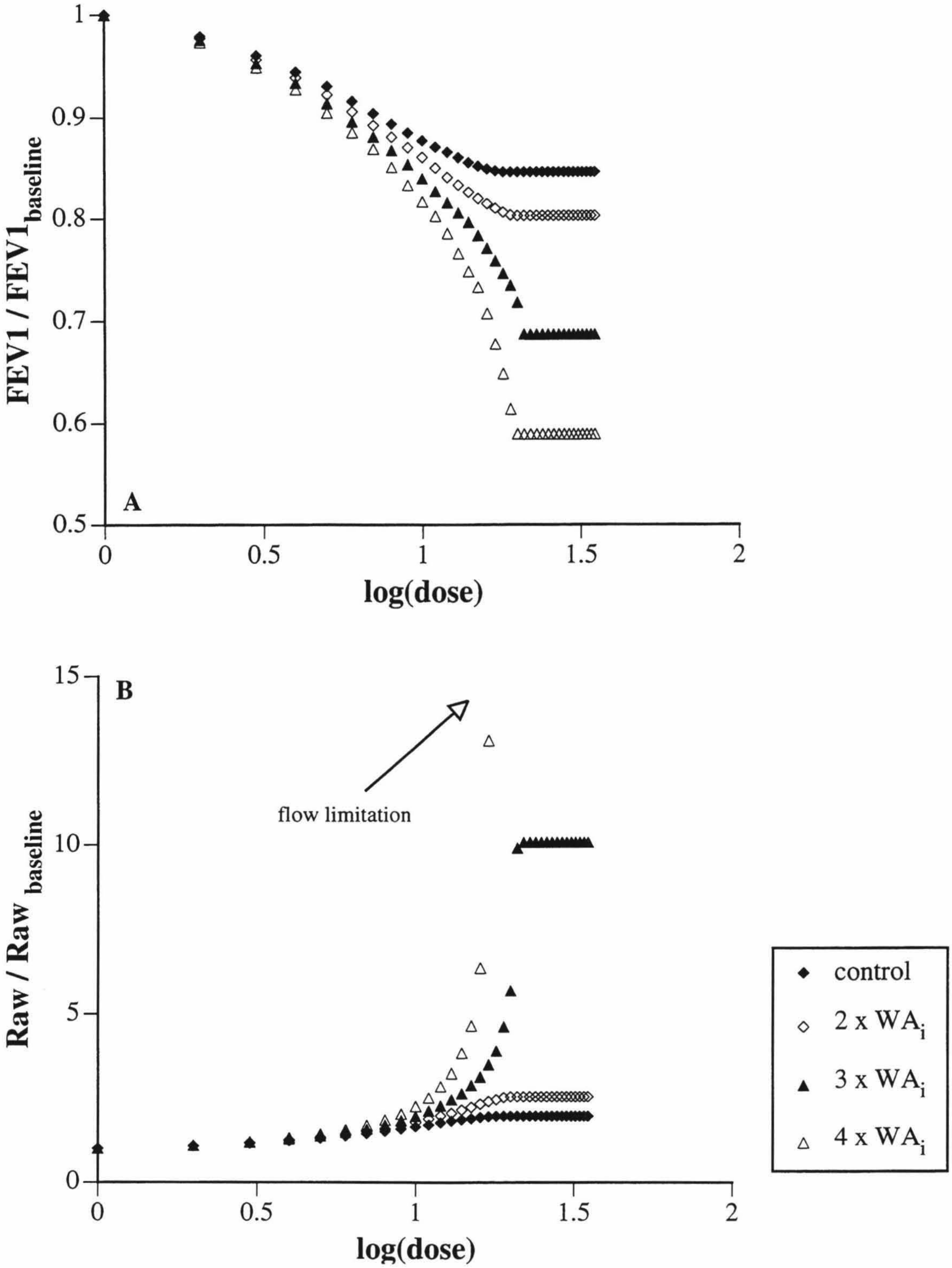

Fig. 5.3. Relative changes of A: FEV_1 and B: Raw as a result of increasing the submucosal area WA_i.

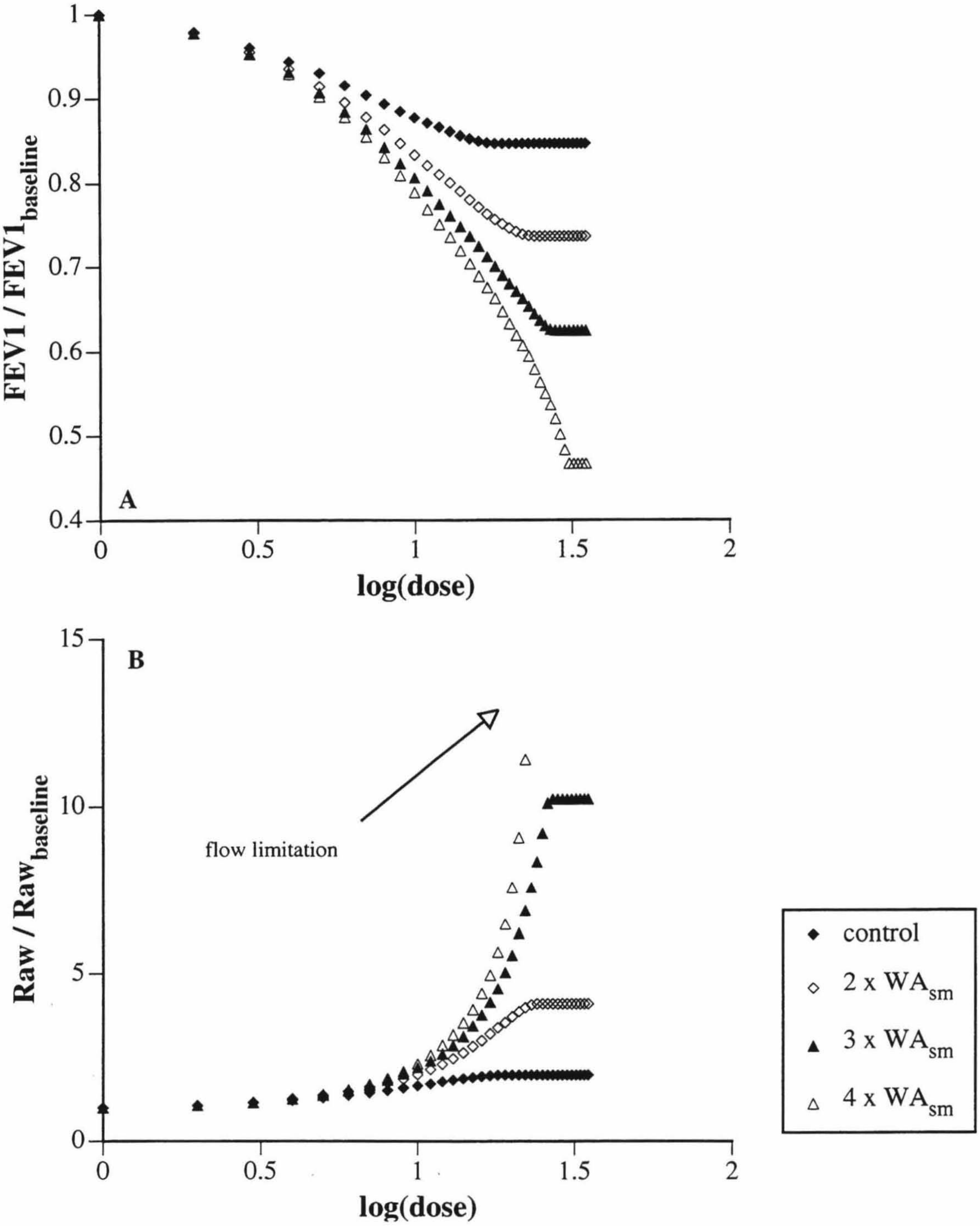

Fig. 5.4. Relative changes of A: FEV_1 (A) and B: Raw as a result of increasing the smooth muscle area WA_{sm}.

Comparing Figs. 5.2 to Fig. 5.4 clearly shows that adventital thickening has only a minor effect on airway responsiveness whereas submucosal thickening and increases of muscle mass can have substantial effects. This is consistent with published results [58, 59]. Comparison of Fig. 5.3 with 5.4 reveals that thickening of submucosa has much the same effect on FEV$_1$ and Raw as thickening of smooth muscle. This is illustrated in Fig. 5.5 for the example of WA$_x$. increased by a factor of three.

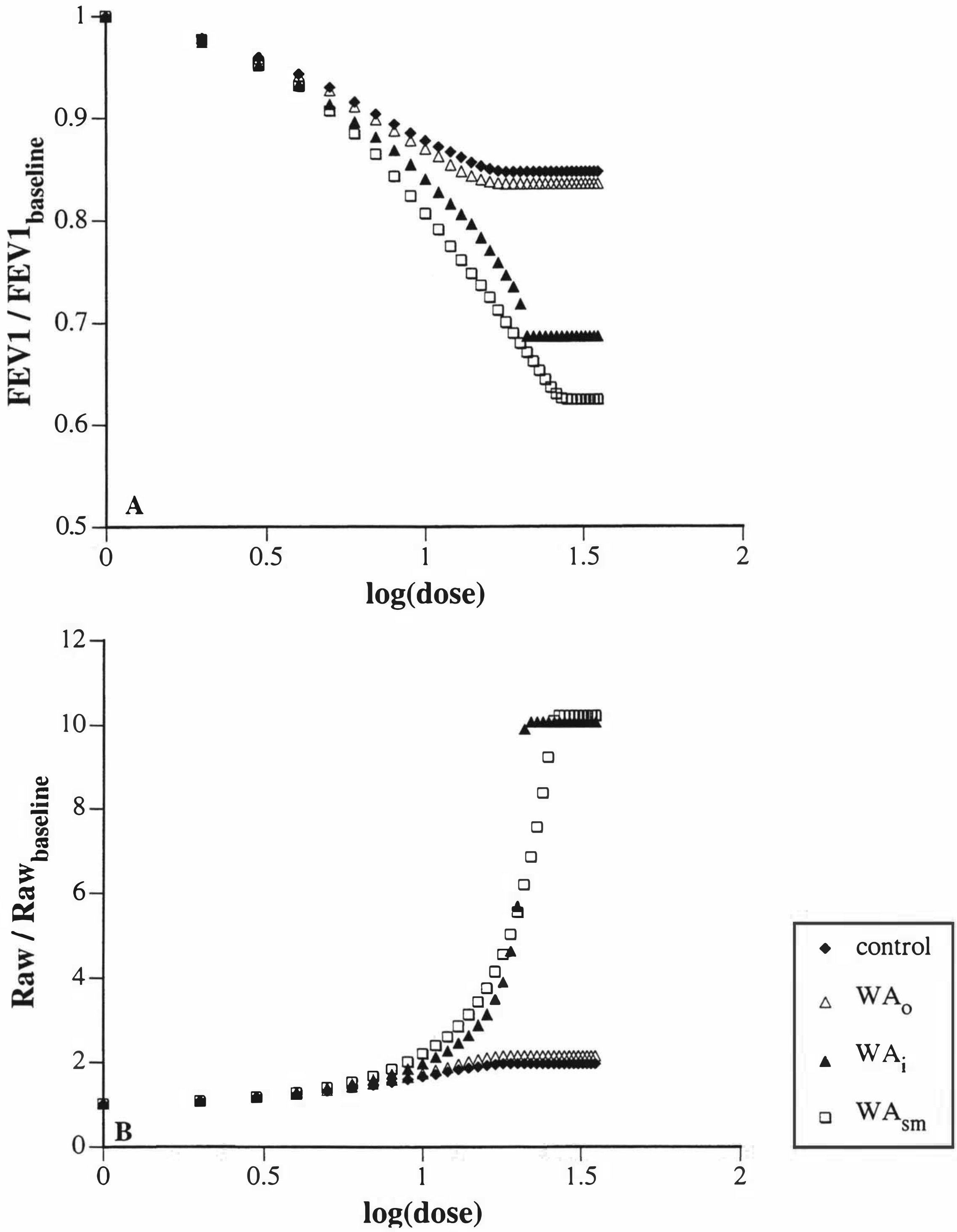

Fig. 5.5. Comparison of changes on A: FEV$_1$ and B: Raw for equally (three times) increased wall areas WA$_x$.

This is somewhat different from Lambert's result where smooth muscle had a greater effect than similar increase in submucosal area. The major (but hardly new) result obtained from this new model is that it is very likely that the most compromising factor in abnormalities found in disease is the increase in airway smooth muscle mass. This is in agreement with previous modelling studies. The new model, however, shows that increased submucosal mass has a more compromising effect, than previously published results showed [58, 59].

Fig.s 5.2 to 5.4 reflect the different ways, in which changes in WA_o, WA_i and WA_{sm} affect Raw and FEV_1. Changes in FEV_1 or Raw caused by increases in WA_o or WA_i result, primarly, from geometric effects. Increased WA_{sm}, on the other hand, directly affects the smooth muscle's ability to generate tension T given by Eq. (2.15) since increased muscle wall area also results in an increased muscle thickness t_{sm}. For a given tension (required by the force balance), increased muscle mass reduces the required stress (Eq. (2.21)). The airway smooth muscle has to shorten further to generate the same stress σ, and thus can shorten further before reacheing maximal stress. This results in an increased narrowing of the airway.

The extra submucosal area WA_i was incorporated by allowing encroachment of thickened inner wall area into the lumen [58] which results in a reduced A_i (Eq. 2.22). The resulting A_i^* (Eq. 2.22) at zero dose obtained by force balance at zero dose is essentially identical with the baseline maximal cross-sectional areas. Increased submucosal wall thickness should result in a slightly decreased FEV_1 (or increased Raw) at baseline. This seems to be a weakness of the model, but there are, however, no data available on how to incorporate the extra WA_i.

COPD and Asthma

The results shown in Fig. 4.6 are based on data derived from a study of small airways dimensions and COPD patients [48]. The relative changes in FEV_1 and Raw are shown in Fig. 5.6.

Fig. 4.6 (and Fig. 5.6) shows a distinct knee starting at a log(dose) of about 1.25 resulting in a subsequent almost linear change in FEV_1 or Raw for asthmatics. At this dose, the smooth muscle in most airway generations has reached maximal tension (or maximal shortening in some generations). A few large airway generations (generations 0 to 2) have still not reached this condition and thus are able to shorten further. Consequently any further increments in dose will cause only smaller changes in Raw or FEV_1.

Thickening of the smooth muscle of up to four times caused a depression in FEV_1 to 45% (Fig. 5.4A) of the baseline value whereas FEV_1 for asthmatics plateaued at about 60% of baseline value. Raw with $4 \times WA_{sm}$ (Fig. 5.4B) exceeded flow limitation where Raw could be calculated with asthmatic data (Fig. 5.6A). This is an apparent contradiction because in asthma not only is WA_{sm} increased by at least a factor of four but all other wall compartments are also enlarged [77]. Hence, at first glance, it would be reasonable to expect an even greater depression in FEV_1 and the computation of Raw should have shown the same flow limiting effect as in the cases of four-fold increase in WA_i and WA_{sm}.. The cause of these discrepancies are the extrapolations made from the regression data for the wall compartments (Eq. 2.10). The measurements of wall dimensions in the asthmatic airways were limited to membranous bronchioles with P_{bm} between 0.7 and 7 mm [48], thus spanning the range of airways from the 16th to about the 8th generation in the Weibel model. The extrapolations to more centrally located airways made from the regression data for wall components are questionable. Tiddens et al for example pointed out that at least for patients suffering from COPD there are differences in wall area compartments between cartilaginous and non-cartilaginous airways [98]. Fig. 5.7 shows the change of the airway wall compartments with increasing internal perimeter.

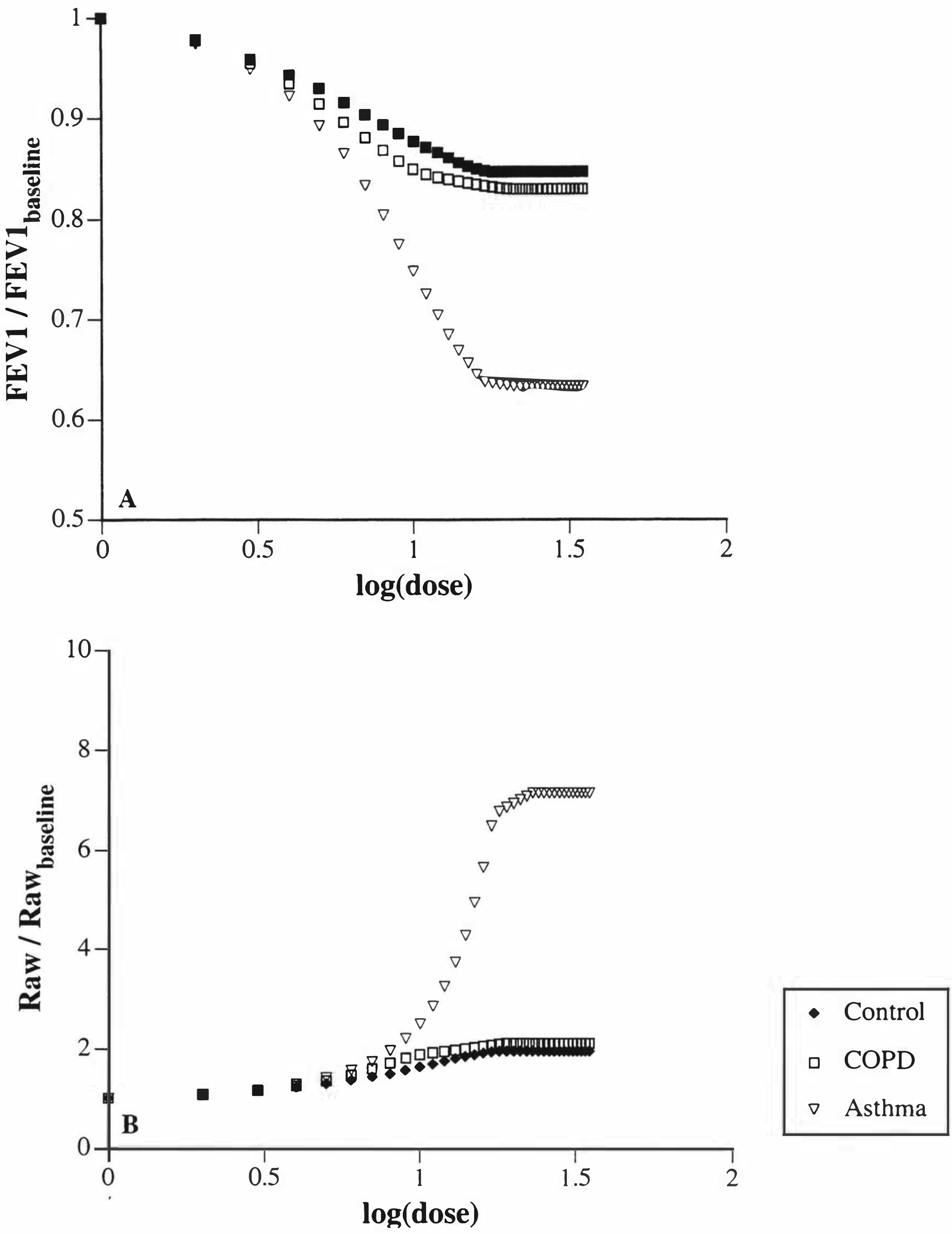

Fig. 5.6. Relative changes of A: FEV_1 and B: Raw for data obtained for COPD and asthma.

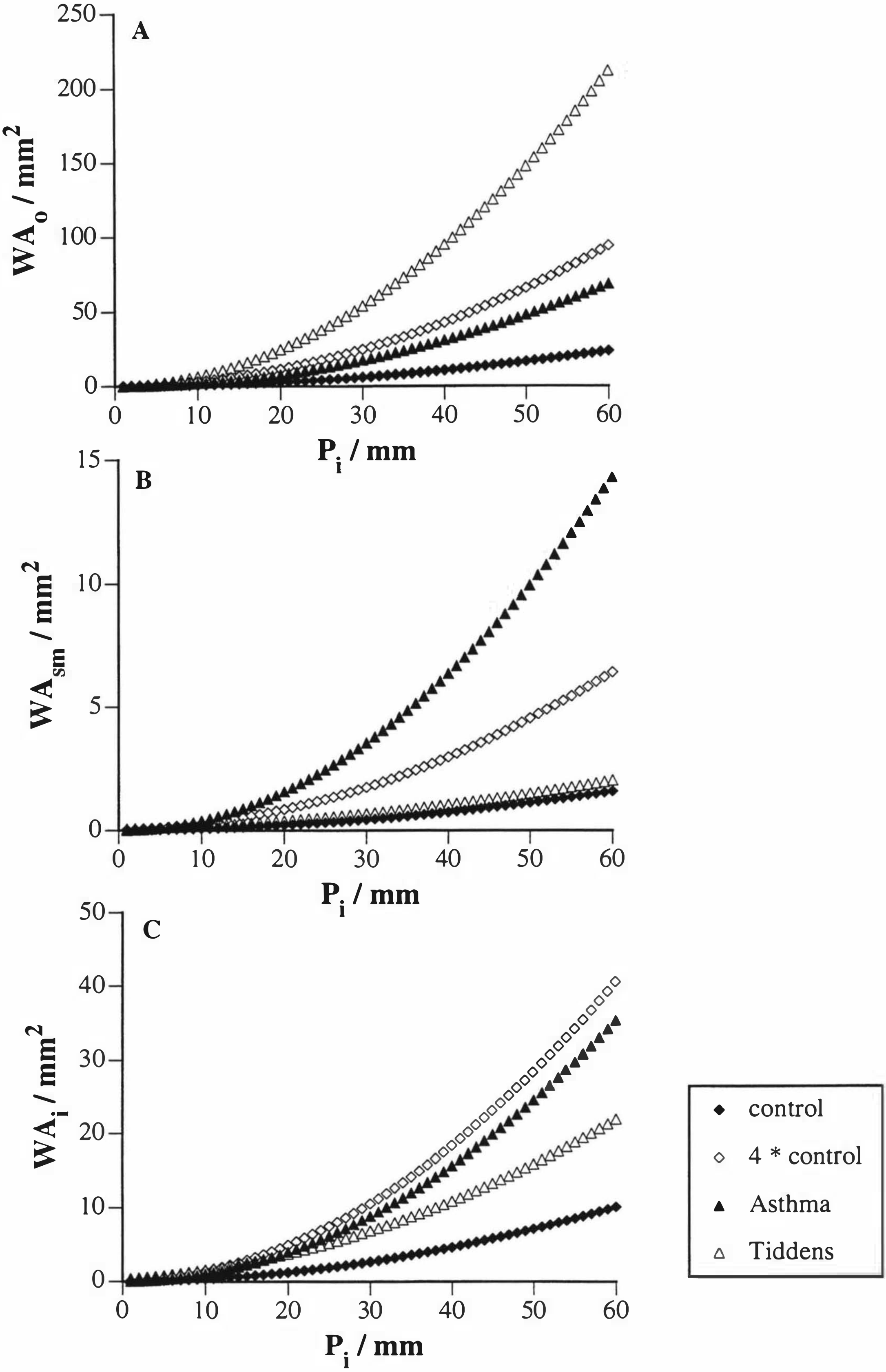

Fig. 5.7. Wall area compartments A: external to smooth muscle, B: smooth muscle and C: internal to smooth muscle computed by the method of Kuwano et al. [47].

Fig. 5.7A shows for example, that the outer wall area WA_0 is probably considerably thicker for central airways than for peripheral airways. Also, Fig. 5.7B shows that, at least for asthmatics, the airway smooth muscle for central airways is probably too thick. This makes this extrapolation of the Kuwano questionable. However, I am unaware of any data that could clarify this contradiction. It would appear to be preferable to find a reasonable way of combining the data sets of Kuwano and Tiddens.

Determinants of plateau in FEV_1 and Raw *curves*

An additional difference from the RM lies in the determinants of maximal smooth muscle shortening. A basic result in Lambert's model is that maximal PMS is determined by the maximal tension that the muscle is capable of generating. An additional possibility of what governs the plateau values of FEV_1 and Raw is the maximal shortening the muscle is able to generate. Lambert et al. used data from porcine trachealis muscle. This muscle is capable of shortening to 32% of L_{max} [37]. All airway generations in the RM reached maximal stress before they reached maximal shortening. Human airway smooth muscle, however only shortens to 54% of L_{max}. In the present model, the plateau values in Raw and FEV_1 can also be governed by maximal allowable smooth muscle shortening. Some airways reach maximal shortening, whereas others reach maximal stress.

Comparison with experimental data

Direct comparison with experimental data is difficult due to a considerable variability of airway responses in normal subjects [31]. A comparison is nevertheless useful to elucidate whether computed values are within a realistic physiological range. The experimental data used for comparison are based on inhalation challenge tests with bronchocontricting agonists on normal subjects. The detailed experimental protocol can be read elsewhere [71]. Fig. 5.8 depicts the experimental data in comparison with the computed control FEV_1 and Raw values.

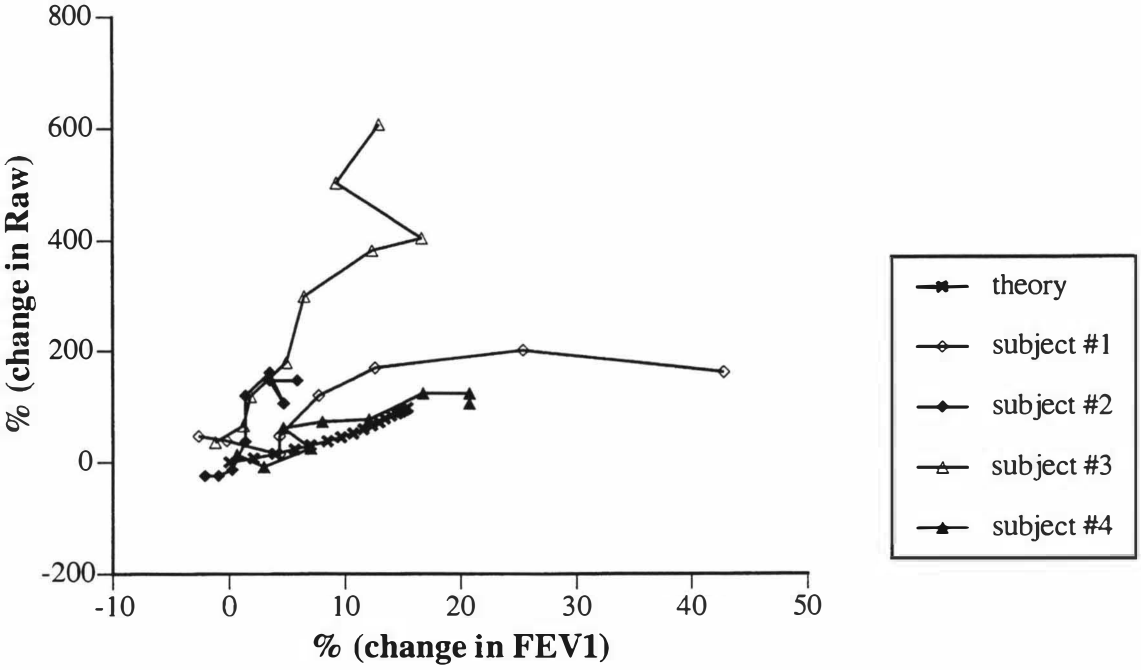

Fig. 5.8. Comparison between computed (control) data and experimental data obtained from normal subjects [71] (Courtesy of Barbara Moore, University of British Columbia Pulmonary Research Laboratory, Vancouver, Canada).

Although biological variability is considerable, model values are within a physiologically realistic range.

In summary, results obtained with the new model are consistent with previously known findings. The major progress in the new model is the incorporation of airway wall structure into the calculation of the MEFV curve thus enabling dose-response calculations to be made. In addition, resistance calculations can now be performed on dynamically compliant airways. This is a more realistic approach in the understanding of the interrelationship between airway mechanics, forced expiratory airflow, airway resistance and airway remodelling.

SUMMARY AND OUTLOOK

This thesis was concerned with the interaction between the mechanics of highly deformable human airways and the airflow through them with the ultimate objective of providing a better understanding of some respiratory disorders.

Part one provided a theoretical analysis of the mechanics of some specific components of the tracheobronchial tree. In chapter two the influence of a non-homogeneous stiffness of the epithelial basement membrane on airway collapse of membranous bronchioles was investigated. Results showed that a non-homogeneous stiffness of the basement membrane affects airway collapse. Results could only be obtained for the fundamental, "two-lobe" collapse. The numerical techniques chosen to solve the ordinary differential equation proved not to be sensitive enough for higher orders of folding. A different, more powerful method would be necessary to provide solutions with a higher accuracy and for a higher number of folds. Computations were stopped when the walls of the collapsed structure touched. Solutions have still to be found for a collapsed structure with opposite walls touching. This is not of particular concern for airway mechanics, but could be of interest for other biological systems such as veins. Additionally, no attempt has been made to analyse the possibility of the epithelial membrane being tethered in some way and the implications of this on airway collapse. No provision was made for the epithelial thickness. This is a simple geometric effect and should be fairly straightforward to incorporate.

A theoretical analysis of tracheal mechanics was presented in chapter three. Results of the computations are in good agreement with experimental evidence. Computations were stopped at the pressure at which the posterior membrane started touching the inner wall of the cartilage ring. No attempt was made to provide solutions for pressures exceeding the "wall-touching pressure." This is worth pursuing to better understand diseased states observed in tracheomalacia.

Part two of this thesis dealt with effects of airway remodelling and the effect on forced expiratory airflow and airway resistance. The major progress made with this new model is the more realistic approach used to represent airway mechanics. Computed results are all within a physiologically feasible range. One weakness, as already pointed out, is how a thickened submucosal wall area was incorporated. The resulting baseline value should be slightly higher than the normal (control) baseline value. A major problem is the reliability of data for the wall compartments of the central airways. Data used are based on small airways, the quality of extrapolation to centrally located airways is unknown but appears to give values for smooth muscle area greatly in excess of those measured by Tiddens et al [97]. The assumption of constricted airways having the same specific compliance as "relaxed" airways is also only based on an *in vitro* study on mid-sized cartilaginous airways. More experimental studies are needed to provide guidance as to the appropriate modelling approach to be used.

The results shown represent only some few areas of interest. No attempts so far have been made to investigate how changes in density, viscosity, or parenchymal shear modulus affect expiratory airflow or airway resistance in the new model although they have been done for the old models. So far only changes affecting all airways have been investigated. Regional variations in airway properties revealed interesting flow-volume and dose-response behaviour in the earlier models. It remains to be seen how these are changed in the new model.

REFERENCES

1. **Agostoni, E., and W. O. Fenn**. Velocity of muscle shortening as a limiting factor in respiratory air flow. *J. Appl. Physiol.* 15: 349-353, 1960.

2. **American Thoracic Society** Standards for the diagnosis and care of patients with chronic obstructive pulmonary disease (COPD) and asthma. *Am. Rev. Respir. Dis.* 136: 225-244, 1986.

3. **Asthma Research Foundation of New Zealand.** Asthma in New Zealand. Latest facts and statistics, March 1999. 1999.

4. **Asthma Research Foundation of New Zealand**. *CORD In New Zealand - Facts and Statistics.* 1996, Asthma and respiratory foundation of New Zealand: Wellington.

5. **Bai, A., D. H. Eidelman, J. C. Hogg, A. L. James, R. K. Lambert, M. S. Ludwig, J. Martin, D. McDonald, W. A. Mitzner, M. Okazawa, R. J. Pack, P. D. Paré, R. R. Schellenberg, H. A. W. M. Tiddens, E. M. Wagner, and D. Yager**. Proposed nomenclature for quantifying subdivisions of the bronchial wall. *J. Appl. Physiol.* 77: 1011-1014, 1994.

6. **Bates, D. V., P. T. Macklem, and R. V. Christie**. *Respiratory function in disease*. Philadelphia, London, Toronto: W. B. Saunders Company, 1971.

7. **Beer, F. P., and E. R. Johnston Jr.** *Mechanics of materials.* 3rd ed. New York: McGraw-Hill Book Company, 1981.

8. **Begis, D., C. Delpuech, P. Le Tallec, L. Loth, M. Thiriet, and M. Vidrascu**. A finite element model of tracheal collapse. *J. Appl. Physiol.* 64: 1359-1368, 1988.

9. **Blanc, F., S. Salmeron, C. Coirault, M. Bard, E. Fadel, E. Dulmet, P. Darteville, and P. Lecarpentier**. Effects of load and tone on the mechanics of isolated human bronchial smooth muscle. *J. Appl. Physiol.* 86: 488-495, 1999.

10. **Bosken, C. H., B. R. Wiggs, J. C. Hogg, and P. D. Paré**. Small airway dimensions in smokers with obstruction to airflow. *Am. Rev. Respir. Dis.* 142: 563-570, 1990.

11. **Chalmers, W. G., A. Little, K. R. Patel, and N. C. Thomson**. Endothelin -1-induced bronchoconstriction in asthma. *Am. J. Respir. Crit. Care Med.* 156: 382-388, 1997.

12. **Codd, S. L., R. K. Lambert, M. R. Alley, and R. J. Pack**. Tensile stiffness of ovine tracheal wall. *J. Appl. Physiol.* 76: 2627-2635, 1994.

13. **Comroe, J. H.** *Physiology of respiration.* Chicago: Year Book Medical Publishers, Inc., 1971.

14. **Correy, E. M., and D. A. Young**. Optimization of physical data tables by using simulated annealing. *Computers in Physics* 33-37, 1989.

15. **Corrin, B. E.** *Systematic Pathology. Third Edition Vol. 5. The Lungs.* Churchill Livingstone, 1990.

16. **Dallmann, M. J., R. C. McClure, and E. M. Brown**. Normal and collapsed trachea in the dog: Scanning electron microscopy study. *Am J Vet Res* 46: 2110 - 2115, 1985.

17. **Dawson, S. V., and E. A. Elliott**. Wave speed limitation on expiratory flow - a unifying concept. *J. Appl. Physiol.: Respirat. Environ. Excercise Physiol.* 43: 498-515, 1977.

18. **De Kock, M. A., J. A. Nadel, and C. M. Lewis**, ed. *Mechanisms of Airway Obstruction in human respiratoy disease (Proceedings of the International Symposium*

Tygerberg, South Africa, 1978). Functional anatomy of the trachea and main bronchi, ed. M. A. De Kock. 1978, South African Medical Research Council, Cape Town: Tygerberg, South Africa.

19. **Ding, D. J., J. G. Martin, and P. T. Macklem**. Effects of lung volume on maxdimal methacholine induced bronchoconstriction in normal humans. *J. Appl. Physiol.* 62: 1324-1330, 1987.

20. **Dunnill, M. S., G. R. Massarella, and J. A. Anderson**. A comparison of the quantitative anatomy of the bronchi in normal subjects, in status asthmaticus, in chronic bronchitis, and in emphysema. *Thorax* 24: 176, 1969.

21. **Elad, D., R. D. Kamm, and A. H. Shapiro**. Mathematical simulation of forced expiration. *J. Appl. Physiol.* 65: 14-25, 1988.

22. **Flaherty, J. E., J. B. Keller, and S. I. Rubinow**. Post buckling behavior of elastic tubes and rings with opposite sides in contact. *SIAM J. Appl. Math.* 23: 446-455, 1972.

23. **Fredberg, J. J., D. Inouye, B. Miller, M. Nathan, S. Jafari, H. S. Raboudi, J. A. Butler, and S. A. Shore**. Airway smooth muscle, tidal stretches, and dynamically determined contractile states. *Am. J. Respir. Crit. Care Med.* 156: 1752-1759, 1997.

24. **Fry, D. L.** Theoretical considerations of the bronchial pressure-flow volume relationships with particular reference to the maximum expiratory flow volume curve. *Phys. Med. Biol.* 3: 174-194, 1958.

25. **Fry, D. L., and R. E. Hyatt**. Pulmonary mechanics: a unified analysis of the relationship between pressure, volume and gas flow in the lungs of normal and diseased subjects. *Am. J. Med* 29: 672-89, 1960.

26. **Gamsu, G., and W. R. Webb**. Computed tomography of the Trachea: Normal and Abnormal. *AJR* 139: 321-326, 1982.

27. **Gibbons, W. J., A. Sharma, L. D., and P. T. Macklem**. Detection of excessive bronchoconstriction in asthma. *Am. J. Respir. Care Med.* 153: 582-589, 1996.

28. **Gibson, G. J.** *Clinical tests of respiratory function.* Macmillian Press London, 1984.

29. **Greene, R., and G. L. Lechner**. "Saber-Sheath" Trachea: A clinical and functional Study of Marked Coronal Narrowing of the Intrathoracic Trachea. *Radiology* 115: 265-268, 1975.

30. **Gunst, S. J., and J. Q. Stropp**. Pressure-volume and length-stress relationships in canine bronchi in vitro. *J. Appl. Physiol.* 64: 2522-2531, 1988.

31. **Habib, M. P., P. D. Paré, and L. A. Engel**. Variability of airway responses to inhaled histamine in normal subjects. *J. Appl. Physiol.* 47: 51-58, 1979.

32. **Hill, M. J., T. A. Wilson, and R. K. Lambert**. Effects of surface tension and intraluminal fluid on mechanics of small airways. *J. Appl. Physiol.* 82: 666-673, 1997.

33. **Hyatt, R. E.** Expiratory flow limitation. *J. Appl. Physiol.: Respirat. Envirom. Excercise Physiol.* 55: 1-8, 1983.

34. **Hyatt, R. E., and R. E. Flath**. Influence of lung parenchyma on pressure diameter behavior of dog bronchi. *J. Appl. Physiol.* 21: 1448-1452, 1966.

35. **Hyatt, R. E., T. A. Wilson, and E. Bar-Yishay**. Prediction of maximal expiratory flow in excised human lungs. *J. Appl. Physiol.* 48: 991-998, 1980.

36. **Ingram, R. H., and D. P. Schilder**. Effect of gas compression on pulmonary pressure, flow and volume relationship. *J. Appl. Physiol.* 21: 1821-26, 1966.

37. **Ishida, K., P. D. Paré, T. Blogg, and R. R. Schellenberg**. Effects of elastic loading on porcine trachealis muscle mechanics. *J. Appl. Physiol.* 93: 1033-1039, 1990.

38. **Ishida, K., P. D. Paré, J. Hards, and R. R. Schellenberg**. Mechanical properties of human bronchial smooth muscle in vitro. *J. Appl. Physiol.* 73: 1481-1485, 1992.

39. **James, A. L., J. C. Hogg, L. A. Dunn, and P. D. Paré**. The use of internal perimeter to compare airway size and to caculate smooth muscle shortening. *Am. Rev. Respir. Dis.* 138: 136-139, 1988.

40. **James, A. L., P. D. Pare, and J. C. Hogg**. The mechanics of airway narrowing in asthma. *Am. Rev. Respir. Dis.* 139: 242-246, 1989.

41. **James, A. L., P. D. Paré, and J. C. Hogg**. Effects of lung volume, bronchoconstriction, and cigarette smoke on morphometric airways dimensions. *J. Appl. Physiol.* 64: 913-919, 1988.

42. **Jeffery, P. K.** Morphometry of the airway wall in asthma and in chronic obstructive pulmonary disease. *Am. Rev. Respir. Dis.* 143: 1152-1158, 1991.

43. **Jeffery, P. K., R. W. Godfrey, E. Aedelroth, F. Nelson, A. Rogers, and S.-A. Johansson**. Effects of treatment on airway inflammation and thickening of basement membrane collagen in asthma. *Am. Rev. Respir. Dis.* 145: 890-899, 1992.

44. **Jones, J. G., R. B. Fraser, and A. J. Nadel**. Prediction of maximum expiratory flow rate from area transmural pressure curve of compressed airway. *J. Appl. Physiol.* 38: 1002-1011, 1975.

45. **Jones, J. G., R. B. Fraser, and J. A. Nadel**. Effect of changing airway mechanics on maximum expiratory flow. *J. Appl. Physiol.* 38: 1012-1021, 1975.

46. **Kresch, E., and A. Noordegraaf**. Cross-sectional shape of collapsible tubes. *Biophys. J.* 12: 274-294, 1972.

47. **Kuwano, K., C. H. Bosken, T. R. Bai, B. R. Wiggs, and J. C. Hogg**. Small airway dimensions in asthma and in chronic obstructive pulmonary disease. *Am. Rev. Respir. Dis.* 148: 1220-1225, 1993.

48. **Kuwano, K., C. H. Bosken, P. D. Pare, T. Bai, B. R. Wiggs, and J. C. Hogg**. Morphometric dimensions of small airways in asthma and chronic obstructive pulmonary disease (COPD) (Abstract). *Am. Rev. Respir. Dis.* 145: A386, 1992.

49. **Lai-Fook, S. J., R. E. Hyatt, and J. P. Rodarte**. Effect of parenchymal shear modulue and lung volume on bronchial pressure-diameter behavious. *J. Appl. Physiol.* 44: 859-868, 1978.

50. **Lai-Fook, S. J., T. A. Wilson, R. E. Hyatt, and J. R. Rodarte**. Elastic constants of inflated lobes of dog lungs. *J. Appl. Physiol.* 40: 508-513, 1976.

51. **Lambert, R. K.** A model for the elastic properties of the lung and their effect on expiratory flow. *J. Appl. Physiol.* 34: 34-48, 1973.

52. **Lambert, R. K.** A new computational model for expiratory flow from nonhomogeneous human lungs. *J. Biomech. Eng.* 111: 200-205, 1989.

53. **Lambert, R. K.** Role of basement membrane in airway collapse. *J. Appl. Physiol.* 71: 666-673, 1991.

54. **Lambert, R. K., E. M. Baile, R. Moreno, R. Bert, and P. D. Paré**. A method for estimating the Young's modulus of complete tracheal cartilage rings. *J. Appl. Physiol.* 70: 1152-1159, 1991.

55. **Lambert, R. K., E. H. D. Bel, and H. A. W. Tiddens**. Compliance of small cartilagenous human airways before and after bronchoconstriction and effect on resistance (Abstract). *Am. J. Respir. Crit. Care Med.* 159: A406, 1999.

56. **Lambert, R. K., S. L. Codd, M. R. Alley, and R. J. Pack**. Physical determinants of bronchiol mucosal folding. *J. Appl. Physiol.* 77: 1206-1216, 1994.

57. **Lambert, R. K., R. J. Pack, Y. Xia, C. D. Eccles, and P. T. Callaghan**. In vitro tracheal mechanics by nuclear magnetic resonance imaging. *J. Appl. Physiol.* 65: 1872-1879, 1988.

58. **Lambert, R. K., and P. D. Paré**. Lung parenchymal shear modulus, airway wall remodeling, and bronchial hyperresponiveness. *J. Appl. Physiol.* 83: 140-147, 1997.

59. **Lambert, R. K., B. R. Wiggs, K. Kuwano, J. C. Hogg, and P. D. Paré**. Functional significance of increased airway smooth muscle in asthma and COPD. *J. Appl. Physiol.* 74: 2771-2781, 1993.

60. **Lambert, R. K., and T. A. Wilson**. Flow limitation in a collapsible tube. *J. Appl. Physiol.* 33: 150-153, 1972.

61. **Lambert, R. K., T. A. Wilson, R. E. Hyatt, and J. R. Rodarte**. A computational model for expiratory flow. *J. Appl. Physiol.: Respirat. Environ. Excercise Physiol.* 52: 44-56, 1982.

62. **Lomasney, L., C. J. Bergin, J. Lomasney, V. Roggli, and F. W.** Case Report: CT Appearence of Lunate Trachea. *Journal of Computer Assisted Tomography* 13: 520-522, 1989.

63. **Ma, X., W. Li, and N. L. Stephens**. Detection of two clusters of mechanical properties of smooth muscle along the airway tree. *J. Appl. Physiol.* 80: 857-861, 1996.

64. **Martin, H. B., and D. Proctor**. Pressure-volume measurements on dog bronchi. *J. Appl. Physiol.* 13: 337-343, 1958.

65. **Mead, J., T. Takishima, and D. Leith**. Stress distribution in the lung: a model of pumonary elasticity. *J. Appl. Physiol.* 28: 596-608, 1970.

66. **Mead, J., J. M. Turner, P. T. Macklem, and J. B. Little**. Significance of the relationship between lung reciol and maximum expiratory flow. *J. Appl. Physiol.* 22: 95-108, 1967.

67. **Meiss, R. A.** Influence of intercellular tissue connections on airway muscle mechanics. *J. Appl. Physiol.* 86: 5-15, 1999.

68. **Metropolis, N., A. W. Rosenbluth, M. N. Rosenbluth, and A. H. Teller**. Equation of state calculations by fast computing machines. *J. Chem. Physics* 21: 1089-1092, 1953.

69. **Mitchell, H. W., R. Cvetkovski, M. P. Sparrow, P. R. Gray, and P. K. McFawn**. Concurrent measurement of smooth muscle shortening, lumen narrowing and flow to acetylchlorine in large and small porcine bronchi. *Eur. Respir. J.* 12: 1053-1061, 1998.

70. **Mitzner, W., and E. Wagner**. Bronchial vessels in the submucosa precipitate buckling of the airway epithelium (Abstract). *Am. Rev. Respir. Dis.* 147: A503, 1993.

71. **Moore, B. J., G. G. King, Y. D'Yachkova, H. R. Ahmand, and P. D. Paré**. Mechanism of methacholine dose-response plateaus in normal subjects. *Am. J. Respir. Crit. Med.* 158: 666-669, 1998.

72. **Moreno, R., R. Taylor, N. Mueller, J. Fleetham, D. Li, B. Wiggs, and P. D. Paré**. In vivo human tracheal pressure-area curves using computerized tomographic scans. *Am. Rev. Respir. Dis.* 134: 585-589, 1986.

73. **Moreno, R. H., J. C. Hogg, and P. D. Paré**. Mechanics of airway narrowing. *Am. Rev. Respir. Dis.* 133: 1171-1180, 1986.

74. **Moreno, R. H., G. S. McCormack, J. B. M. Mullen, J. C. Hogg, J. Bert, and P. D. Paré**. Effect of intravenous papain on tracheal pressure-volume curves in rabbits. *J. Appl. Physiol.* 60: 247-252, 1986.

75. **Mortola, J. P., and G. Sant'Ambrogio**. Mechanics of the trachea and behavior of its slowly adapting stretch receptors. *J. Physiol.* 286: 577-590, 1977.

76. **Newth, C. J. L., M. J. Lipton, R. G. Gould, and M. Stretton**. Varying tracheal cross-sectional area during respiration in infants and children with suspected upper airway obstruction by computed cinetomography scanning. *Pediatric Pulmonology* 9: 224-232, 1990.

77. **O'Byrne, P. M., and D. S. Postsma**. The many faces of airway inflammation. *Am. J. Respir. Crit. Care Med.* 159: S41-S66, 1999.

78. **Okazawa, M., K. Ishida, J. Road, R. R. Schellenberg, and P. D. Paré**. in vivo and in vitro correlation of trachealis muscle contraction in dogs. *J. Appl. Physiol.* 73: 1486-1493, 1992.

79. **Olsen, C. R., A. E. Stevens, and M. B. McIlroy**. Rigidity of tracheae and bronchi during muscular constriction. *J. Appl. Physiol.* 23: 27-34, 1967.

80. **Opazo-Saez, A., and P. D. Paré**. Stimulus-response relationships for isotonic shortening and isometric tension generation in rabbit trachealis. *J. Appl. Physiol.* 77: 1638-1643, 1994.

81. **Paradaens, J., K. P. van de Woestjijne, and J. Clement**. A physical model of expiration. *J. Appl. Physiol.* 33: 479-490, 1972.

82. **Press, W. H., B. P. Flannery, S. A. Teukolsky, and V. W. T.** *Numerical recipes in C*. Cambridge: Cambridge University Press, 1988.

83. **Rains, J. K., J. L. Bert, C. R. Roberts, and P. D. Paré**. Mechanical properties of human tracheal cartilage. *J. Appl. Physiol.* 72: 219-225, 1992.

84. **Reynolds, D. B.** Steady expiratory flow-pressure relationship in a model of the human bronchial tree. *J. Biomech. Eng.* 104: 153-158, 1982.

85. **Ribreau, C., S. Naili, M. Bonis, and A. Langlet.** Collapse of thin-walled elliptical tubes for high values of major-to-minor axis ratio. *J. Biomech. Eng.* 115: 432-440, 1993.

86. **Roberts, C. R., J. K. Rains, P. D. Paré, W. D. C., B. Wiggs, and J. L. Bert.** Ultrastructure and tensile properties of human tracheal cartilage. *J. of Biomech.* 31: 81-86, 1998.

87. **Robinson, P., M. Okazawa, T. Bai, and P. D. Paré.** In vivo loads on airway smooth muscle: the role of noncontractile airway structures. *Can. J. Physiol. Pharmacol.* 70: 602-606, 1991.

88. **Saunders, K. S.** *Clinical Physiology of the Lung.* Blackwell Scientific Publications, 1977.

89. **Scheel, W., H.-J. Strauss, and J. Weber.** Comparative Cinetracheobronchographic, Endoscopic and Functional Investigations with Regard to the Pre- and Postoperative Assesment of the Severity of Tracheobronchial Collapse (in German). *Z. Erkrank. Atm. org.* 172: 53-64, 1989.

90. **Seow, C. Y., R. R. Schellenberg, and P. D. Paré.** Structural and functional changes in the airway smooth muscle of asthmatic subjects. *Am. J. Respir. Crit. Care Med.* 158: 179-186, 1998.

91. **Shapiro, A. H.** Steady flow in collapsible tubes. *J. Biomech. Eng.* 99: 126-147, 1977.

92. **Shen, X., M. F. Wu, R. S. Tepper, and S. J. Gunst.** Mechanisms for the mechanical response of airway smooth muscle to length oscillation. *J. Appl. Physiol.* 83: 731-738, 1997.

93. **Shen, X., M. F. Wu, R. S. Tepper, and S. J. Gunst**. Pharmalogical modulation of the mechanical response of airway smooth muscle to length oscillation. *J. Appl. Physiol.* 83: 739-745, 1997.

94. **Stephens, N. L., W. Li, Y. Wang, and X. Ma**. The contractible apparatus of airway smooth muscle. *Am. J. Respir. Crit. Care Med.* 158: 80-94, 1998.

95. **Stern, E. J., C. M. Graham, R. W. Webb, and G. Gamsu**. Normal Trachea during Forced Expiration: Dynamic CT Measurements. *Radiology* 187: 27-31, 1993.

96. **Tepper, R.** Tracheomalacia (Personal Communication). 1999.

97. **Thurlbeck, W. M. E.** *The Lung, Structure, Function and Disease.* Wiliams & Willkins Company, 1978.

98. **Tiddens, H. A. W. M., P. D. Pare, J. C. Hogg, H. W. C. J., R. Lambert, and J. C. de Jongste**. Cartilagenous airway dimensions and airway obtruction in human lungs. *Am. J. Respir. Crit. Care Med.* 152: 260-266, 1995.

99. **Timoshenko, S.** *Strength of Materials.* 3rd. ed. New York: Nostrand Reinhold, 1958.

100. **Timpl, R.** Structure and biological activity of basement membrane proteins. *Eur. J. Biochem.* 180: 487-502, 1989.

101. **Tsao, T. C., and W. B. Shieh**. Intrathoracic tracheal dimensions and shape changes in chronic obstructive pulmonary disease. *J. Formosan Medical Association* 93: 30-34, 1994.

102. **Wagner, E. M., and W. Mitzner**. Effects of bronchial vascular engorgement on airway dimensions. *J. Appl. Physiol.* 81: 293-301, 1996.

103. **Weibel, E. R.** *Morphometry of the Human Lung.* New York: Academic Press Inc., 1963.

104. **Welling, L. W., and J. J. Grantham**. Physical properties of isolated perfused renal tubulus and tubular basement membranes. *J. Clin. Invest.* 51: 1063-1075, 1972.

105. **West, J. B.** *Respiratory Physiology.* Williams & Willkins Company, 1990.

106. **Wheatley, J. R., P. D. Paré, and L. A. Engel**. Reversibility of induced bronchoconstriction by deep inspiration in asthmatic and normal subjects. *Eur. Respir. J.* 2: 1989.

107. **Widdicombe, J., and A. Davis**. *Respiratory Physiology.* London: Edward Arnold Publishers Ltd., 1983.

108. **Wiggs, B. R., C. A. Hrousis, J. M. Drazen, and R. D. Kamm**. On the mechanism of mucosal folding in normal and asthmatic airways. *J. Appl. Physiol.* 83: 1814-1821, 1997.

109. **Wiggs, B. R., R. Moreno, C. Hilliam, and P. D. Paré**. A model of the mechanics of airway narrowing. *J. Appl. Physiol.* 69: 849-860, 1990.

110. **Winter, D. C.** Elastic properties of collapsing and expanding trachea. *J. Biomech. Eng.* 107: 300-303, 1985.

111. **Winter, D. C., R. L. Pimmel, and B. F. Lewis**. Direct in-vivo measurements of the elastic properties of canine trachea. *J. Biomech. Eng.* 104: 311-313, 1982.

112. **Woolcock, A. J., C. M. Salmone, and K. Yan**. The shape of the dose-respone curve to histamine in asthmatic and normal subjects. *Am. Rev. Respir. Dis.* 130: 71-75, 1984.

113. **Yamada, H.** *Strength of biological materials.* Baltimore, MD: Williams and Willkins, 1970.

APPENDICES

A. Derivation of differential equation describing elastic tube collapse for non-uniform stiffness

The basic equations as presented in part I, chapter 2.2.1 are:

$$\sum F_x = 0 \Rightarrow \frac{dT}{ds} + S\frac{d\theta}{ds} = 0 \qquad \text{(A1)}$$

$$\sum F_y = 0 \Rightarrow \frac{dS}{ds} - T\frac{d\theta}{ds} - P = 0 \qquad \text{(A2)}$$

$$\sum M = 0 \Rightarrow \frac{dM}{ds} - S = 0 \qquad \text{(A3)}$$

$$M = D(\kappa - \kappa_0) \qquad \text{(A4)}$$

where D, κ and κ_0 may be functions of arc length s.

Eliminating T, S and M results in:

$$\begin{aligned} &\left(D'''(s)\Delta + 3D''(s)\Delta' + 3D'(s)\Delta'' + D(s)\Delta'''\right)\kappa \\ &-\left(D''(s)\Delta + 2D'(s)\Delta' + D(s)\Delta''\right)\kappa' \\ &+\kappa' P + \kappa^3\left(D'(s)\Delta - D(s)\Delta'\right) = 0 \end{aligned} \qquad \text{(A5)}$$

where $\Delta \equiv \kappa - \kappa_0$ is the difference in curvature between the deformed ($\kappa = d\theta/ds$) and the undeformed ($\kappa_0 = d\theta_0/ds$) state.

The flexural rigidity can be written as:

$$D(s) = D_0 f(s) \qquad \text{(A6)}$$

where D_0 is the base flexural rigidity and $f(s)$ is the dimensionless function describing the variations in stiffness along the circumference of the tube as introduced in Part I, chapter 2.2.1.

The length scale in Eqns. (A1) to (A6) can be normalised by introducing the non-dimensional arc length, λ.

$$\lambda = \frac{s}{R_0} \tag{A7}$$

R_0 is the radius of the undeformed, circular cross-section tube.

This results in the following scales for the bending moments M, forces F and the pressure P.

$$\begin{aligned} M &= \frac{D_0}{R_0} M^* \\ F &= \frac{D_0}{R_0^2} F^* \\ P &= \frac{D_0}{R_0^3} P^* \end{aligned} \tag{A8}$$

An asterisk indicates a dimensionless quantity.

Eq. (A5) can thus be rewritten in non-dimensional form (Eq. (A9)).

$$\begin{aligned} &\theta'''' + \frac{f'''(\lambda)}{f(\lambda)}(\theta-\theta_0)' + 3\frac{f''(\lambda)}{f(\lambda)}(\theta-\theta_0)'' + 3\frac{f'(\lambda)}{f(\lambda)}(\theta-\theta_0)''' - \\ &\{f''(\lambda)(\theta-\theta_0)' + 2f'(\lambda)(\theta-\theta_0)'' + f(\lambda)(\theta-\theta_0)'''\}\frac{\theta''}{f(\lambda)\theta'} + \\ &\frac{P^*}{f(\lambda)}\frac{\theta''}{\theta'} + \{f'(\lambda)(\theta-\theta_0)' + f(\lambda)(\theta-\theta_0)''\}\frac{(\theta')^2}{f(\lambda)} = 0 \end{aligned} \tag{A9}$$

When θ'_0'is constant, Eq. (A9) reduces to Eq. (A10).

$$\begin{aligned}&\theta'''' + \frac{f'''(\lambda)}{f(\lambda)}(\theta' - 1) + 3\frac{f''(\lambda)}{f(\lambda)}\theta'' + 3\frac{f'(\lambda)}{f(\lambda)}\theta''' \\ &-\{f''(\lambda)(\theta' - 1) + 2f'(\lambda)\theta'' + f(\lambda)\theta'''\}\frac{\theta''}{f(\lambda)\theta'} \\ &+\frac{P^*}{f(\lambda)}\frac{\theta''}{\theta'} + \{f'(\lambda)(\theta' - 1) + f(\lambda)\theta''\}\frac{(\theta')^2}{f(\lambda)} = 0\end{aligned} \tag{A10}$$

The well-known, often solved equation for a uniform tube can be recovered by setting D constant (and thus $f(s) = 1$)

$$\theta''''\theta' - \theta'''\theta'' + \theta''(\theta')^3 + \theta''P^* = 0 \tag{A11}$$

B. Simulated annealing

Simulated annealing is an algorithm used for combinatorial minimisation [82]. The idea of simulated annealing is an analogy with thermodynamics, specifically with the way that liquids freeze and crystallise, or metals cool and anneal. At high temperatures, the molecules of a liquid move freely with respect to one another. When the liquid is cooled slowly, thermal mobility is lost and the atoms are often able to line themselves up and form a pure crystal that is completely ordered over a distance up to billions of times the size of an individual atom in all directions. This is the state of minimum energy for this system. If a liquid metal is cooled quickly ("quenched") it does not reach this state but rather ends up in a polycrystalline or amorphous state having somewhat higher energy. The essence of annealing is slow cooling, allowing sufficient time for redistribution of the atoms as they loose mobility.

The analogous quantity in computational simulated annealing to the energy of a liquid being cooled down is the cost function (*CF*) or objective function to be optimised. The idea is to go from a starting point of the function (the initial guess) as far as one can go towards the minimised state. This often leads to a local, but not necessarily a global minimum, thus there is always a certain probability p that the found minimum is not the global one. This probability p is derived from a Boltzmann distribution

$$p(E) = \exp\left(-\frac{E}{kT}\right) \tag{B1}$$

The implementation of these thermodynamical concepts into numerical calculations was first proposed by Metropolis and co-workers in 1953 [68]. Offered a succession of options, the system was assumed to change its configuration from a state CF_1 to CF_2 with the probability

$$p = exp(-\Delta CF \cdot \tau) \tag{B2}$$

The control parameter τ (analogue of temperature) changes according to a so-called annealing schedule which defines how τ has to be raised from a low value to a high value. That is the schedule specifies how many random changes in configuration must be made before each upward step in τ is taken and how large is that step. The assignment of this schedule as well as the meaning of “low” and high” in this context, requires some trial end error testing and some physical insight. Generally, a simulation is started with a low value of τ, which means that virtually any configuration will be accepted. With progressing simulation, τ is gradually raised thus reducing the acceptable probabilities according to Eq. (B2). Computations are terminated when CF of the actual generated configuration is within an acceptable tolerance of the targeted CF_{Min}.

Fig. B.1 depicts the algorithm of simulated annealing implemented into the programs BRONCHI and TRACHEA.

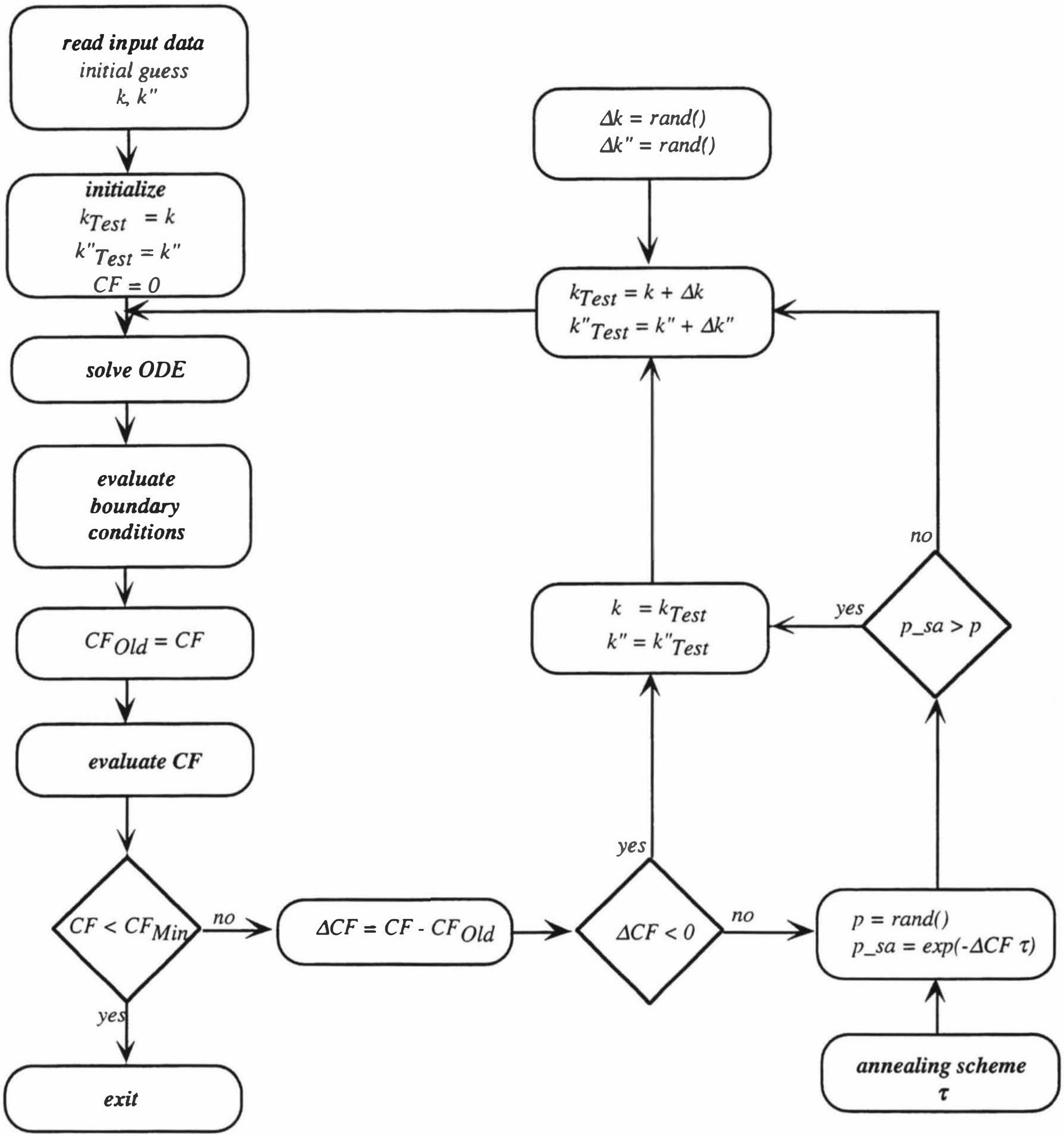

Fig. B.1. Flow chart outlining simulated annealing algorithm used in the programs BRONCHI and TRACHEA.

C. Software documentation

All software was developed using C compiled on a Macintosh Power PC platform using Metroworks Codewarrior compiler v. 4. Numerical procedures were adopted from the Numerical Recipes in C toolbox [82]. All source code as well as result files of simulations were archived on CD (inside rear cover).

C.1 The application BRONCHI

BRONCHI was designed to numerically compute the mucosal folding which was extensively discussed in part I. 2. It is based on the FORTRAN program BRONK (developed by R. Lambert). BRONCHI was specifically designed to investigate effects of a non-homogeneous stiffness of epithelial basement membrane on airway collapse. It is, in principle, an extension of BRONK. BRONCHI uses the concept of simulated annealing as well as a simple "scan algorithm" which simply numerically integrates the ordinary differential equation within a certain given interval of the initial values ("mapping"). The main menu is shown below. The required input parameters are self-explanatory. The file formats are given below.

- Main menu

```
###########   A I R W A Y S   ###########
      Simulating the collapsing of the airways
      including a non-uniform stiffness

-----------------------------------------------------------

 / (0) : Annealing        /  (1) : Mapping       /      ⇐ manual annealing/mapping
 / (2) : File Annealing   /  (3) : File Mapping  /      ⇐file annealing/mapping
 / (4) : Reload           /  (5) : Exit          /      ⇐ reload setup file / quit prog.

Your choice : ==>
```

- Setup File

File Name: BRONCHI.SETUP

```
2           // Method of Integration 1: Runge-Kutta  2: Bulirsch-Stoer
6           // stiffness function  fmax @ 0 &pi/n
1.0e-3      // max. tolerance in final angle theta
0.01        // max. tolerance int theta" (shear)
0.1         // stepsize k for mapping
0.1         // stepsize k" for mapping
2500.0      // adjusting parameter for costfunction (theta)
1.0         // adjusting parameter for costfunction (shear)
```

Key for stiffness distributions:

1: 3rd order polynomial, f_{max} @ π/n (approximation)

2: 4th order polynomial, f_{max} @ π/n (approximation)

3: Sinusoidal, f_{max} @ π/n

4: Sinusoidal, f_{max} @ $1/2\ \pi/n$

5: Linear approximation: $f(x) = 1 + \alpha\,(n/\pi)s$

6: Sinusoidal, f_{max} @ 0

7: Sinusoidal, f_{max} @ 0 and π/n

- Input file formats

- *Simulated annealing batch file:*

no. of folds / pressure / initial guess: curvature / initial guess: 2nd derivative of curvature / stiffness coefficient / output file name

Example:

```
2    6.2    3.34     -12.966   0.5   n2_p62_a05_f@0/2
2    6.3    3.388    -13.41    0.5   n2_p63_a05_f@0/2
2    6.4    3.45     -14.07    0.5   n2_p64_a05_f@0/2
2    6.5    3.4966   -14.513   0.5   n2_p65_a05_f@0/2
2    6.6    3.512    -14.7     0.5   n2_p66_a05_f@0/2
```

(Maximal number of data sets: 50)

- *Mapping batch file*

no. of folds / pressure / min. curvature / max. curvature / min. 2nd derivative of curvature / max. 2nd derivative of curvature / stiffness coefficient / output file name

(step sizes are given in setup file BRONCHI.SETUP)

Example:

```
2   5.1   2.475   2.477   -3.77   -3.76   0.5   p51/2
2   5.2   2.524   2.526   -4.01   -4.00   0.5   p52/2
2   5.3   2.565   2.575   -4.255  -4.2    0.5   p53/2
2   5.4   2.68    2.68    -4.795  -4.785  0.5   p54/2
2   5.5   2.802   2.809   -5.45   -5.4    0.5   p55/2
```

(Maximal number of data sets: 50)

- Output files

Three different output files distinguished by different extensions can be generated.

- *.map ⇐ *summary of results of file mapping [3]*

- *.cg ⇐ *Computed coordinates (*X / Y / θ/ θ' / θ'' / θ'''/ *arc length/ shear force / tensile force) in Cricket Graph Format*

- *.Res ⇐ *results file (based on simulated annealing)*

Example of results file:

```
-----------------------------------------------------
* Thu Dec 18 10:42:03 1997
----------- Simulated annealing --------------------
* Number of folds          :           2
* Normalized pressure      :  4.300000000
* Curvature                :  1.010000000
* d2kdx2                   : -0.020000000
* Stiffness factor         :  1.000000000
* Stiffness type           :           6
* -------- results of calculations ------------------
* Initial Curvature        :  1.010000000
* Initial k"               : -0.020000000
* Angle at far end         :  1.570895324
* rel. Error (Angle)       :  0.000063020
* Shear at far end         : -0.000443653
* Area (semi loop)         :  0.785372479
* Area (complete)          :  3.141489917
* Outer circle             :  1.005909007
* Inner circle             :  0.995691341
* Fraction of lumem area   :  0.008566332
* Number of coordinates    :         365
* ---------------------------------------------------
```

C.2 The application TRACHEA

TRACHEA was developed to investigate various aspects of tracheal collapse as extensively discussed in section I.3. The underlying numerical concept of TRACHEA is identical with the concept used in BRONCHI. The required input parameters are self-explanatory. The file formats are given below.

- Main menu

```
 #### Numerical calculation of a collapse ####
 ####    of an entire trachea             ####

-----------------------------------------------------
 [1] : Start Simulated Annealing           ⇐ start annealing computation
 [2] : Batch mode Simulated Annealing      ⇐ load data file name for batch mode
 [3] : Mapping                             ⇐ "scanning" of solution space
 [4] : Batch mode Mapping                  ⇐ load data file name for batch mode
 [5] : Compute shapes                      ⇐ compute undeformed cartilage shapes
 [0] : Exit                                ⇐ terminate application
-----------------------------------------------------
 ==>
```

- Setup file TRACHEA.SETUP

```
6               // Stiffness Function         ⇐ key is identical with BRONCHI
1.0e-3          // allowed tolerance in Costfunction
1.0             // C  k = C + As^2
0.0             // A
0.0             // normalised stretch factor of smooth muscle
0.01            // step size curvature (mapping)
0.01            // step size k" (mapping)
2.356           // far end of integration
1  TestCircShapeLc20.Cdata                    ⇐ generates log file during batch computation
```

(1: generate log file / 0: do not generate log file)

- Input file formats

- *simulated annealing batch file*:

pressure / posterior membrane length / initial guess: curvature / initial guess: 2^{nd} derivative of curvature / stiffness coefficient / output file name

Example:

```
0.0    2.0    0.5     1.0    0.0     Circ_Lmax_f1_a05_p00
0.1    2.0    0.5     1.5   -0.5     Circ_Lmax_f1_a05_p01
0.2    2.0    0.5     1.5   -0.5     Circ_Lmax_f1_a05_p02
```

(Maximal number of data sets: 200)

- *mapping batch file*

pressure / posterior membrane length / min. curvature / max. curvature / min. 2nd derivative curvature / max. 2nd derivative curvature / stiffness coefficient / output file
(step size is given in setup file TRACHEA.SETUP)

Example:

```
0.1    2.0    0.1    1.0    -1.5  1.5   -0.5      Circ_Map_p01
0.2    2.0    0.1    1.0    -1.5  1.5   -0.5      Circ_Map_p02
0.3    2.0    0.1    1.0    -1.5  1.5   -0.5      Circ_Map_p03
0.4    2.0    0.1    1.0    -1.5  1.5   -0.5      Circ_Map_p04
```

(Maximal number of data sets: 200)

- Output files

Five different output files can be generated.

- *.map ⇐ *summary of results of file mapping (3)*
- *.cg ⇐ *Computed coordinates* (X_c / Y_c / θ / θ' / θ'' / θ''' / *arc length/ shear force / tensile force/*X_m /Y_m) *in Cricket Graph Format* (X_c, Y_c, X_m, Y_m *are the coordinates of the cartilage ring and posterior membrane, respectively)*
- *.* ⇐ *log file name as specified in TRACHEA.SETUP. Summarises the major results obtained by simulated annealing batch mode computations. (pressure / length of posterior membrane / stiffness coefficient / indentation depth / distance between cartilage ring tips / tension in posterior membrane / x-component of tension / y-component of tension)*
- *.Shape ⇐ *computes initial shape of undeformed* ($p = 0$) *cartilage ring based on empirical formula* $k = C + A\lambda^2$.
- *.Res ⇐ *results file (based on simulated annealing)*

Example of results file:

```
* Results of Trachea calculations *
* Calculations started    : Thu Nov 27 10:01:03 1997
* Time required     [sec] : 29
* -----------------------------------------------
* ## circular calculation ##
* ------------ Input parameter ------------------
* Normalized pressure    : -0.100000000
* Curvature              :  1.200000000
* d2kdx2                 : -0.200000000
* Stiffness coefficient  :  0.000000000
* Stiffness type         :            6
* Length of muscle       :  2.000000000
* Curv. coefficient A    :  0.000000000
* Curv. coefficient C    :  1.000000000
* Max. tolerance in CF   :  0.001000000
* --------- Results of computations -------------
* Initial curvature      :  1.101238685
* Initial k"             : -0.104063570
* Calc. Length of muscle :  1.999115967
* Calc. Tension in muscle:  0.142121604
* X - component Fx       :  0.108396785
* Y - component Fy       :  0.091916741
* Initial tension To     : -0.003689999
* F(P) x                 : -0.104706786
* F(P) y                 : -0.091916741
* Resulting angle beta   :  0.703311780    ⇐ angle between Fx and T (in posterior  Membrane)
* Radius of circular area:  1.421216041
* Subtending angle delta :  1.406623560
* Area covered by muscle :  0.424239916
* Area (semi loop)       :  0.780517979
* Area (complete lumen)  :  1.561035958
* Resulting Area         :  1.985275874
* Final x - coordinate   :  1.047067861
* Final y - coordinate   :  0.919167408
* Gap width              :  1.838334817    ⇐ distance between cartilage ring tips
* Expanding width        :  0.337248186    ⇐ height/depth of posterior membrane deformation
* Final angle            :  1.670202025
* Costfunction           :  0.000984901
* Net bending moments    :  0.000100868
* Number of coordinates  :          379
* -----------------------------------------------
```

C.3 The application AIRFLOW

AIRFLOW was developed to investigate effects of airway remodelling on forced expiratory flow and airway resistance. All results presented in part II were obtained by using AIRFLOW.

- Main menu

```
**** Airflow Computation ****

 [1] : Run MEFV simulation            ⇐ forced expiratory flow model
 [2] : Generate IVPF curve            ⇐ generate one single IVPF curve
 [3] : Run Resistance Model           ⇐ "static", published RM
 [4] : Run FEV1 simulation            ⇐ compute FEV1 based on MEFV simulation
 [5] : Run Dosed FEV1 simulation      ⇐ merged RM and expiratory flow model
 [6] : Run batch mode dosed FEV1      ⇐ batch mode for [5]
 [0] : Exit
 -------------------------------------------------------
 ==>
```

The files required for the different computations are summarised in the following table.

	airway mechanics file	**airflow file**	**Resistance file**	**Regression data file**	**MEFV file**	**Batch file**
1	√	√	-	-	-	-
2	√	√	-	-	-	-
3	√	-	√	√	-	-
4	-	√	-	-	√	-
5	√	√	√	√	-	-
6	(√)	(√)	(√)	-	-	√

- file formats

- Airway mechanics (AwMech.dat)

```
* data for trachea (z = 0) and bronchi
z       Ao[m^2]       L[m]        alpha_0    slope[1/Pa]      n1          n2
0      0.000237      0.120000     0.882000     0.000110     1.000000     10.000000
1       0.000118      0.047600     0.882000     0.000300     1.000000     10.000000
2       0.000150      0.019000     0.686000     0.000510     1.000000     10.000000
3       0.000175      0.007600     0.546000     0.000800     1.000000     10.000000
4       0.000210      0.012700     0.428000     0.001000     1.000000     10.000000
5       0.000255      0.010700     0.337000     0.001250     1.000000     10.000000
6       0.000310      0.009000     0.265000     0.001420     1.000000     10.000000
7       0.000385      0.007600     0.208000     0.001590     1.000000     10.000000
8       0.000470      0.006400     0.164000     0.001740     1.000000     10.000000
9       0.000585      0.005400     0.129000     0.001840     1.000000     10.000000
10      0.000750      0.004700     0.102000     0.001940     1.000000     10.000000
11      0.000980      0.003900     0.080000     0.002060     1.000000     9.000000
12      0.001440      0.003300     0.063000     0.002180     1.000000     8.000000
13      0.002225      0.002700     0.049000     0.002260     1.000000     8.000000
14      0.003470      0.002300     0.039000     0.002330     1.000000     8.000000
15      0.005650      0.002000     0.031000     0.002390     1.000000     7.000000
16      0.009000      0.001700     0.024000     0.002430     1.000000     7.000000
1       0.000118      0.047600     0.882000     0.000300     1.000000     10.000000
2       0.000150      0.019000     0.686000     0.000510     1.000000     10.000000
3       0.000175      0.007600     0.546000     0.000800     1.000000     10.000000
4       0.000210      0.012700     0.428000     0.001000     1.000000     10.000000
5       0.000255      0.010700     0.337000     0.001250     1.000000     10.000000
6       0.000310      0.009000     0.265000     0.001420     1.000000     10.000000
7       0.000385      0.007600     0.208000     0.001590     1.000000     10.000000
8       0.000470      0.006400     0.164000     0.001740     1.000000     10.000000
9       0.000585      0.005400     0.129000     0.001840     1.000000     10.000000
10      0.000750      0.004700     0.102000     0.001940     1.000000     10.000000
11      0.000980      0.003900     0.080000     0.002060     1.000000     9.000000
12      0.001440      0.003300     0.063000     0.002180     1.000000     8.000000
13      0.002225      0.002700     0.049000     0.002260     1.000000     8.000000
14      0.003470      0.002300     0.039000     0.002330     1.000000     8.000000
15      0.005650      0.002000     0.031000     0.002390     1.000000     7.000000
16      0.009000      0.001700     0.024000     0.002430     1.000000     7.000000
```

Although not applied in this thesis, AIRFLOW allows the computation of parallel non-homogeneous human lungs as published in [52]. Therefore the input file above, shows different sets of lung mechanics parameter for each lobe. Results were obtained by using data sets for the first lobe only.

- Resistance file (Resistance.dat)

```
* Tue Aug 25 16:50:05 1998
air
1.13   1.87e-5
1   // no of lobes
* data for P-V curve
z        TLCr[m^3]   VCr[m^3]   ref Pr[Pa]  slope[1/Pa]     n1      n2
1      0.002425    0.002090    0.000000    0.001408    1.000000    20.000000
2      0.002425    0.002090    0.000000    0.001408    1.000000    20.000000
* Initial, final values and deflation stepsize [%]
          VCi(1)     VCi(2)      VCf(1)      VCf(2)
       80.000000   80.000000   00.000000    00.000000
```

- Airflow file (Airflow.dat)

```
1.13  1.87E-05                              // density and viscosity
490    0.7                                    // P of interest / ShearMod/PL
3     3     10                                    // Type of WA central/peri/ cutover / 3: norm / 2: COPD / 1: asthma
0.5                                           // airflow l/s
1 50 1   -1.9    1.2                          // dose  / max. Dose / dose mode / alpha / beta
0    16                                       // First & Last dosed Airway Generation
0.54                                          // Minimum Airway muscle length Lc/Lm
4.9e4                                         // maximum stress in Pa
-2.85  9.812 -10.931   4.905                  // fit parameter for active isometric curve, a0, a1, a2, a3
1   50   1                                    // switch for Tnorm Result file / VC / switch for AirwayClosure.log
* z       PMC     WAadv     WAsm    WAsub     alpha0  // % cartilage & WA multiplier
  0    0.33     1         1       1         1
  1    0.33     1         1       1         1
  2   0.67      1         1       1         1
  3    1        1         1       1         1
  4    1        1         1       1         1
  5    1        1         1       1         1
  6    1        1         1       1         1
  7    1        1         1       1         1
  8    1        1         1       1         1
  9    1        1         1       1         1
 10    1        1         1       1         1
 11    1        1         1       1         1
 12    1        1         1       1         1
 13    1        1         1       1         1
 14    1        1         1       1         1
 15    1        1         1       1         1
 16    1        1         1       1         1
```

- Regression data file (*Regression.data*)

The regression data file contains the parameters required to compute airway wall areas, as outlined in part II. *Regression.data* is a fixed file name and will automatically be loaded when simulation is started.

```
* Intercept & Slope
0.085    0.137         // WAadv Asthma
0.084    0.086         // WAadv BosCOPD
0.116    0.079         // WAadv Control
0.16     0.24          // WAadv TidCOPD
0.16     0.24          // WAadv CF
0.001    0.063         // WAsm Asthma
0.016    0.035         // WAsm BosCOPD
0.056    0.02          // WAsm Control
0.23     0.022         // WAsm TidCOPD
0.62     0.017         // WAsm CF
0.009    0.099         // WAsub Asthma
0.054    0.056         // WAsub BosCOPD
0.067    0.052         // WAsub Control
0.08665  0.0693  0     // WAsub TidCOPD + Hogg Score
0.778    0.058         // WAsub CF
0.77  0.0395   0.0118  // FepiCF   / HarmWAepiCF
0.91  0.02132  0.0149  // FepiCOPD / HramWAepiCOPD
```

- Batch file

This option allows a batch processing of dosed FEV1 computations (5). One input set consists of four file names:

1st line : airway mechanics file name
2nd line : airflow file name
3rd line : resistance data file name
4th line : output file name

Example:

```
AwMech.dat                ⇐ 1st line: airway mechanics file
Airflow.dat               ⇐ 2nd line: airflow file
Resistance.dat            ⇐ 3rd line: resistance data file
Norm                      ⇐ 4th line: output file name
AwMech.dat                ⇐ next set of file names
Airflow.dat
ResNormWAadv15.dat
 NormWAadv15
```

(Maximal number of file name sets: 70)

- MEFV file

Result file generated when simulating forced expiratory airflow.

- Output files

The application AIRFLOW can generate up to seven different output files, distinguished by different file extensions.

*.log	⇐ *generated by MEFV computation [1]. Log file of intermediate computational results.*
*.MEFVdata	⇐ *generated by MEFV computation [1]. Summary of data required to generate MEFV curve*
*.IVPFData	⇐ *generated by IVPF computation [2]. Summary of results required to generate IVPF curve.*
*.ResData	⇐ *generated by (static) resistance computation [3]. Summary of results required to generate Raw vs. log(dose) curve.*
*.FEV1Res	⇐ *generated by dosed FEV1 computations [5,6]. Summary of results required to generate FEV1 vs. log(dose) curve.*
*.RawRes	⇐ *generated by dosed FEV1 computations [5,6]. Summary of results required to generate Raw vs. log(dose) curve based on dynamically compliant airways.*
*.TnormRes	⇐ *generated by dosed FEV1 computations [5,6]. Summary of results required to generate (normalised) tension vs. (normalised) muscle length.*